Design and Optimization of Broadband Silicon Photonic Devices

by

Kazim Görgülü

A Dissertation Submitted to the
Graduate School of Sciences and Engineering
in Partial Fulfillment of the Requirements for
the Degree of

Doctor of Philosophy

in

Electrical and Electronics Engineering

KOÇ ÜNİVERSİTESİ

July 26, 2023

Design and Optimization of Broadband Silicon Photonic Devices

Koç University

Graduate School of Sciences and Engineering

This is to certify that I have examined this copy of a doctoral dissertation by

Kazim Görgülü

and have found that it is complete and satisfactory in all respects,

and that any and all revisions required by the final

examining committee have been made.

Committee Members:

Assist. Prof. Emir Salih Mağden (Advisor)

Prof. Alper Kiraz

Assoc. Prof. Sedat Nizamoğlu

Assoc. Prof. Onur Ferhanoğlu

Assist. Prof. Berna Morova

Date:

Dedicated to my wife Saliha, for all of her love and support.

ABSTRACT

Design and Optimization of Broadband Silicon Photonic Devices
Kazim Görgülü
Doctor of Philosophy in Electrical and Electronics Engineering
July 26, 2023

The integration of photonic systems on a chip offers enhanced performance, functionality, and reliability. While there are various material platforms available for constructing photonic integrated circuits, silicon stands out due to its compatibility with existing fabrication technologies and its high refractive index contrast. These features enable sub-micrometer waveguide scaling and dense packing of optical functions, combined with cost-effective and reliable manufacturing processes. Silicon photonics has already demonstrated its effectiveness in high-speed communication applications, but its potential reaches far beyond that. It shows promise for diverse applications like LIDAR, photonic switching, computing, and sensing, making it a versatile technology with a wide range of possibilities. Consequently, there is a growing demand for efficient and innovative photonic building blocks on the silicon platform to meet the specific requirements of these applications. This thesis focuses on the development of advanced photonic devices tailored for photonic integrated circuits. The first part presents the design and experimental demonstration of compact silicon photonic filters using optimized fast adiabatic waveguides, enabling arbitrarily wide bandwidths. These devices, with the widest bandwidths reported to date, find applications in high-throughput communications and ultra-broadband sensing. Subsequently, a novel deep photonics network architecture is introduced, enabling the rapid design of high-performance, multi-functional photonic devices. A proof-of-concept device with an arbitrary dispersion profile over a wide bandwidth is demonstrated. Lastly, a fabrication variation-aware device design concept is presented, utilizing the deep photonic network architecture to account for the effects of the actual fabrication process. Overall, this work contributes to the development of high-performance and versatile silicon photonic systems for a range of applications.

ÖZETÇE

Geniş Bantlı Silisyum Fotonik Aygıtların Tasarımı ve Optimizasyonu
Kazim Görgülü
Elektrik ve Elektronik Mühendisliği, Doktora
26 Temmuz 2023

Fotonik sistemlerin bir çip üzerinde entegrasyonu, performansı, işlevselliği ve güvenilirliği artırmaktadır. Fotonik entegre devrelerin oluşturulması için çeşitli malzeme platformları mevcuttur, ancak silisyum mevcut üretim teknolojileriyle uyumlu olması ve yüksek kırılma indisi farkı nedeniyle öne çıkar. Bu özellikler mikrometre-altı dalga kılavuzlarının elde edilmesini ve optik fonksiyonların yoğun bir şekilde entegrasyonunu düşük maliyet ve güvenilir üretimle birleştirir. Silisyum fotonik teknolojisi, yüksek hızlı iletişim uygulamalarında etkinliğini zaten kanıtlamış olsa da potansiyeli bunun ötesine uzanır. LIDAR, fotonik anahtarlama, hesaplama ve algılama gibi çeşitli uygulamalar için umut vaat etmektedir, bu da geniş bir uygulama yelpazesi sunan çok yönlü bir teknoloji olduğunu gösterir. Sonuç olarak, bu uygulamaların spesifik gereksinimlerini karşılamak için silisyum platformunda verimli ve yenilikçi fotonik yapı taşlarına olan talep artmaktadır. Bu tez, fotonik entegre devreler için özel olarak tasarlanmış ileri düzey fotonik aygıtların geliştirilmesine odaklanmaktadır. İlk bölümde, optimize edilmiş hızlı adiabatik dalga kılavuzları kullanarak istenilen bant genişliklerinde tasarlanabilen kompakt silisyum fotonik filtrelerin tasarımı ve deneysel gösterimi sunulmaktadır. Bugüne kadar rapor edilen en geniş bant genişliklerine sahip olan bu aygıtlar, yüksek verimli iletişim ve ultra geniş bant algılama uygulamalarında kullanılabilir. Ardından, yüksek performanslı, çok fonksiyonlu fotonik aygıtların hızlı tasarımını sağlayan yeni bir derin fotonik ağ mimarisi tanıtılmaktadır. Geniş bir bant üzerinde keyfi bir dağılım profiline sahip bir kavram kanıtlama aygıtı gösterilir. Son olarak, gerçek üretim sürecinin etkilerini hesaba katmak için derin fotonik ağ mimarisinden faydalanan ve üretim varyasyonlarından etkilenmeyen bir aygıt tasarımı konsepti sunulmaktadır. Genel olarak, bu çalışma, çeşitli uygulamalar için yüksek performanslı ve çok yönlü silisyum fotonik sistemlerinin geliştirilmesine katkıda bulunmaktadır.

ACKNOWLEDGMENTS

First of all, I would like to express my deepest thanks and gratitude to my advisor, Dr. Emir Salih Magden, for allowing me to pursue my PhD under his supervision. As the first PhD student in his group, we worked closely, and I learned a lot from him. His guidance, patience, and support have been invaluable, and I am indebted to him. His vision and mindset will continue to guide me in my future career path.

I would like to thank Prof. Alper Kiraz, Assoc. Prof. Sedat Nizamoğlu, Assoc. Prof. Onur Ferhanoğlu, and Asst. Prof. Berna Morova for joining my thesis committee and for their guidance during my PhD research.

I acknowledge TUBITAK BIDEB for the financial support in the form of a PhD scholarship.

I would like to express my heartfelt gratitude to both former and current members of the Photonic Architecture Laboratories for creating a friendly and highly productive research environment. I would like to offer a special acknowledgment to Ali and Aycan, with whom I collaborated closely on the same project.

I would like to express my deepest gratitude to my beloved family, including my parents, sisters, and brothers.

Last but certainly not least, I would like to extend a heartfelt and special thank you to my beloved wife, Saliha, for her endless love and support. Her presence in my life has been an endless source of motivation and enthusiasm, especially during challenging times.

TABLE OF CONTENTS

List of Figures **ix**

Abbreviations **xiv**

Chapter 1: Introduction **1**

Chapter 2: Compact adiabatic silicon photonic filters with arbitrary and ultra-broadband response **6**

2.1 Introduction . . . 7

2.2 Coupled Mode Theory . . . 9

2.3 Device Structure . . . 13

2.4 Design Methodology . . . 16

2.5 Simulation of Adiabatic Filters . . . 19

2.6 Fabrication of the Devices and Measurement Setup . . . 22

2.7 Short-pass/Long-pass Filters . . . 23

2.8 Band-pass filters . . . 24

2.9 Coarse Wavelength Division Multiplexers . . . 31

2.10 Effect of Design Wavelength (λ_d) on Adiabatic Filter Design . . . 34

2.11 Effect of Width Deviation on the Filter Response . . . 37

2.12 Effect of Roll-off on Bandwidth . . . 39

2.13 Conclusion . . . 40

Chapter 3: On-chip Arbitrary Dispersion Engineering with Deep Photonic Networks **42**

3.1 Introduction . . . 42

3.2 Network architecture and optimization . . . 44

3.3 Experimental results 50
3.4 Conclusion 53

Chapter 4: Optimizing Photonic Devices Under Fabrication Variations with Deep Photonic Networks 55

4.1 Introduction 55
4.2 Photonic Network Architecture 58
4.3 Effect of Fabrication Variations on the Components 59
4.4 Fabrication Tolerant Device Optimization 61
4.5 Conclusion 69

Chapter 5: Conclusion 71

Bibliography 72

LIST OF FIGURES

1.1 The number of photonic components integrated on a single waveguide over time for three photonic integration platforms: InP substrate with integrated lasers, Si substrate without integrated lasers, and Si substrate with integrated lasers. retrieved from [Margalit et al., 2021] 3

2.1 Two uncoupled waveguides (left) and coupled waveguide system (right) [Lifante, 2003] 10

2.2 (a) Effective and (b) group indices of the fundamental transverse-electric mode of the single-segment (WG_1), three-segment (WG_3), five-segment (WG_5), and seven-segment (WG_7) waveguides. The width of the single-segment waveguide is 308 nm, widths of individual subwavelength layers of three-, five-, and seven-segment waveguides are 262 nm, 250 nm, and 247 nm, respectively. Gaps between the subwavelength layers are 150 nm. (c) Fundamental transverse electric mode profiles of WG_1 & WG_5 coupled waveguide configuration at wavelengths below and above the cutoff wavelength (λ_c). 14

2.3 Schematic of an adiabatic single-stage filter composed of coupled single-segment and five-segment waveguides. L_1, L_2, L_3, and L_4 are the lengths of four different transitions along the propagation direction. w(z) and s(z) are the width and separation of sections 2 and 3, respectively. 15

2.4 Schematic representation of single-segment to five-segment transition without (a) and with (b) adiabatic bends. Radii of curvature are: R1=40 µm and R2=80 µm. (c) 3D FDTD-simulated transmission results of the transitions in (a) and (b). 17
2.5 Optimized (a) width w(z) for section 2 and (b) separation s(z) for section 3, using three different ϵ bounds. The coupled waveguide system consists of a five-segment waveguide with 250 nm wide subwavelength segments separated by 150 nm gaps, and a single-segment waveguide with the target width of 308 nm. 20
2.6 (a) Simulated fraction of power in fundamental even and odd modes of the optimized single-stage filter designed with three different ϵ bounds. (b) Simulated transmission spectra of the single-stage filter with three different ϵ bounds. Inset shows close-up of the filter roll-off. Solid and dashed lines represent short-pass and long-pass outputs, respectively. (c) Roll-off and Total Length as a function of ϵ. Total Length is the sum of the adiabatic transition lengths for sections 2 and 3 (L_2+L_3). 21
2.7 Top: Images of the grating coupler-based measurement setup from two different perspectives. Bottom: Images of fibers aligned to the grating couplers of a device. 23
2.8 a) Layout of a single segment filter with grating coupler connections. b) Optical microscope image of input and output of one of the fabricated single segment filters. 24
2.9 Measurements of single segment filters with cut-off wavelengths of 1580 nm (top) and 1590 nm (bottom). 25
2.10 Block diagram of a double-stage filter composed of two cascaded filters with cutoff wavelengths of λ_{c1} and λ_{c2}. (b) Optical microscopy images taken from the input and output sections of a double-stage filter. . . . 26

2.11 Measured transmission spectra of the double-stage filters with bandwidths of (a) 96.6 nm, (b) 45.5 nm, (c) 25.7 nm, (d) 6.4 nm. Blue, orange, and red lines represent short-pass, band-pass, and long-pass outputs, respectively. 27
2.12 Illustrations of single and multi-channel optical communication links at the top and bottom, respectively 31
2.13 Coarse WDM connection diagram. 32
2.14 Coarse WDM connection diagram. 33
2.15 Measured transmission results of 8-channel coarse WDM. 33
2.16 Calculated (a) w(z) and (b) s(z) for three different $\Delta\lambda$. Calculated RHS of Eq. 2 as a function of (c) w and (d) s. ($\Delta\lambda = \lambda_c$-$\lambda_d$) 35
2.17 Simulated fraction of power in fundamental even and odd modes at three different $\Delta\lambda$. (b) Simulated transmission spectra of the single-stage filters designed at three different $\Delta\lambda$. 36
2.18 Simulated long-pass transmission spectra of the filter in (a) under-etch and (b) over-etch cases. Widths of both WG_1 and WG_5 are modified by the same amount, indicated by Δw. 38
2.19 Simulated long-pass transmission spectra of the filter in (a) under-etch and (b) over-etch cases. Widths of WG_1 and WG_5 are modified by different amounts. In the legends, the first and second values represent width deviations for WG_1 and WG_5, respectively. 39
2.20 Passband configurations of cascaded filters for (a) λ_{c1} and λ_{c2} are spectrally distant, (b) λ_{c1} and λ_{c2} are spectrally close. (IL: insertion loss, BW: 3dB-bandwidth) 40

3.1 a) Photonic network architecture composed of cascaded Mach-Zehnder interferometers (MZIs). b) Single MZI consisting of two splitters, implemented with directional couplers, and two tapers with custom geometries for achieving specific spectral phase profiles. c) Custom waveguide constructed from a set of trainable width parameters. . . . 45
3.2 Optimization cycle of photonic network. 47
3.3 Trained widths of dispersion optimized network. 48
3.4 Optimization monitor: L2 loss function at the top left (linear scale) and right (log scale) as a function of iteration. Learning rate at the bottom left. Sum of gradients of all parameters at the bottom right. . 49
3.5 a) Target and optimized dispersion profiles for a 2x12 sized network. b) Target and optimized transmittance responses of the same network. 50
3.6 Illustration of the interference-based dispersion measurement setup. . 51
3.7 a) Measured interference fringes and peak values of the two-port network optimized for a specific dispersion profile. b) Calculated group delay from interference fringes. c) Calculated dispersion from the group-delay. d) Measured transmission responses of the network. . . . 52
3.8 a) Schematic of 3-port photonic network architecture. b) Dispersion profile of a 3-port network optimized to have step-like dispersion. c) Dispersion profile of a 3-port network optimized to have a large dispersion. 53

4.1 Photonic network architecture two-port (a) and three port (b) illustraions. c) Single MZI consisting of two splitters, implemented with directional couplers, and two tapers with custom geometries for achieving specific spectral phase profiles. d) Custom waveguide constructed from a set of trainable width parameters. 59

4.2 3D illustration of directional coupler and its through port tranmission response under different under-etch and over-etch scenarios. Here Δw represents the width deviations. 60
4.3 3D illustration of custom waveguide taper and its phase response under different under-etch and over-etch scenarios. 62
4.4 Virtual wafer maps with correlation lengths of 1 mm (left and 4 mm (right)) 63
4.5 (Top) Illustration of a four-layer, two-port deep photonic network architecture. The optimized response of this network achieving a 50/50 splitting ratio, aligned with the designated objective. 64
4.6 Transmission spectra of the non-fabrication tolerant network calculated on different locations of a wafer map of correlation length of 4 mm and width deviation of 10 nm 65
4.7 Transmission spectra of the fabrication tolerant network calculated on different locations of a wafer map of correlation length of 4 mm and width deviation of 10 nm 66
4.8 Training loss of non-tolerant and tolerant power splitter optimizations. 66
4.9 Maximum deviation from 50% splitting ratio for tolerant and non-tolerant networks as a function of network size 67
4.10 Conventional (top) vs fabrication variation aware (bottom) design flows for photonic integrated circuits 69

ABBREVIATIONS

MZI	Mach-Zehnder interferometer
LIDAR	light detection and ranging
CMOS	complementary metal-oxide-semiconductor
FDTD	finite difference time domain
PIC	photonic integrated circuit
3D	three dimensional
SOI	silicon-on-insulator
MPW	multi-project-wafer
WDM	wavelength-division-multiplexing
AWG	arrayed waveguide grating
SWG	sub-wavelength grating
FSR	free spectral range
PDK	process design kit

Chapter 1

INTRODUCTION

Silicon photonics is the technology to integrate a large number of optical functions on a chip using CMOS fabrication technology [Soref, 2006, Chrostowski and Hochberg, 2015, Siew et al., 2021, Lim et al., 2013]. By leveraging the existing investments and research conducted in silicon semiconductor device processing over the decades, silicon photonics can achieve scalability, reliable manufacturing processes, and cost-effectiveness. Therefore, silicon photonics is rapidly maturing as a platform for large-scale photonic circuits and evolving from a research-based field to an industrially viable platform, mainly driven by communication applications, and enabled by the growing number of manufacturing facilities [Bogaerts and Chrostowski, 2018, Dong et al., 2014, Thomson et al., 2016].

Currently, there is a diverse range of material platforms available for constructing photonic integrated circuits, including III-V semiconductors (GaAs, InP), Lithium Niobate, glasses, polymers, and silicon [Bogaerts and Chrostowski, 2018, Liu et al., 2022a]. Each of these materials has its own advantages and limitations. For instance, III-V semiconductors excel in generating and detecting light at telecom wavelengths [Nagarajan et al., 2010], while Lithium Niobate offers highly efficient optical modulators [Zhu et al., 2021, Sohler et al., 2008]. Glasses and polymers are known for their ability to efficiently route light with minimal losses on a chip [Eldada and Shacklette, 2000, DeCorby et al., 2005].

However, silicon photonics stands out as a promising technology due to its compatibility with the manufacturing processes used in the CMOS industry. This compatibility enables the potential for high-volume production at a low cost per device. Another distinguishing characteristic of silicon photonics is its high refractive index contrast, which allows the scaling of waveguides to sub-micrometer dimensions. This, in turn, allows for the compact placement of numerous optical functions on the chip. The combination of these features makes silicon photonics the sole viable technology platform for the creation of large-scale, complex photonic integrated circuits.

Integrating photonic systems onto a chip offers many advantages, including improved performance, reliability, and the ability to incorporate complex functionality. The functionality of a photonic circuit on a chip doesn't rely on a single element but rather on the interconnectivity between multiple functional building blocks and sub-circuits. As a result, various components have been developed and demonstrated for performing different tasks within integrated photonic systems including light generation, coupling, routing, detection, processing, and modulation [Jalali and Fathpour, 2006].

After demonstration of electro-optic effect in silicon by Soref [Soref and Bennett, 1987], studies in silicon phase modulators [Zhao et al., 1995, Tang and Reed, 1995], one of the first building blocks of integrated photonics, has started. Subsequently, there was extensive research into SOI (silicon-on-insulator) waveguides [Rickman et al., 1994, Dumon et al., 2004], as they played a crucial role in enabling the integration of multiple components onto a chip. Progress continued with the demonstration of various passive and active integrated photonic components. These include splitters [Wang et al., 2016, Tao et al., 2008], crossings [Wu et al., 2020a], grating couplers [Cheng et al., 2020], edge couplers [Mu et al., 2020], filters [Liu et al., 2021], thermo-optic phase shifters [Liu et al., 2022b], photodetectors [Piels and Bowers, 2023], and modulators [Witzens, 2018]. These components collectively contribute to the expanding capabilities and functionalities of integrated photonic systems.

The number of devices incorporated into a single silicon photonic circuit continues to increase, thanks to the high device yield and the requirements of various applications [Shekhar et al., 2023]. The Figure 1.1 provides an overview of the progression in the number of photonic devices integrated onto a single waveguide across different platforms, including monolithic InP, monolithic Si, and heterogeneous InP/Si or GaAs/Si [Margalit et al., 2021]. During the early stages of silicon photonics development, small-scale photonic integrated circuits (PICs) were demonstrated, featuring high-speed pn junction modulators and photodetectors [Liu et al., 2004, Liao et al., 2005]. However, as the field advanced, the demand for more complex photonic circuits increased. This demand has been driven by a range of applications such as LIDAR [Yaacobi et al., 2014], photonic switching [Seok et al., 2019], photonic computing [Shastri et al., 2021], programmable circuits [Bogaerts et al., 2020], multiplexed biosensors [Reed et al., 2022], and spectroscopy [Subramanian et al., 2015].

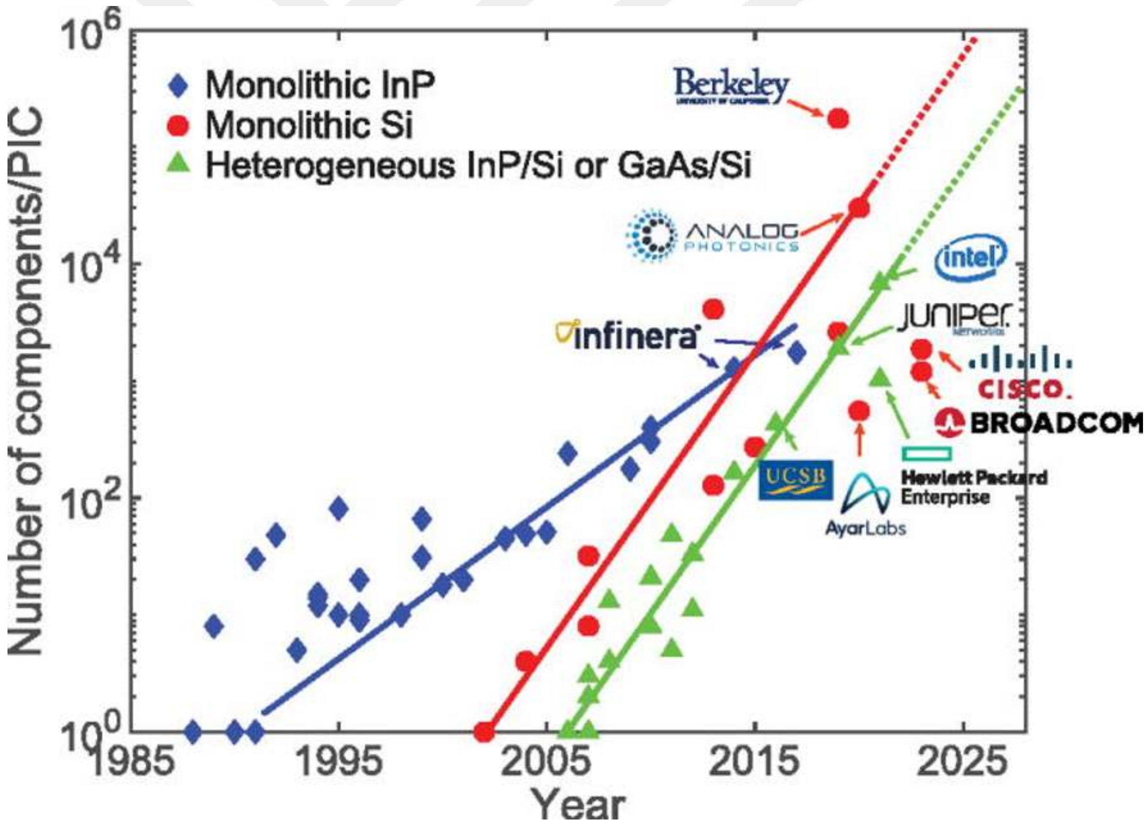

Figure 1.1: The number of photonic components integrated on a single waveguide over time for three photonic integration platforms: InP substrate with integrated lasers, Si substrate without integrated lasers, and Si substrate with integrated lasers. retrieved from [Margalit et al., 2021]

As photonic applications become increasingly complex, the design of customized

PICs with exceptional performance has become one of the most critical drivers of advancement in photonic systems. Many of the communication and spectroscopy applications require high-performance and wideband optical filters for the development of next-generation broadband photonic systems. Moreover, in applications like microwave photonics, photonic computing, and sensing, stringent performance requirements necessitate the optimization of complex photonic geometries. To make the design process more time-efficient and to improve the device performance new design methods need to be developed.

This thesis presents the design of broadband silicon photonic filters as well as optimization of deep photonic networks assisted multi-objective complex photonic devices:

In chapter 2, we present the design, simulation, and experimental demonstration of compact and ultra-broadband silicon photonic filters with adiabatic waveguides. We first developed an optimization algorithm for coupled adiabatic waveguide structures, and used it to design individual, single-cutoff spectral filters and experimentally demonstrated. Both outputs of the filters operate in transmission, making it possible to cascade multiple filters in different configurations. Taking advantage of this flexibility, we cascade two filters with different cutoff wavelengths on-chip, and experimentally demonstrate band-pass operation. The independent and flexible design of these band edges enables filters with bandwidths well over 100 nm. Experimentally, we demonstrated band-pass filters with passbands ranging from 6.4 nm up to 96.6 nm. Our devices achieve flat-band transmission in all three of the short-pass, band-pass, and long-pass outputs with less than 1.5 dB insertion loss and extinction ratios of over 15 dB. We then cascaded multiple of these filters in a tree configuration and experimentally demonstrated a multiplexer in S, C, L bands.

In chapter 3, we propose on-chip deep photonic networks providing arbitrarily defined dispersion profiles with custom designed Mach-Zehnder interferometers (MZIs). We created a custom framework for the simulation and optimization of these tapers by rapid transfer matrix evaluations. The framework allows for optimization of the dispersion and transmission simultaneously. We demonstrated a proof-of-concept device having triangular dispersion over a 40 nm spectrum in C-band. A flat band transmission is achieved in this band with less than 0.7 dB insertion loss. We also showed increasing design of freedom allows for arbitrary transfer function realizations.

In chapter 4, We propose a deep photonic interferometer network architecture for designing fabrication-tolerant photonic devices. Our framework employs variation-aware, custom-designed MZIs and virtual wafer maps to optimize broadband power splitters under fabrication variations. Notably, we successfully demonstrate 50/50 splitters with deviations below 1% from the desired 50/50 ratio, even when facing up to 10 nm over-etch and under-etch variations.

Chapter 2

COMPACT ADIABATIC SILICON PHOTONIC FILTERS WITH ARBITRARY AND ULTRA-BROADBAND RESPONSE

Broadband spectral filters are highly sought-after in many integrated photonics applications such as ultra-broadband wavelength division multiplexing, multi-band spectroscopy, and broadband sensing. In this chapter, we present the design, simulation, and experimental demonstration of compact and ultra-broadband silicon photonic filters with adiabatic waveguides. We first develop an optimization algorithm for coupled adiabatic waveguide structures, and use it to design individual, single-cutoff spectral filters. These single-cutoff filters are 1×2 port devices that optimally separate a broadband signal into short-pass and long-pass outputs, within a specified device length. We control the power roll-off and extinction ratio in these filters using the adiabaticity parameter. Both outputs of the filters operate in transmission, making it possible to cascade multiple filters in different configurations. Taking advantage of this flexibility, we cascade two filters with different cutoff wavelengths on-chip, and experimentally demonstrate band-pass operation. The independent and flexible design of these band edges enables filters with bandwidths well over 100 nm. Experimentally, we demonstrate band-pass filters with passbands ranging from 6.4 nm up to 96.6 nm. Our devices achieve flat-band transmission in all three of the short-pass, band-pass, and long-pass outputs with less than 1.5 dB insertion loss and extinction ratios of over 15 dB. These ultra-broadband filters can enable new capabilities for multi-band integrated photonics in communications, spectroscopy, and sensing applications.

This chapter is based on the publication [Gorgulu and Magden, 2023]: Gorgulu, Kazim, and Emir Salih Magden. "Ultra-broadband integrated optical filters based on adiabatic optimization of coupled waveguides." Journal of Lightwave Technology (2023).

2.1 Introduction

Integrated optical filters are one of the main building blocks in photonic integrated circuits and are commonly used in communications [Miller, 2009, Doerr, 2015, Lam et al., 2010, Shi et al., 2020], spectroscopy [Yang et al., 2021, Xia et al., 2011, Nitkowski et al., 2008], and sensing [Luan et al., 2018, Fernández Gavela et al., 2016, De Vos et al., 2007]. Many of these applications require high-performance and wideband optical filters for the development of next-generation broadband photonic systems. Efficiently splitting and combining ultra-broadband signals is crucial in wideband wavelength division multiplexing to enable transmission beyond the typical communication bands to increase optical networks' transport capacities [Lam et al., 2010, Shi et al., 2020, Okamoto et al., 2019, Doerr et al., 2016]. Broadband filtering can also be utilized for increasing the operation bandwidth of narrowband spectroscopy [Yang et al., 2021, Misra et al., 2020, Zheng et al., 2019], or separating different spectral components in dual-comb spectroscopy [Dutt et al., 2018] to enhance measurement resolution and signal-to-noise ratio.

So far, many different structures have been presented for implementing integrated optical filters. Among these, ring resonators [Bogaerts et al., 2012, Biberman et al., 2012, Ye et al., 2021], Mach-Zehnder interferometers (MZIs) [Horst et al., 2013, Xu and Shi, 2017, Mikkelsen et al., 2018], arrayed waveguide gratings (AWGs) [Wang et al., 2014, Pathak et al., 2013], and echelle gratings [Brouckaert et al., 2007, Pathak et al., 2014] have been studied extensively. As these structures achieve spectral filtering through interference and waveguide dispersion, their bandwidths can typically reach about 30 nm [Pathak et al., 2014, Liu et al., 2021], limiting their usability in applications requiring wider passbands. Due to their limited operation bandwidths, these filters are primarily used in narrowband spectral filtering and multiplexing applications [Liu et al., 2021]. Cascaded ring resonators [Chen et al., 2014] and subwavelength grating (SWG)-assisted MZIs [Sumi et al., 2018] have also been demonstrated with flat-top and broader-band operation but have only achieved up to about 40 nm-wide bandwidths so far. In general, system design with these interferometric filters requires careful consideration of their free spectral ranges (FSR), especially for broadband filtering [Liu et al., 2021]. On the other hand, Bragg grating-based optical filters can be designed with FSR-free operation [Cheng and Chrostowski, 2020, Chen et al., 2013]. However, these Bragg grating filters work in reflection mode and thus require an additional optical circulator or directional coupler for signal routing, significantly increasing insertion loss and integration complexity. In comparison, Bragg grating-based contra-directional couplers can allow for add-drop filtering configurations without requiring optical circulators [Yun et al., 2019, Hammood et al., 2019, Naghdi and Chen, 2016]. Yet, despite their good extinction ratios, these filters have so far only achieved optical bandwidths up to 35 nm, due to the limited coupling strength of forward and backward propagating modes. More recently, a broader-band design of the contra-directional Bragg grating filter was demonstrated by chirping the grating period [Hammood et al., 2021], with passbands reaching up to 11 THz (approximately 88 nm). However, this method results in much longer device lengths, and presents an inherent design tradeoff between extinction ratio and device bandwidth.

Unlike these grating-based or typical interferometric devices, couplers based on adiabatic waveguide transitions present an important class of integrated photonic devices that are particularly suitable for broadband operation. An adiabatic coupler is typically designed to maintain the propagating optical signal in a single eigenmode through a waveguide whose cross-section slowly evolves in the propagation direction [Sun et al., 2009, Siriani and Tambasco, 2021, Wu et al., 2020b]. While many adiabatic devices have been demonstrated for broadband polarization rotation [Dai and Bowers, 2011, Chung and Tseng, 2018], mode multiplexing [Guo and Chu, 2017, Gross et al., 2014], and power splitting [Han et al., 2018, Hung et al., 2019], adiabatic couplers can also be used for on-chip broadband filtering [Magden et al., 2018, Menchon-Enrich et al., 2013, Lin et al., 2021, Gorgulu and Magden, 2022, Gorgulu and Magden, 2021]. These adiabatic filters rely on the phase mismatch between coupled waveguide modes at different wavelengths while achieving broadband operation through slowly varying waveguide cross-sections. However, these filters must be made sufficiently long to satisfy the desirable extinction ratio and roll-off performance. Typical lengths of these filters vary from several millimeters to centimeters, significantly reducing their integration density and also introducing unwanted propagation losses.

In this study, we demonstrate integrated photonic filters based on adiabatic structures combining broadband responses with compact footprints through an independent design of band edges in a cascaded structure. We first present a design methodology for compact, single-cutoff, 1×2-port adiabatic filters by optimizing the adiabaticity parameter through a slowly-varying, coupled waveguide structure. The resulting device acts as a single-cutoff filter separating the input signal into short-pass and long-pass outputs. We show that this filter's performance metrics can be controlled by an upper bound on the power coupled out of the fundamental mode, specifically by varying the adiabaticity parameter. The cutoff wavelength of these single-cutoff filters can be adjusted by modifying the cross-sectional geometry of the coupled waveguides. This flexibility allows us to design band-pass filters by cascading two of these single-cutoff filters, designed independently at different cutoff wavelengths. With this configuration, we experimentally demonstrate band-pass filters with bandwidths ranging from 6.4 nm to as wide as 96.6 nm, with inherently flat-top and low-loss transmission.

2.2 Coupled Mode Theory

The design of the adiabatic filter is based on the evolution of coupled waveguides along the propagation direction. Therefore, in this section we will review the coupled mode theory.

A waveguide structure which is invariant along the propagation direction supports several modes and these modes are orthogonal to each other. All of these modes are called eigenmodes of this linear waveguide system. If the waveguide system is modified by a small amount, previously found modes are no longer eigenmodes of the new structure. Therefore, they will start to couple each other.

To determine the eigenmodes of the modified system, two methods are commonly employed. In the first method, one can calculate the eigenmodes by using Maxwell's equations and the new boundary conditions. This method gives the exact solution for the modes. However, sometimes it might be too difficult to solve it for some coupled waveguide geometries and thus some numeric techniques might be required (finite difference eigenmode method etc.). In the second method, one can express the modes of the new structure as a linear combination of modes of the individual waveguides. This method is called coupled mode theory and provides accurate results for relatively weakly coupled waveguide systems

An optical wave in a waveguide can be expressed as linear combination of guided modes and radiation modes. In most cases it is sufficient to consider first two guided modes. Figure 2.1 shows two uncoupled waveguides (left) and a coupled waveguide system (right) [Lifante, 2003]. In this figure, ψ_a and ψ_b represent the individual modes of the uncoupled waveguides, with propagation constants β_a and β_b, respectively. In the absence of coupling they obey following differential equations:

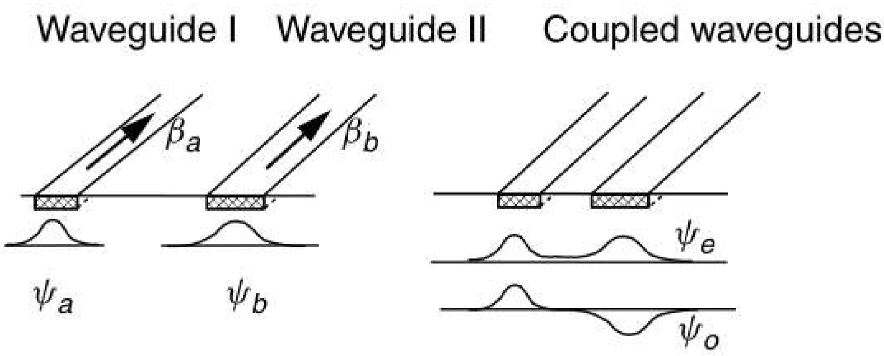

Figure 2.1: Two uncoupled waveguides (left) and coupled waveguide system (right) [Lifante, 2003]

$$\frac{d}{dz}\psi_a = -j\beta_a\psi_a \tag{2.1}$$

$$\frac{d}{dz}\psi_b = -j\beta_b\psi_b \tag{2.2}$$

Lets assume that we bring these two waveguides together and they become weakly coupled. In this case new set of differential equations will be:

$$\frac{d}{dz}\psi_a = -j\beta_a\psi_a + \kappa_{ab}\psi_b \tag{2.3}$$

$$\frac{d}{dz}\psi_b = -j\beta_b\psi_b + \kappa_{ba}\psi_a \tag{2.4}$$

Equations (2.3) and (2.4) form a system of first order linear differential equations. We can write this in matrix form:

$$\begin{bmatrix} \psi_a^{'} \\ \psi_b^{'} \end{bmatrix} = \begin{bmatrix} -j\beta_a & \kappa_{ab} \\ \kappa_{ba} & -j\beta_b \end{bmatrix} \begin{bmatrix} \psi_a \\ \psi_b \end{bmatrix} \tag{2.5}$$

$$\psi^{'} = A\psi \tag{2.6}$$

Equation (2.5) is an eigenvalue problem. In our current basis, the two components of the mode vector represent the modes of the individual uncoupled waveguides. This basis is a natural choice, but we will instead use the eigenvectors of the above matrix as our basis, allowing us to diagonalize the matrix and thus uncouple the differential equations.

For waveguides carrying power in the same direction, power conservation requires that $\kappa_{ab}\kappa_{ba} = -|\kappa_{ab}|^2 \rightarrow \kappa_{ab} = -\kappa_{ba}^*$ [Haus, 1984].

Let $\kappa_{ab} = -\kappa_{ba}^* = -j\kappa$. Then, equation (2.5) can be rewritten as

$$\begin{bmatrix} \psi_a^{'} \\ \psi_b^{'} \end{bmatrix} = \begin{bmatrix} -j\beta_a & -j\kappa \\ -j\kappa^* & -j\beta_b \end{bmatrix} \begin{bmatrix} \psi_a \\ \psi_b \end{bmatrix} \tag{2.7}$$

Lets assume that $\psi_\pm$ are the eigenvectors of this system with corresponding eigenvalues $\beta_\pm$. Assuming $-j\beta_\pm z$ dependence,

$$\begin{bmatrix} -j(\beta_a - \beta_\pm) & -j\kappa \\ -j\kappa^* & -j(\beta_b - \beta_\pm) \end{bmatrix} \psi_\pm = 0 \tag{2.8}$$

Setting determinant zero, we get

$$(\beta_a - \beta) * (\beta_b - \beta) - |\kappa|^2 = 0 \tag{2.9}$$

Solution of this quadratic equation is:

$$\beta_\pm = \frac{\beta_a + \beta_b}{2} \pm \sqrt{\left(\frac{\beta_a - \beta_b}{2}\right)^2 + |\kappa|^2} \tag{2.10}$$

We define the following parameters and rewrite the eigenvalues.

$$\bar{\beta} = \frac{\beta_a + \beta_b}{2},\ \delta = \frac{\beta_a - \beta_b}{2},\ S = \sqrt{\delta^2 + |\kappa|^2} \tag{2.11}$$

$$\beta_\pm = \bar{\beta} \pm \sqrt{\delta^2 + |\kappa|^2} \tag{2.12}$$

Here, the eigenvalues ($\beta_\pm$) of the system are also referred as even (β_e) and odd (β_o) propagation constants, and the corresponding eigenvectors ($\psi_\pm$) of this system are referred as even (ψ_e) and odd (ψ_o) supermodes. These modes are the eigenmodes of the coupled system and they are orthogonal to each other (Figure 2.1 right). We found the eigenvalues (propagation constants), and the next step is finding the eigenvectors(supermodes) of the system. We will put the solution for β_+ into equation (2.8) and solve for ψ_+:

$$\begin{bmatrix} -j(\delta - S) & -j\kappa \\ -j\kappa^* & -j(-\delta - S) \end{bmatrix} \begin{bmatrix} \eta_1 \\ \eta_2 \end{bmatrix} = 0 \tag{2.13}$$

From (2.13) we get $\frac{\eta_1}{\eta_2} = \frac{\kappa}{S-\delta}$. Therefore ψ_+ will be:

$$\psi_+ = \alpha \begin{bmatrix} \kappa \\ S-\delta \end{bmatrix} \tag{2.14}$$

where α is a constant and will be used for normalization of ψ_+.

$$\alpha = \sqrt{\frac{1}{\kappa^2 + (S-\delta)^2}} \tag{2.15}$$

$$\psi_+ = \frac{1}{\sqrt{2}} \begin{bmatrix} \sqrt{1+\delta/S} \\ \sqrt{1-\delta/S} \end{bmatrix} \tag{2.16}$$

Following similar steps for ψ_-:

$$\psi_- = \frac{1}{\sqrt{2}} \begin{bmatrix} -\sqrt{1-\delta/S} \\ \sqrt{1+\delta/S} \end{bmatrix} \tag{2.17}$$

Equations (2.16) and (2.17) are the normalized representations of the even and odd supermodes with their components being the amplitudes of the two individual waveguide modes.

2.3 Device Structure

The adiabatic filter design uses a coupled waveguide system with two specifically engineered waveguides that are designed to be phase-matched only at a single cutoff wavelength (λ_c), and phase-mismatched otherwise. The spectral filtering operation is based on placing these two waveguides in close proximity, where the combined structure results in spatial separation of the fundamental modes at short ($\lambda < \lambda_c$) and long ($\lambda > \lambda_c$) wavelengths, on either side of the band edge at the cutoff wavelength. This is made possible through a difference in the group indices of the two waveguides within the desired operation band of the device. For this purpose, our first waveguide is designed using laterally-arranged, multi-segment subwavelength structures with specific effective index and dispersion properties. As demonstrated in Figure 2.2a, with increasing number of segments, this first waveguide more closely resembles a uniform material, with a flatter effective index profile. Our second waveguide is a typical strip waveguide, with a significantly different effective index profile. As plotted Figure 2.2b, a multi-segment waveguide with more segments has a smaller group index. As such, with more segments, the group index difference between the single-segment and the multi-segment waveguides grows . This higher difference in the group indices results in better confinement of the fundamental mode to the intended waveguide and enhances filter roll-off. However, with increased number of segments, the two waveguides are separated farther, reducing coupling strength between them, and resulting in longer devices overall. Therefore, we designed our filters using the single-segment (WG_1) & five-segment (WG_5) waveguide configuration.

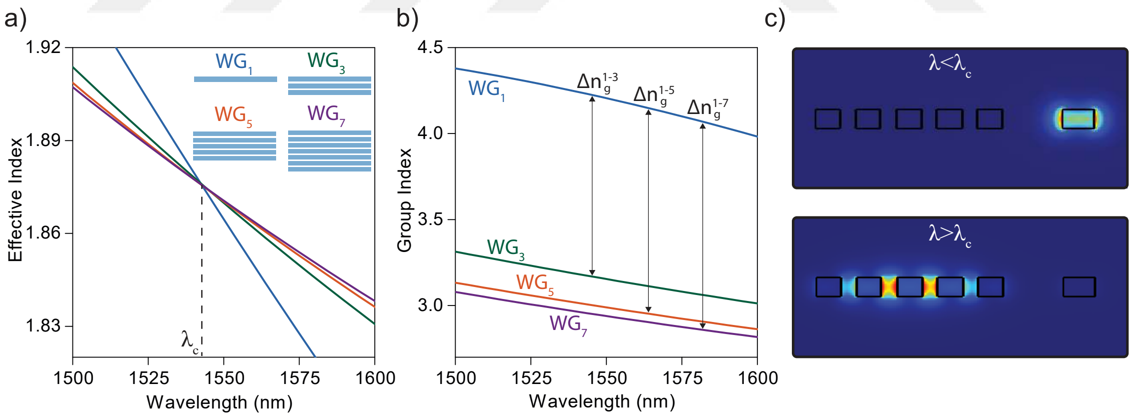

Figure 2.2: (a) Effective and (b) group indices of the fundamental transverse-electric mode of the single-segment (WG_1), three-segment (WG_3), five-segment (WG_5), and seven-segment (WG_7) waveguides. The width of the single-segment waveguide is 308 nm, widths of individual subwavelength layers of three-, five-, and seven-segment waveguides are 262 nm, 250 nm, and 247 nm, respectively. Gaps between the subwavelength layers are 150 nm. (c) Fundamental transverse electric mode profiles of WG_1 & WG_5 coupled waveguide configuration at wavelengths below and above the cutoff wavelength (λ_c).

Figure 2.2c shows the fundamental electric field profiles of this coupled waveguide structure (WG_1 & WG_5) for wavelengths below and above the filter cutoff. In general, majority of the fundamental mode is spatially confined around the waveguide with the higher effective index. Therefore, the fundamental mode is confined mainly around the single-segment waveguide at short wavelengths and around the multi-segment waveguide at long wavelengths. Such mode confinement onto separate waveguides at different wavelengths enables spectral splitting of short and long wavelengths to respective output ports.

The adiabatic filter is created from these two waveguides (WG_1 and WG_5), using slowly varying transitions as shown in Figure 2.3. The geometry of the filter is separated into four different adiabatic transitions along the propagation direction, with lengths of L_1, L_2, L_3, and L_4. In section 1, WG_5 is created by transforming a single-segment input waveguide to the five-segment design. Towards to the end of this section, WG_1 is introduced adjacent to WG_5. In section 2, the width of the WG_1, (w(z)) is slowly tapered up. In section 3, WG_5 and WG_1 are gradually separated, using the separation s(z). Finally, in section 4, WG_5 is transformed back into a single-segment output waveguide; and WG_1 is also tapered to the correct output waveguide width.

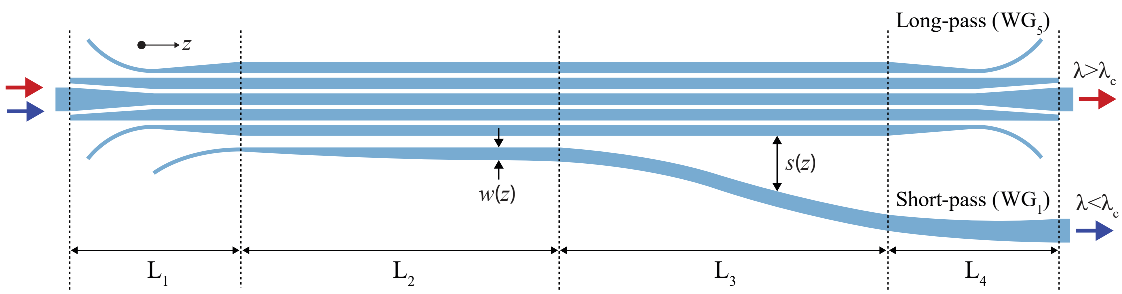

Figure 2.3: Schematic of an adiabatic single-stage filter composed of coupled single-segment and five-segment waveguides. L_1, L_2, L_3, and L_4 are the lengths of four different transitions along the propagation direction. w(z) and s(z) are the width and separation of sections 2 and 3, respectively.

2.4 Design Methodology

We used 35 µm-long linear tapers for sections 1 and 4, as these only include transitions within WG_1, and near-lossless transmission is easily achieved through typical linear transitions. The single-segment waveguide and the five-segment waveguide are slowly evolved into one another through adiabatic transitions. One possible design for these transitions involves using linear tapers from the single-segment waveguide to the five-segment waveguide as shown in Figure 2.4a. However, abrupt introduction of new adjacent segments can potentially lead to undesired losses. Using the 3D finite difference time domain (FDTD) method we calculated the transmitted power of the fundamental mode for this transition. We used fundamental TE mode as the input and then calculated the amount of power transmitted to the fundamental mode at P-plane. As shown in Figure 2.4c (black line), more than 1% of the power is lost within this transition. In order to reduce this loss, we utilized adiabatic bends when introducing the outermost segments in this transition as shown in Figure 2.4b. Transmission plot (red line in Figure 2.4c) shows that the amount of power lost is significantly reduced when the adjacent waveguides are introduced to the structure through these bends.

In contrast, the design of sections 2 and 3 present significant challenges and tradeoffs between device performance and footprint. Specifically, our design variables w(z) and s(z) need to be carefully optimized in order to minimize power lost to the unwanted waveguide, while still maintaining reasonable section lengths. We describe this as an optimization problem in coupled mode theory [Haus, 1984] for adiabatically transforming the fundamental mode while minimizing excitation of the higher order modes.

We use the variable $\gamma = \Delta/\kappa$ to express the amount of power in either one of the two waveguides as a function of wavelength, where $\Delta = (\beta_5 - \beta_1)/2$ is the mismatch of propagation constants between the individual (uncoupled) modes of WG_5 and WG_5, and κ is the coupling coefficient between these two modes. We model sections 2 and 3 individually, as cascades of successive transitions determined by w(z) and

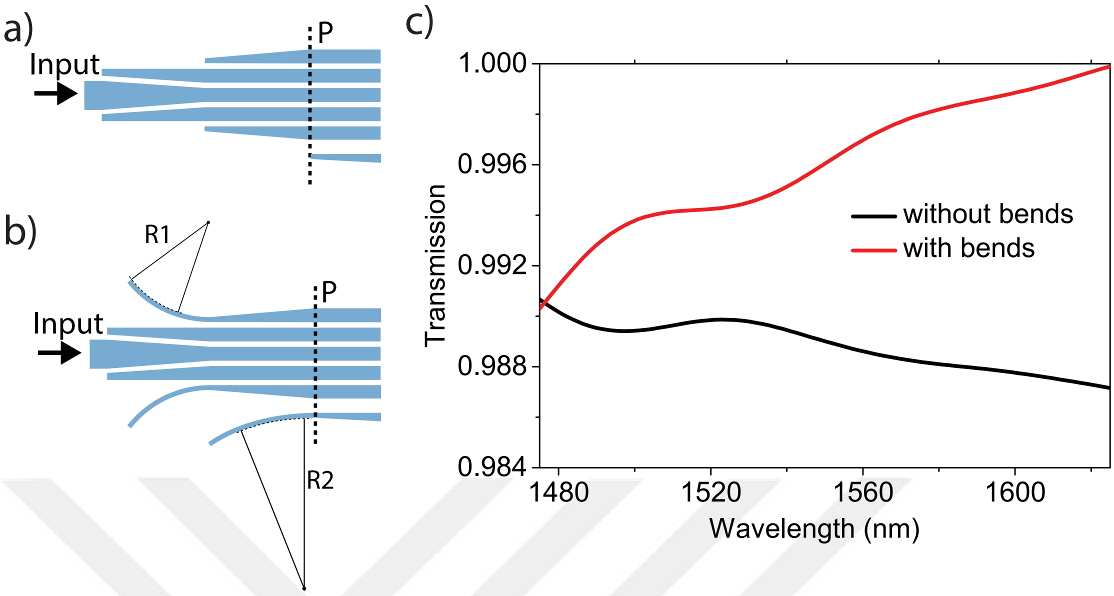

Figure 2.4: Schematic representation of single-segment to five-segment transition without (a) and with (b) adiabatic bends. Radii of curvature are: R1=40 µm and R2=80 µm. (c) 3D FDTD-simulated transmission results of the transitions in (a) and (b).

s(z), respectively. As such, the evolution of these parameters along the propagation direction directly influences how the variable γ changes throughout the device. This is critical in limiting the unwanted power loss to higher order modes to a minimum, since the adiabaticity criterion indicates that

$$\frac{1}{2\kappa(1+\gamma^2)^{3/2}}\frac{d\gamma}{dz} \leq \sqrt{\epsilon} \tag{2.18}$$

where ϵ is the fraction of power lost from the fundamental mode [Sun et al., 2009]. Here, we consider power coupling between only the fundamental even and odd modes. By design, as the optical input to our filter geometry is always in the fundamental even mode, the amount of power lost to the odd mode determines how much power is coupled to the adjacent waveguide. The parameter ϵ is an upper bound on this power, from which $\gamma(z)$ can be optimized for the shortest possible adiabatic transition. In sections 2 and 3 of our filters, the dimensions and separation between waveguides vary significantly making κ also a function of z. For this reason, we use a numerical method for the solution of $\gamma(z)$ in these two sections for a given upper bound ϵ as detailed below. We first select the initial (w_0 and s_0) as well as final target (w_T and s_T) dimensions for each section. Here, w_T is determined based on the desired cutoff wavelength; and s_T is chosen to be approximately 1500 nm so that no significant further coupling can occur between the two waveguides after they are separated. We then choose a design wavelength (λ_d) slightly shorter than the cutoff wavelength. The design wavelength parameter influences performance metrics of the filters and will be discussed in the following section. Using a mode solver at this design wavelength, we solve for and record the fundamental transverse-electric (TE) mode profile of WG_1 as a function of its width, w. We also record the fundamental TE mode-profile of WG_5, for which the cross-section remains constant throughout these two sections. Using these mode profiles, we created lookup tables by calculating the coupling coefficient κ using its overlap integral definition [48] and the corresponding γ, both as functions of w and s. Then, starting from the initial width (w_0) for section 2, and the initial separation (s_0) for section 3, we discretize and solve Eq. 1 in steps of Δz along the propagation direction according to the following algorithm, yielding w(z) and s(z).

given w_0 (or s_0) at z = 0, read γ_0 and κ_0 from lookup tables

while $w_n < w_T$ (or $s_n < s_T$)

find the next γ by $\gamma_{z+\Delta z} = \gamma_z + 2\kappa_z(1+{\gamma_z}^2)^{3/2}\sqrt{\epsilon}\Delta$

using $\gamma_{z+\Delta z}$ read $w_{z+\Delta z}$ (or $s_{z+\Delta z}$) from lookup tables

using $w_{z+\Delta z}$ (or $s_{z+\Delta z}$) read $\kappa_{z+\Delta z}$ from lookup tables

increment z = z + Δz

end

To illustrate the performance of our filters created with this algorithm, we designed an example adiabatic filter with a five-segment waveguide consisting of 250 nm-wide subwavelength segments separated with 150 nm gaps, and a single-segment waveguide with the target width of w_T = 308 nm. We also chose λ_d to be 16 nm shorter than the cutoff wavelength. For these parameter selections in section 2, the optimized w(z) for three different ϵ bounds are plotted in Figure 2.5a. Here, w(z) adiabatically evolves starting from the initial width of $w_0 = 230$ nm, below which we find that there is practically no coupling. In this algorithm, the device length is not subject to any direct constraints, but instead is determined by the selection of ϵ. As expected, imposing tighter bounds on ϵ to limit the power coupled to the unwanted odd mode results in longer transitions. We also observe that w(z) evolves rapidly at the beginning of the section where power coupling is minimal but slows down significantly towards the end as it approaches the target w_T with increased coupling. Similarly for section 3, we plot the optimization result of s(z), from an initial separation of $s_0 = 200$ nm to a final target of $s_T = 1500$ nm in Figure 2.5b. Similar to section 2, our algorithm returns longer optimal lengths for this section with tighter bounds on ϵ. The optimized s(z) evolves slowly at the beginning of the section due to stronger coupling, and changes much faster towards the end as the two waveguides are separated farther.

2.5 Simulation of Adiabatic Filters

In order to model the filtering performance of this single-stage filter, we used the transfer matrix method to simulate the adiabatic transitions in sections 2 and 3. Figure 2.6a shows the fraction of powers in the fundamental even and odd modes for three separate filters designed with different ϵ bounds. As seen in this figure, the fraction of the power in the odd mode is suppressed in the entire spectrum of interest except for the region around the cutoff. This is the spectral region where the difference between the propagation constants of the individual waveguides (β_5 and β_1) is the smallest, resulting in increased coupling between these waveguides. Therefore, suppressing the power lost to the odd mode is significantly more challenging around the cutoff, and requires slower transitions. With tighter ϵ bounds, our design algorithm creates slower transitions, resulting in a faster decrease of power in the odd mode around the cutoff region, which is necessary for enabling sharp filter roll-offs.

The transmission at the two outputs (short-pass and long-pass) for three dif-

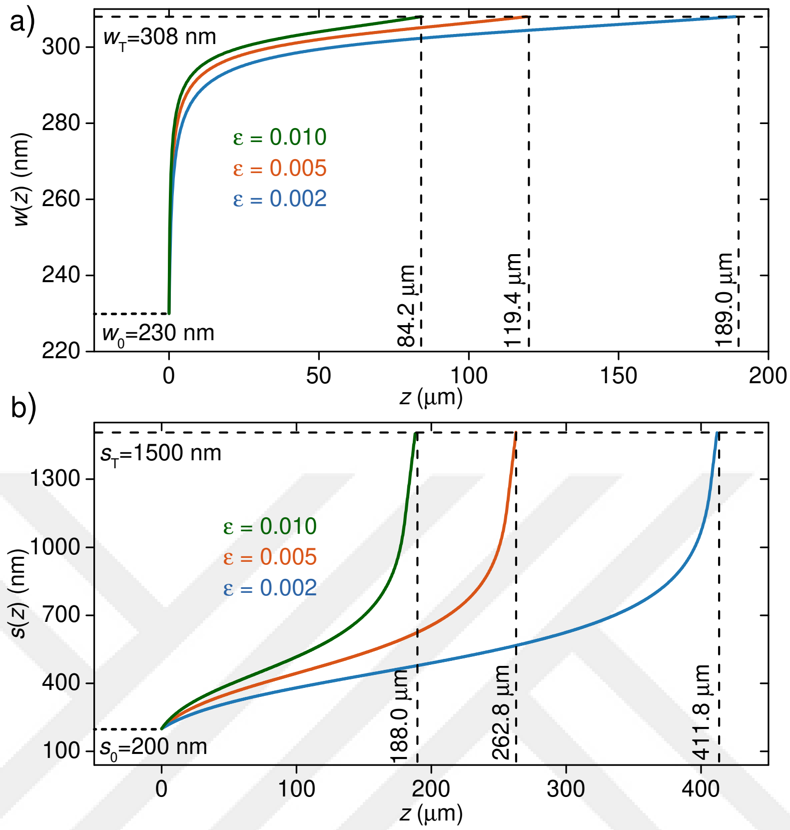

Figure 2.5: Optimized (a) width w(z) for section 2 and (b) separation s(z) for section 3, using three different ϵ bounds. The coupled waveguide system consists of a five-segment waveguide with 250 nm wide subwavelength segments separated by 150 nm gaps, and a single-segment waveguide with the target width of 308 nm.

ferent ϵ bounds is plotted in Figure 2.6b. These results verify the expected flat-top pass-bands due to the inherent near-lossless transmission through the adiabatic structures. Since ϵ represents the amount of power allowed to couple to the odd mode, it directly affects the extinction ratio of the filter, where a smaller ϵ results in better extinction. The filters also exhibit sharper roll-offs with tighter ϵ bounds, as the power in odd mode around the cutoff wavelength shrinks with decreasing ϵ. We plot this roll-off and the resulting device length (L_2+L_3) as a function of the ϵ parameter in Figure 2.6c. The roll-off here is calculated as the numerical gradient of the transmission at -3 dB. This result clearly illustrates the design tradeoff between filter roll-off and device length. Filters with sharper roll-offs can be obtained by

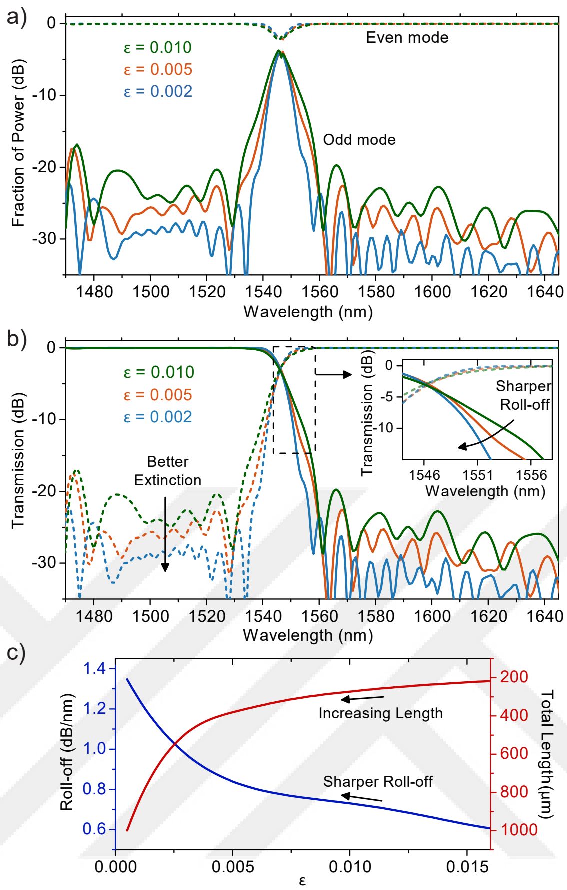

Figure 2.6: (a) Simulated fraction of power in fundamental even and odd modes of the optimized single-stage filter designed with three different ϵ bounds. (b) Simulated transmission spectra of the single-stage filter with three different ϵ bounds. Inset shows close-up of the filter roll-off. Solid and dashed lines represent short-pass and long-pass outputs, respectively. (c) Roll-off and Total Length as a function of ϵ. Total Length is the sum of the adiabatic transition lengths for sections 2 and 3 (L_2+L_3).

running the algorithm with smaller ϵ, but at the expense of longer device lengths. The specific selection of the design wavelength (λ_d) also influences this filter roll-off. As this design wavelength approaches the cutoff wavelength of the filter, γ (and the resulting w(z) and s(z)) are optimized in order to provide a sharper spectral change in the filter transmission. We observed that as λ_d approaches λ_c, the transition length slightly decreases for section 2, but significantly increases for section 3. Once again, this choice also presents a tradeoff between sharper roll-offs and overall device lengths. Considering these tradeoffs between ϵ or λ_d parameters and the resulting device length, our design algorithm can be used to produce filters with varying extinction and roll-off metrics, with lengths ranging from hundreds of micrometers to several millimeters.

2.6 Fabrication of the Devices and Measurement Setup

We used a commercial software IPKISS [Bogaerts et al., 2016] design system for transferring the designed filters to the layout. IPKISS is a design system specializing in photonic circuit design. IPKISS has an interface written in Python programming language. In this software, special parametric cells can be defined where all the features of any structure called PCell can be gathered in one place. In this way, we can create a library of our own custom structures and use them over and over again.

For the fabrication of our filters, we worked with Imec [Imec,], which is part of the Europractice consortium. Imec provided us with the process design kit (PDK), a file containing the library of the general structures they created and the requirements they set for the custom structures. We used grating and edge couplers and waveguides readily available in PDK to couple light from fiber to our designs.

The setup shown in 2.7 was set up to measure the fabricated adiabatic devices. As seen in this setup, measurements were made in the E, C, L bands, with a tunable laser. The light in the fiber was transferred to the waveguides on the chip with grating couplers, and measurements were made with an optical power meter. Since the grating couplers work in single polarization, the optical signal obtained from the laser was sent to the chip with the integrated photonic device, using a polarization controller.

Two cameras are placed on movable plates at different angles so that the connection between the chip input and output fiber ends and the chip can be created more easily. At the same time, the fiber holders positioned on the grating couplers on the chip and the plate on which the chip is placed are placed on the plates with precision movement capability. Thanks to this precise movement, the chip is positioned with the least loss and with the same precision ($\Delta < 1\ \mu m$) as possible each time. Photographs of this measuring setup from different angles and examples of

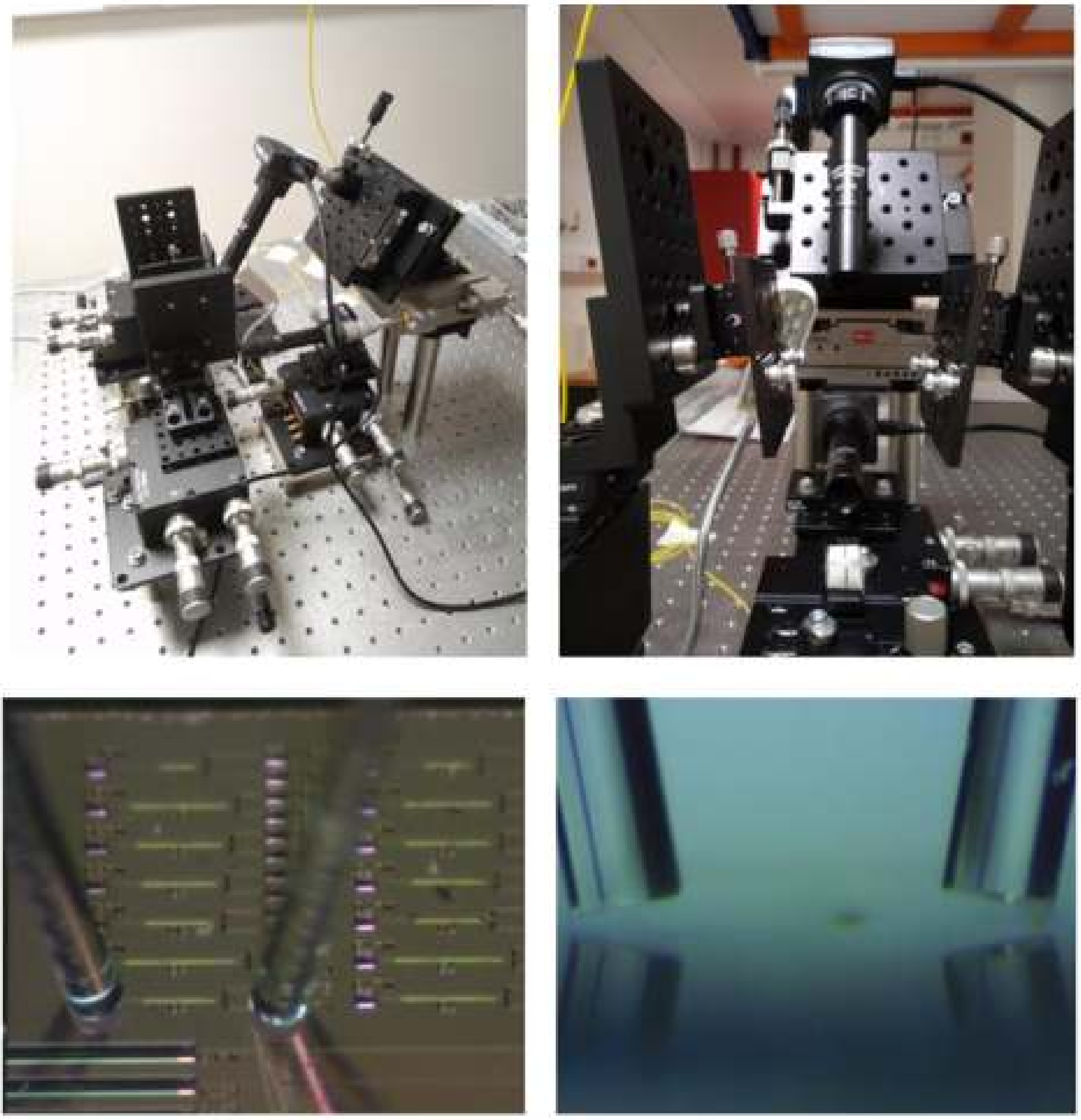

Figure 2.7: Top: Images of the grating coupler-based measurement setup from two different perspectives. Bottom: Images of fibers aligned to the grating couplers of a device.

fibers approached to the chip are shown in 2.7.

2.7 Short-pass/Long-pass Filters

By controlling the size of the waveguides used in adiabatic transitions, we designed filters operating at different cut-off wavelengths. Considering the previously mentioned design parameters, we chose ϵ around 0.0015 to achieve high extinction and roll-off speed, while keeping the overall device length under 1 mm. We created the layout of these filters and fabricated these filters through Imec's Multi-Project-Wafer service. Figure 2.8a shows the layout of a single segment filter. Its one input on the left and two outputs on the right are connected to the grating couplers. 2.8b shows the optical microscope image of input and output of one of the fabricated single segment filters.

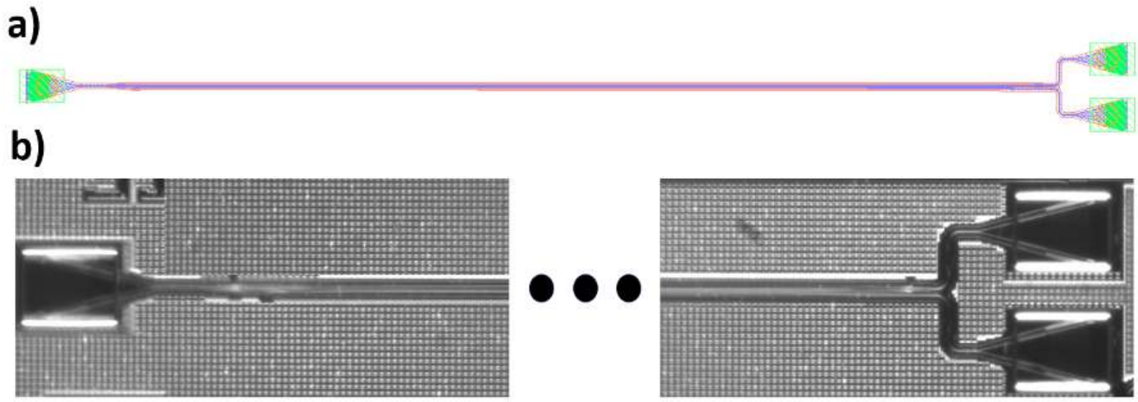

Figure 2.8: a) Layout of a single segment filter with grating coupler connections. b) Optical microscope image of input and output of one of the fabricated single segment filters.

Figure 2.9 shows the measurement results of single-stage filters with limit wavelengths $\lambda_c = 1580$ nm at the top and $\lambda_c = 1590$ nm at the bottom. As seen in these figures, these filters have a bandwidth of over 120nm with the output loss under 2.5 dB. The roll-off speed of over 1.5 dB/nm and a extinction of 12 dB was achieved. As can be seen in the figures, there are shifts of up to 7 nm in the cut-off wavelengths of these filters. We think that these shifts are due to process variations that occurred during fabrication.

2.8 Band-pass filters

One of the most significant advantages of these single-stage adiabatic filters is that they can be individually designed and cascaded, in order to achieve arbitrary fil-

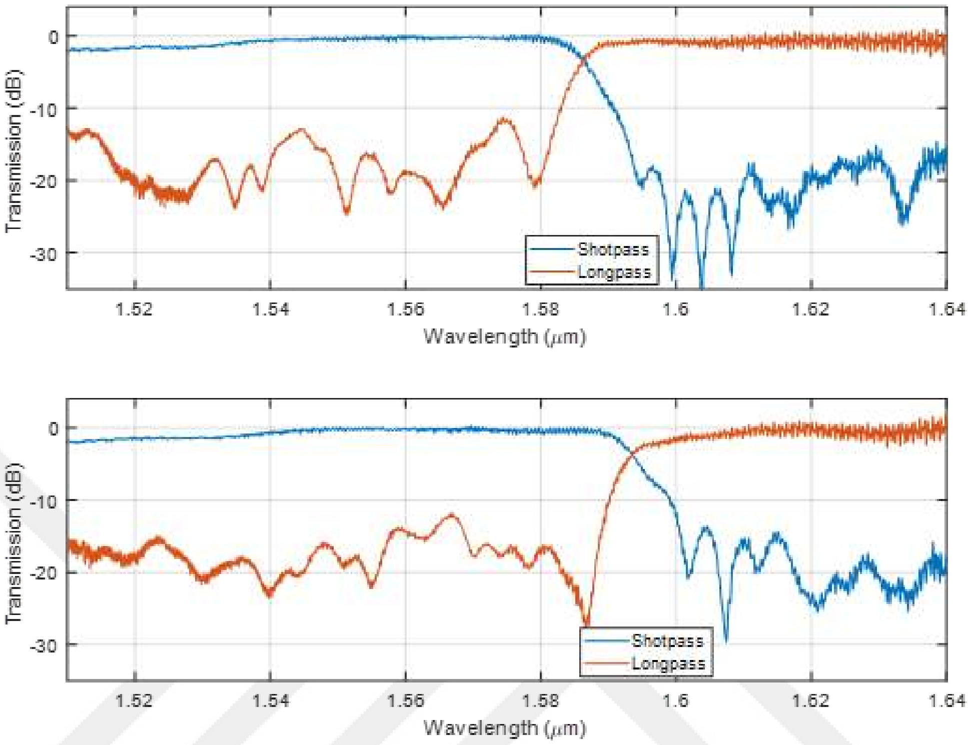

Figure 2.9: Measurements of single segment filters with cut-off wavelengths of 1580 nm (top) and 1590 nm (bottom).

tering profiles in any one of long-pass, short-pass, or band-pass configurations. We demonstrate this by cascading two of these single-stage filters as shown in Figure 2.10a to obtain a double-stage, band-pass filter. Here, the individual cutoff wavelengths are denoted by λ_{c1} and λ_{c2}, where $\lambda_{c1} < \lambda_{c2}$. The long-pass output from the first filter is connected to the input of the second filter. Therefore, the short-pass output from the second filter exhibits a band-pass response. We designed each one of these filters by modifying the dimensions of the individual waveguides (specifically w_T), in order to place the band edges at the desired cutoff wavelengths. Considering the previously mentioned design tradeoffs, we chose $\epsilon \approx 0.0015$ and λ_d to be 10 nm shorter than the cutoff wavelength to obtain the best possible extinction and roll-off, while limiting total device length of each individual filter to around 1 mm. Specifically, we designed four double-stage filters with target bandwidths of 5 nm, 20 nm, 50 nm, and 100 nm, each one consisting of two cascaded single-stage filters. We then ran the above algorithm for sections 2 and 3 of each one of these eight single-stage filters. The resulting total device lengths of these independently designed single-stage filters are between 766.8 µm and 1126.4 µm.

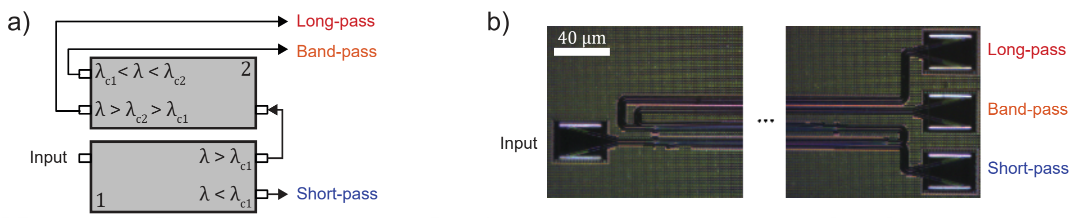

Figure 2.10: Block diagram of a double-stage filter composed of two cascaded filters with cutoff wavelengths of λ_{c1} and λ_{c2}. (b) Optical microscopy images taken from the input and output sections of a double-stage filter.

The cascaded structures were fabricated using standard 193 nm CMOS photolithography techniques on 220 nm SOI wafers through imec's multi-project-wafer foundry service. An optical microscopy image from the two ends of one of the fabricated band-pass filters is shown in Figure 2.10b Edge couplers (for devices with 50 nm and 100 nm target bandwidths) and grating couplers (for devices with 5 nm and 20 nm target bandwidths) provided by the foundry were used for coupling light into and out of the devices. The fabricated filters were then characterized using a tunable laser source and an optical power meter. A manual 3-paddle polarization controller was used to couple TE light onto the chip. In Figure 2.11a, we plot the experimentally measured transmissions at the three output ports of the double-stage filter with 100 nm target bandwidth. For this filter, we cascaded two single-stage filters with target cutoff wavelengths of λ_{c1}=1525 nm and λ_{c2}=1625 nm. Resulting cutoff wavelengths were measured to be λ_{c1}=1534.6 nm and λ_{c2}=1631.2 nm. Therefore, this specific filter demonstrates a bandwidth of 96.6 nm at the band-pass output. As predicted by the individual filter simulations of the independent stages, all outputs are spectrally flat across the whole measured spectrum with insertion loss of less than 1.5 dB in all three outputs. The roll-off speeds were measured to be 1.40 dB/nm and 1.55 dB/nm at the two cutoff wavelengths respectively, matching our expectations from the transfer matrix simulations. The extinction ratios were measured to be 14.5 dB, 15.2 dB, and 11.0 dB for the short-pass, band-pass, and long-pass outputs, respectively.

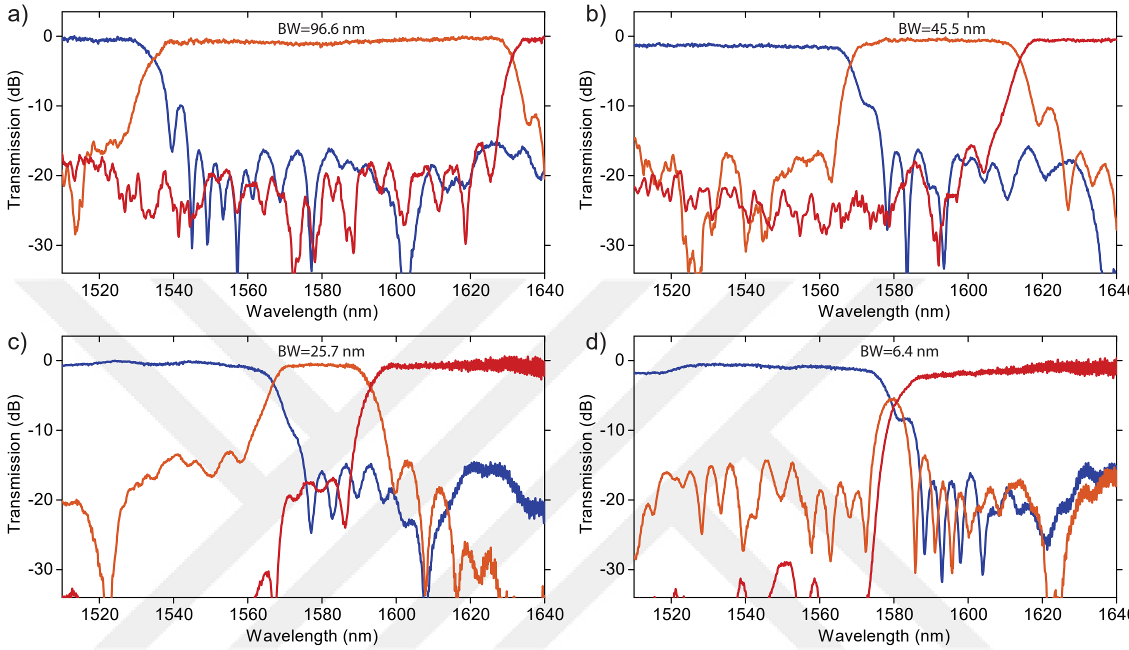

Figure 2.11: Measured transmission spectra of the double-stage filters with bandwidths of (a) 96.6 nm, (b) 45.5 nm, (c) 25.7 nm, (d) 6.4 nm. Blue, orange, and red lines represent short-pass, band-pass, and long-pass outputs, respectively.

While these extinction ratios are less than those predicted by transfer matrix simulations in Figure 2.6, the difference can be attributed to excitation of higher order modes that are present in our waveguide cross-sections and fabrication imperfections. In theory, what ultimately determines the resulting extinction ratio are two key parameters: γ as a function of wavelength at the end of the device, and how much power (ϵ) is lost from the fundamental mode by the end of the device. Of these parameters, γ is determined by final waveguide cross-section itself, and ϵ is specified directly as an input to the optimization algorithm. Therefore, the gradual evolution of waveguide geometry has no direct influence on the extinction ratio, given that this evolution is formed in a way that power lost from the fundamental mode is below a sufficiently small ϵ and the final cross-section of the structure achieves a sufficiently large γ. However, in our adiabatic design, we limit the analysis to coupling only between fundamental even and odd modes. Power lost to higher order modes may contribute to the power recorded at the other outputs. A more general optimization approach that accounts for coupling loss to all other guided and radiative modes [Siriani and Tambasco, 2021] can be used for further improvement of the extinction ratios, depending on specific application requirements. As a generalized version of our two-mode-approach here, look-up tables of coupling coefficients with overlap integrals of all pairs of possible modes can be created. Using this data, the adiabatic transitions can be numerically optimized by limiting the amount of power lost to all of the other modes included in this analysis. By limiting the total optical power coupled out of the fundamental mode, such an approach may result in devices with better extinction ratios than those considering only two modes. Besides the higher order mode coupling, fabrication variations may also contribute to the mismatch of extinction ratios between simulations and experimental measurements. We investigated the effect of potential over-etch under-etch scenarios, and observed deterioration in extinction ratios of about 5 dB, with ±15nm over/under-etch of waveguide widths. In addition to extinction ratio, we also find that the cutoff wavelength deviations of about 10-12 nm from simulation results can be attributed to uneven changes in the widths of WG_1 and WG_5, again by about 15nm over/under-etch of waveguide widths.

Measured transmissions of the filters with target bandwidths of 50 nm, 20 nm, and 5 nm are shown in 2.11 b, c, and d, respectively. Resulting 3 dB-bandwidths for each one of the filters were 45.5 nm, 25.7 nm, 6.4 nm, respectively. The extinction ratios were again measured to be at least 14.0 dB in the passband; and the insertion losses were measured to be less than 1.5 dB. Except for the narrowest band filter in 2.11 d, all outputs were observed to be spectrally flat. For the device with the bandwidth of 6.4 nm, since the cutoffs of individual filters are spectrally close, resulting double-stage filter can exhibit higher insertion loss due to the filter roll-off. Depending on the application requirements, this can be mitigated by improving filter roll-off through optimal ϵ and λ_d selections as necessary, at the expense of longer device lengths. These results demonstrate the flexibility of our design algorithm in creating spectral filters with bandwidths from several nanometers to about 100 nm and beyond, enabling their use in a wide variety of applications. These band-pass adiabatic filters present an important class of devices enabling FSR-free, ultra-wide passbands with a flexible design procedure, while still providing access to all three outputs in transmission mode for any downstream devices. Crucially, this eliminates the need for the use of a circulator that is required for accessing outputs from devices in reflection mode [Cheng and Chrostowski, 2020, Chen et al., 2013]. Moreover, this new class of filters come with a flexible and scalable design methodology that can be adapted for a variety of applications that require broadband and flat-top transmission responses. Ring resonators are the most compact filters among conventional integrated filters, but the widest achievable bandwidths are on the order of several nanometers, even with high-order or cascaded ring schemes due to limited FSRs and underlying resonant dynamics [Chen et al., 2014]. In the interference-based AWG and MZI lattice filters [Xu and Shi, 2017, Pathak et al., 2014], FSRs determined by the interference order impose an upper bound on the practically usable filter bandwidth, typically up to around 20 nm. Therefore, even though these filters achieve relatively higher extinction, they are significantly limited in terms of bandwidth. These AWG or MZI-based filters typically also require large device footprints on-chip, reducing integration density. With the use of SWGs, the passband bandwidths in grating-based MZI filters have been extended to about 40 nm by increasing the coupling coefficient [Sumi et al., 2018]. However, fabrication of such SWGs can be significantly challenging due to small feature sizes, especially when trying to increase the coupling coefficient beyond what is possible with standard SOI processing capabilities [Luque-González et al., 2021]. Prior to our devices here, the widest demonstrated bandwidths have been achieved with contra-directional Bragg couplers, but with much longer device sizes and limited extinction ratios [Hammood et al., 2021]. In these gratings, while a slower chirp rate can improve the extinction in principle, it also greatly increases the device length. In contrast, our waveguide structure does not rely on the coupling between backward and forward propagating modes. This fundamental difference in the underlying filtering approach enables our designs to achieve much wider filter bandwidths than those limited by the strength of grating perturbations. The waveguide geometry we present requires no additional material deposition or fabrication stages that are otherwise used to further increase the coupling coefficient [Vermeulen et al., 2010]. Moreover, it is also possible to create passbands wider than 100 nm or even more complicated spectral filter shapes using the design procedure we outlined, through flexible and independent design and cascading of the individual stages. Our filters can be especially useful in applications that require transmission responses wider than typical 100 GHz - 1 THz passbands (0.8nm - 8nm around 1550nm), for which ring resonators or MZIs may be typically sufficient. For instance, ultra-broadband integrated optical (de)multiplexers are essential for scaling the transmission capacity of fiber optic networks. So far, AWGs are commonly used for designing high-density multiplexers utilizing a broad spectrum around the C-band [Dai and Bowers, 2014, Dai, 2017, Akca and Doerr, 2018, Chen et al., 2015]. Pinguet et al. have demonstrated wavelength division multiplexer transmission with four channels and with a crosstalk level of -17 dB [Pinguet et al., 2008]. Interleaved AWGs [Akca and Doerr, 2018] and MZI-assisted AWG [Chen et al., 2015] are also demonstrated as multiplexers with -15 dB of crosstalk in operation, but they suffer from high insertion losses of up to 10 dB. Therefore, owing to its low-loss, flat-top, and broadband operation with superior performance metrics, our filters with double-stage or multi-stage configurations can be utilized in integrated ultra-wideband transmission systems covering the S-, C-, and L- bands. Similarly, the operation bandwidth of spectrometers can be significantly increased by combining multiple bands with our filters. Moreover, in dual-comb spectroscopy applications, spectrally filtering a broadband light source is routinely used to improve the signal-to-noise ratio [Newbury et al., 2010]. Currently, many systems use free-space optical filters to separate the two halves of the dual-comb spectrum [Dutt et al., 2018, Yu et al., 2018]. In these applications, our filters can be a scalable on-chip alternative to bulky free-space components, helping reduce system complexity and improve integration density.

2.9 Coarse Wavelength Division Multiplexers

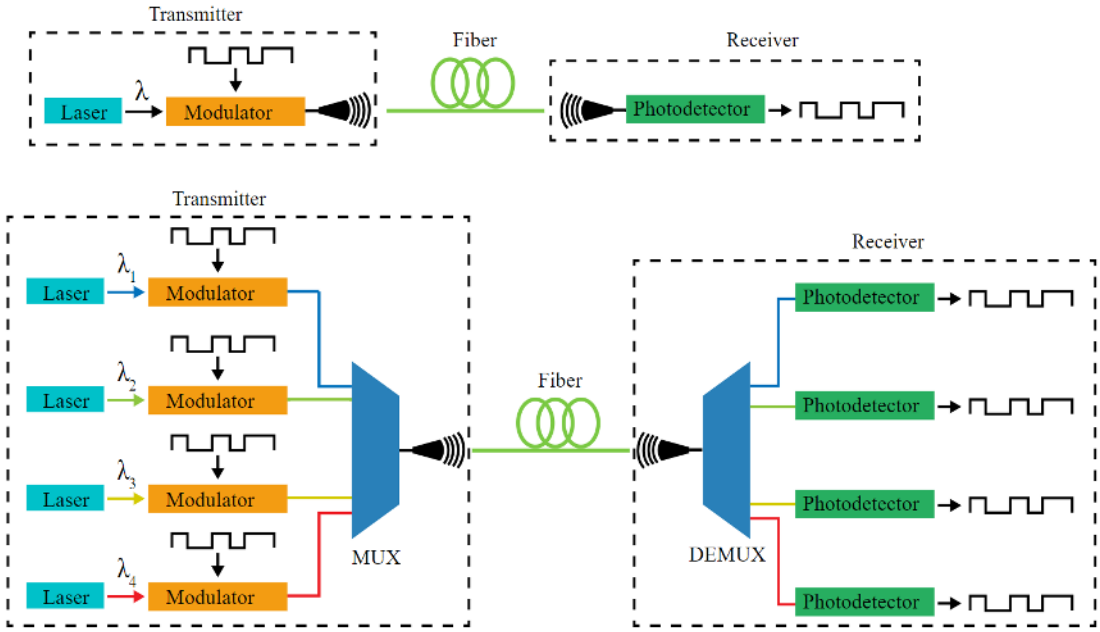

Figure 2.12: Illustrations of single and multi-channel optical communication links at the top and bottom, respectively

Wavelength division multiplexing (WDM) holds significant importance in communication applications due to its ability to enhance the capacity and efficiency of optical fiber networks. Figure 2.12 shows the illustrations of single and multi-channel optical communication links at the top and bottom, respectively. Multi-channel communication link utilizes multiplexer (MUX) and de-multiplexer (DEMUX) at the transmitter and receiver sides, respectively, enabling the aggregation of multiple bands together. By dividing the available bandwidth into multiple channels and assigning each channel a different wavelength, WDM enables simultaneous transmission of multiple data streams over a single optical fiber. This technique significantly increases the capacity of the communication system, allowing for the seamless integration of high-speed data, voice, and video traffic. WDM enables efficient utilization of the limited resources of optical fibers, reducing the need for additional infrastructure investments. It also offers flexibility in network design, allowing for

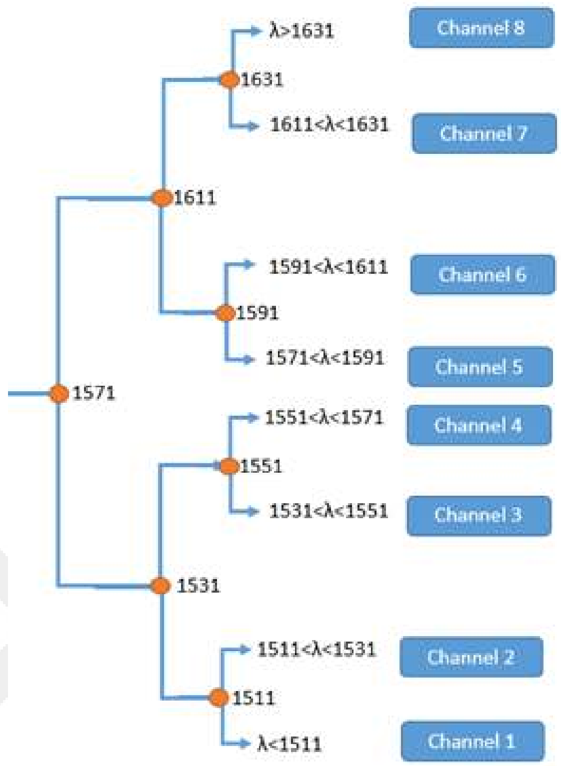

Figure 2.13: Coarse WDM connection diagram.

scalability and future expansion. With the exponential growth of data traffic and the demand for higher bandwidth, WDM has become a crucial technology in modern communication applications, providing cost-effective and efficient solutions to meet the ever-increasing data transmission requirements.

Since outputs of the adiabatic filters operate in transmission, it is possible to cascade multiple filters in different configurations. Taking advantage of this flexibility, we cascade 7 filters with different cutoff wavelengths on-chip with a tree-like configuration as shown in Figure 2.13 to obtain a coarse WDM. In this figure, each orange circle represents a single-stage filter.

With this connection configuration, we created the layout of coarse WDM by folding and cascading 7 single-segment filters. Layout of the device is shown in Figure 2.14. This device has single input and 8 outputs covers a footpirint of 200 μm x 900 μm in size. Figure 2.15 shows the measurement results of the outputs of the

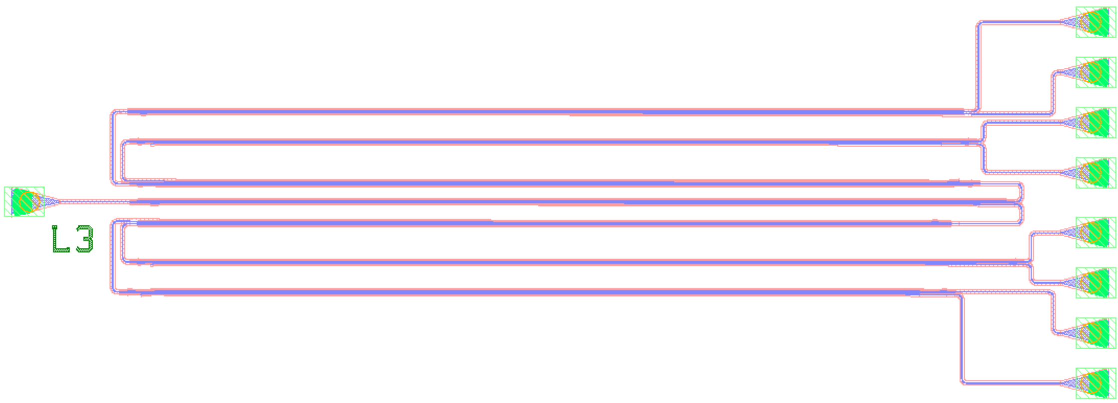

Figure 2.14: Coarse WDM connection diagram.

multi-channel filter. Due to the shifts in the cut-off wavelengths due to fabrication variations, the bandwidths of some outputs are measured slightly wider or narrower than designed. The extinction at the center of all the band-pass type channels of this 8-channel multiplexing is over 12 dB.

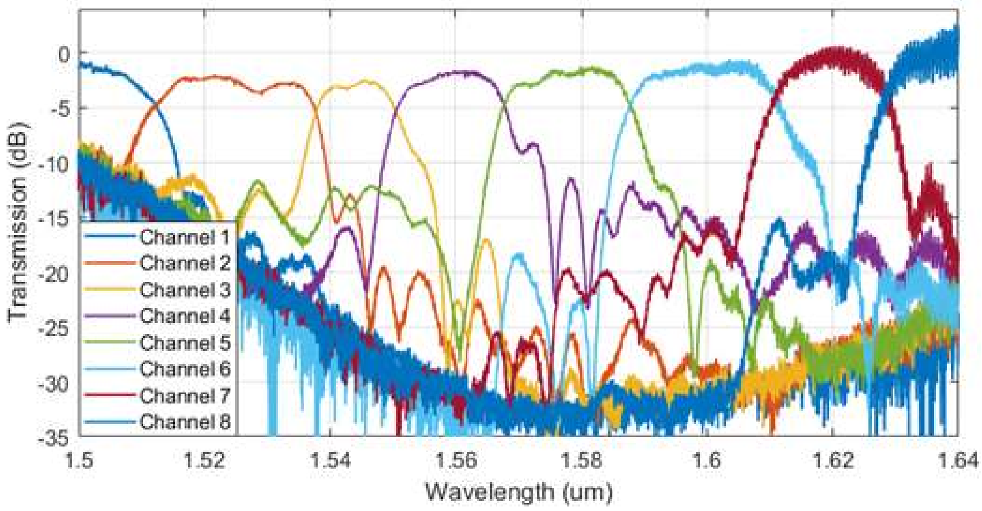

Figure 2.15: Measured transmission results of 8-channel coarse WDM.

2.10 Effect of Design Wavelength (λ_d) on Adiabatic Filter Design

For a given wavelength, which we call the design wavelength (λ_d), Eq. 2.18 can be solved and γ(z) can be obtained. However, since γ changes with wavelength, solution of Eq. 2.18 at different λ_d will result in a different γ(z). In order to analyze how the choice of λ_d affects the adiabatic transitions, we fixed the ϵ bound at 0.005, and calculated w(z) and s(z) for different λ_d. We used a five-segment waveguide consisting of 250 nm wide subwavelength layers separated with 150 nm gaps. We chose the target width of single-segment waveguide as 308 nm resulting in a cutoff wavelength (λ_c) of 1546 nm. For convenience, we defined a new parameter, $\Delta\lambda = \lambda_c$-$\lambda_d$, as the difference between the cutoff wavelength and the design wavelength. In Figure 2.16a and Figure 2.16b, we plot the calculated w(z) (for section 2) and s(z) (for section 3), for three different choices of $\Delta\lambda$ ranging from 6 nm to 26 nm. From these results, we conclude that as $\Delta\lambda$ decreases (i.e., λ_d approaches λ_c), transition length decreases for the width, w(z), but significantly increases for the separation, s(z). To better understand this behavior, we rearranged Eq. 2.18 as

$$\frac{d\gamma}{dz} \leq 2\kappa(1+(\delta/\kappa)^2)^{3/2}\sqrt{\epsilon} \tag{2.19}$$

and plotted the right-hand-side (RHS) of Eq. 2 in Figure 2.16c as a function of WG_1's width w(z) in section 2. This RHS serves as an upper bound for dγ/dz, and is shown again for the three different choices of $\Delta\lambda$. From this analysis, we note that as the width of WG_1 increases, max(dγ/dz) decreases to a minimum and then increases again. That is because with a wider WG_1, the phase mismatch between the waveguides decreases at the beginning and becomes zero at the width where two waveguides are phase-matched at corresponding $\Delta\lambda$. Here, the width for WG_1 at which the two waveguides are phase-matched is a function of the design wavelength, and therefore is also a function of $\Delta\lambda$.

When WG_1's width is greater than the phase matching width, there is greater phase mismatch; and thus max(dγ/dz) increases again. Therefore, the transition becomes much slower as the width of WG_1 approaches the point where two waveguides

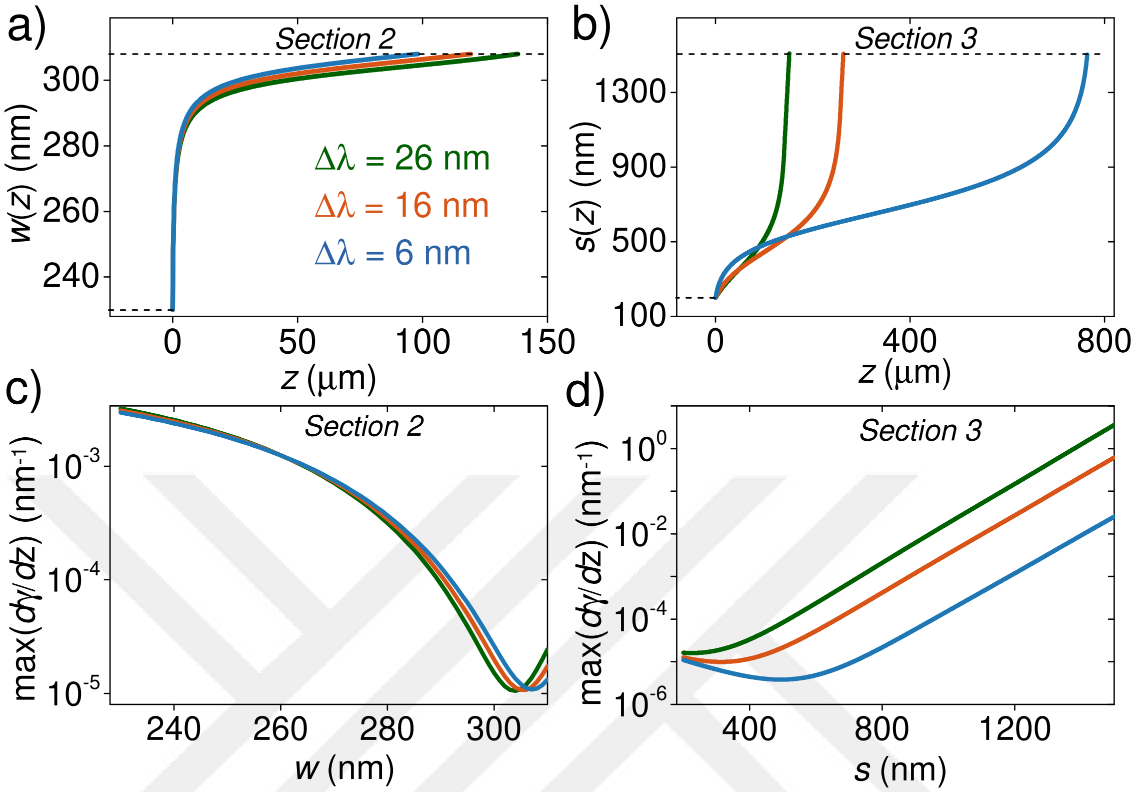

Figure 2.16: Calculated (a) w(z) and (b) s(z) for three different $\Delta\lambda$. Calculated RHS of Eq. 2 as a function of (c) w and (d) s. ($\Delta\lambda$ = λ_c-λ_d)

are phase-matched. Comparing different $\Delta\lambda$, we find that max(dγ/dz) is greater for smaller $\Delta\lambda$ at a majority of the width range up to 308 nm (260 nm - 305 nm), which enables shorter transitions for smaller $\Delta\lambda$. This can be explained again by phase-mismatch between the two waveguides. For the widths between 260 nm and 305 nm, with longer design wavelengths (i.e. smaller $\Delta\lambda$) the phase mismatch between the waveguides grows, resulting in a higher max(dγ/dz). For example, at a width of 300 nm, the phase-matching wavelength is around 1500 nm. Therefore, at this width, phase mismatch between waveguides is the greatest for $\Delta\lambda = 6$ nm ($\lambda_d =$ 1540 nm) resulting in the highest max(dγ/dz), and is the smallest for $\Delta\lambda = 26$ nm ($\lambda_d = 1520$ nm) resulting in the lowest max(dγ/dz).

For the same three $\Delta\lambda$, we plot the maximum bound on dγ/dz in Figure 2.16d, this time as for section 3 as a function of the separation s(z) between WG_1 and

WG_5. Here, the coupling coefficient decreases with increasing separation. Hence, max(dγ/dz) increases with decreasing κ, making the transitions faster as separation increases. Comparing different $\Delta\lambda$, we find that as $\Delta\lambda$ decreases, max(dγ/dz) is significantly suppressed due to the two waveguides becoming more closely phase-matched. This drop in max(dγ/dz) results in much longer transitions, in order to maintain the same amount of maximum power (ϵ) coupled to the adjacent waveguide, at design wavelengths much closer to the cutoff wavelength.

Using the transfer matrix method, we simulated the structures obtained from the results in Figure 2.16. First, we plot the fraction of power in the fundamental even and odd modes in Figure 2.17a. This power is calculated at the end of the filter designed with the three different $\Delta\lambda$. With smaller $\Delta\lambda$, while the power in the odd mode remains constant at the cutoff wavelength λ_c itself, it is significantly reduced on either side the cutoff. This is evident from the faster spectral roll-off of the odd mode power on either side of the cutoff wavelength. This behavior is expected as the adiabatic criterion ensures that the amount of power lost to the odd mode is kept at a minimum at the design wavelength λ_d. Therefore, choosing a design wavelength closer to the cutoff wavelength suppresses the power in the odd mode around the cutoff.

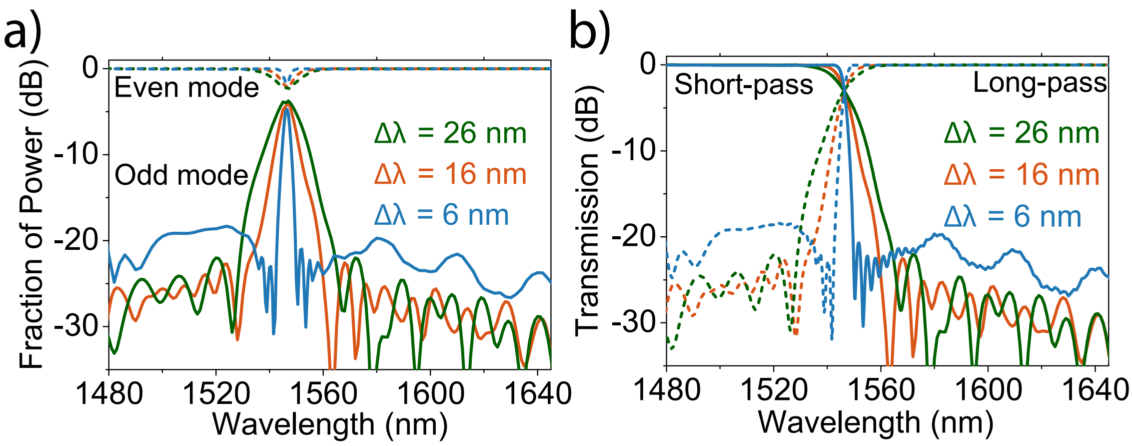

Figure 2.17: Simulated fraction of power in fundamental even and odd modes at three different $\Delta\lambda$. (b) Simulated transmission spectra of the single-stage filters designed at three different $\Delta\lambda$.

Figure 2.17b shows the transmission spectra of these filters. We observe that as $\Delta\lambda$ decreases, the filter roll-off becomes sharper, at the expense of longer overall device lengths. These sharper roll-offs can be beneficial for spectral separation in many applications. However, we also note that using a smaller $\Delta\lambda$ also decreases the extinction ratio of the filter. This can be explained by the design algorithm's tendency to strongly favor the spectral separation and a sharp filter roll-off when using a smaller $\Delta\lambda$ choice. This problem can be prevented by a more general adiabatic design process where multiple design wavelengths are used, and the device optimization procedure limits higher mode excitation at each one of these wavelengths.

2.11 Effect of Width Deviation on the Filter Response

In this section, we investigated the effect of fabrication variations on the filter performance. We chose a filter with a cutoff wavelength (λ_c) of 1546 nm as our reference structure, which has a five-segment waveguide consisting of 250 nm wide subwavelength segments separated by 150 nm gaps, and a single-segment waveguide with 308 nm target width. We calculated the optimized adiabatic transitions of section 2 -w(z)- and 3 -s(z)- by setting λ_d as 1530 nm and ϵ as 0.005. Then we performed the transfer matrix simulations of the same structure under various over-etch and under-etch amounts. Here, we consistently increased (decreased) the width of each subwavelength segment of the five-segment waveguide and width of the single-segment waveguide by certain under-etch (over-etch) scenarios, indicated below by the variable Δw. The center-to-center separation of the waveguide segments remained unchanged in this analysis. Figure 2.18 shows the simulated transmission spectra at long-pass outputs in (a) under-etch (Δw>0) and (b) over-etch (Δw<0) cases. In this case, since both five-segment and single-segment waveguides are subject to the same amount of etch offsets, the phase matching wavelength of WG_1 and WG_1 only changes slightly. For instance, for 10 nm of under-etch and over-etch cases, cutoff wavelength shifts from the ideal device are observed to be less than 1 nm and around 2 nm, respectively. A blue-shift of cutoff is observed in both under-etch and over-etch scenarios, which can be explained by the effective index of WG_5 being greater than that of WG_1 both when Δw>0 and Δw<0, resulting in phase matching of the two waveguides at a shorter wavelength. In addition to the slight change in the cutoff wavelength, we also observe that these width variations worsen the extinction ratio by about 5 dB. This degradation is a direct result of the violation of the adiabaticity condition in Eq. 1 due to the modified profile of $\gamma(z)$, resulting from the changes in the propagation constants of WG_1 and WG_5 when Δw $\neq 0$.

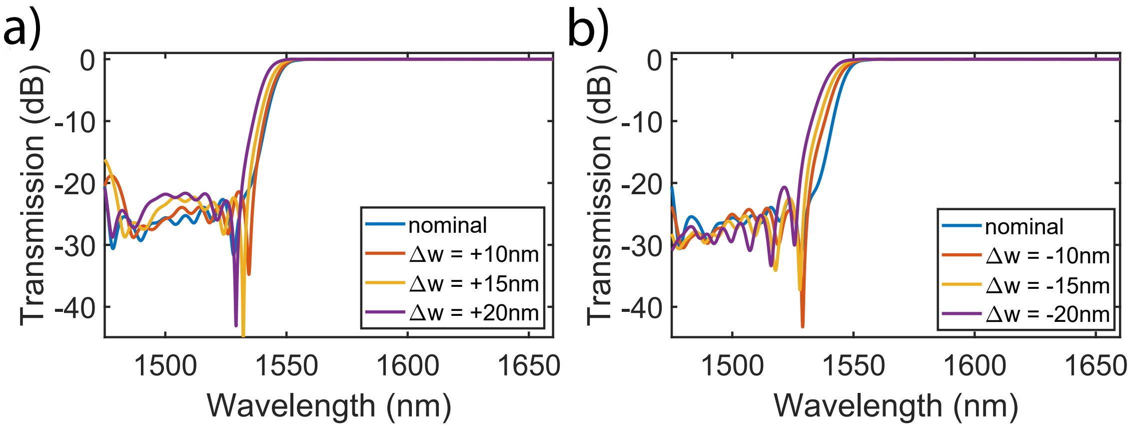

Figure 2.18: Simulated long-pass transmission spectra of the filter in (a) under-etch and (b) over-etch cases. Widths of both WG_1 and WG_5 are modified by the same amount, indicated by Δw.

In our experimental measurements, we observed a redshift of cutoff wavelength by about 10 nm. In order to model this, we investigated several scenarios where WG_1 and WG_1 are subject to different etch offsets (specifically where $\Delta w_{(WG1)} > \Delta w_{(WG5)}$. Such uneven etch offsets of the two waveguides more strongly influences the phase matching wavelengths of the two waveguides. As shown in Figure 2.18, an increasing difference between $\Delta w_{(WG1)}$ and $\Delta w_{(WG5)}$ results in a worse measured extinction ratio and emerging sidelobes in the transmission spectrum, similar to the spectral features we measured experimentally in our double-stage filters.

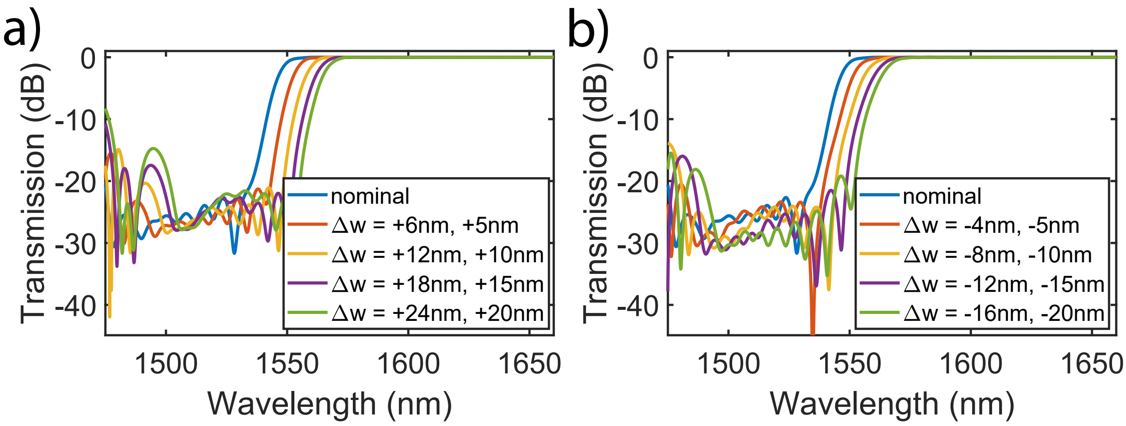

Figure 2.19: Simulated long-pass transmission spectra of the filter in (a) under-etch and (b) over-etch cases. Widths of WG_1 and WG_5 are modified by different amounts. In the legends, the first and second values represent width deviations for WG_1 and WG_5, respectively.

2.12 Effect of Roll-off on Bandwidth

The flexibility of designing individual spectral filters allows building more complicated transfer functions using multiple different single-stage devices in combination. For bandpass devices, two of these single-stage filters with appropriate cutoff wavelengths can be cascaded in series. Figure 2.20 shows the passband configurations of cascaded filters for two different cases, depending on the spectral separation of the cutoff wavelengths of single stage filters (λ_{c1} and λ_{c2}). In Figure 2.20a, we indicate that if the cutoff wavelengths of the two single stage filters are sufficiently different, then a flat and inherently lossless passband can be obtained in the bandpass output. Bandwidth of this cascaded filter is then simply calculated as the difference between the cutoffs, namely λ_{c2} - λ_{c1}. However, if the cutoff wavelengths of individual filters are chosen to be spectrally close as shown in Figure 2.20b, the bandpass output of the resulting double-stage filter experiences some insertion loss. We denote the individual filter roll-offs with α (dB/nm) and their spectral intersection with a transmission of -χ (dB). The design procedure we outlined provides flexibility in the roll-off speed α through the choice of the design wavelength with respect to the cutoff wavelength. Given α, then the transmission -χ at the spectral intersection of the two filters is simply a function of how their cutoff wavelengths are positioned spectrally. With these parameters, the overall device exhibits an insertion loss of 2χ dB, and a 3dB-bandwidth of $(2\chi+6)/\alpha$ nm, respectively. It is possible to eliminate insertion loss completely, by careful selection of the cutoff wavelengths to be sufficiently far from one another. In that case, bandwidth is only limited by the roll-off speed (if χ=0, then BW=6/α nm). Therefore, in order to achieve narrowband filters, single-stage filters with sharper roll-offs (higher α) are required. As an example, if the roll-off speed is 1dB/nm for both single stage filters, then the narrowest achievable 3 dB-bandwidth for the band-pass filter is 6 nm. This estimate can be used as a starting point for filter design using the approach we outline. For a more detailed analysis of the filter transfer function and filter bandwidth, the transfer matrix method described in the manuscript yields more accurate results since the filter roll-offs are not perfectly linear in the spectral domain, and the two filters can exhibit slightly different roll-offs than each other.

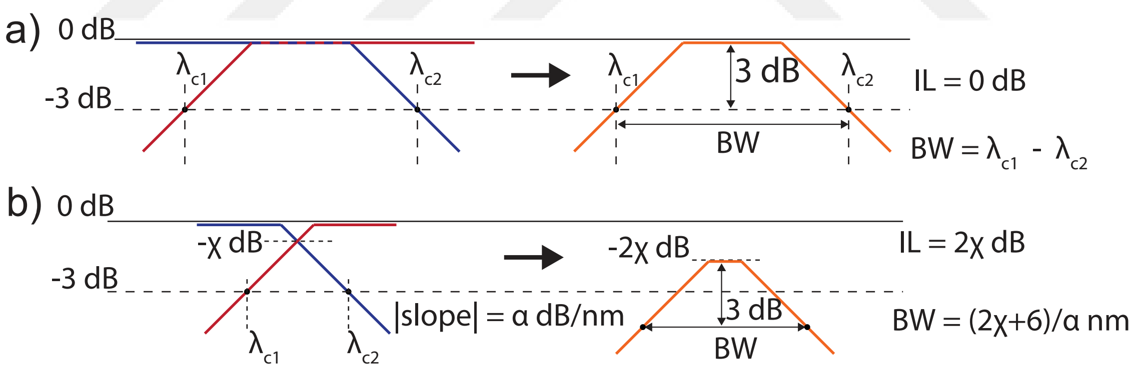

Figure 2.20: Passband configurations of cascaded filters for (a) λ_{c1} and λ_{c2} are spectrally distant, (b) λ_{c1} and λ_{c2} are spectrally close. (IL: insertion loss, BW: 3dB-bandwidth)

2.13 Conclusion

In summary, we presented the design of compact integrated spectral filters with ultra-broadband response and low insertion loss through a flexible adiabatic optimization algorithm. We showed that the proposed filters' roll-off and extinction performance can be optimized by modifying the optimization bound on the power lost to unwanted mode in separately designed filter stages. The ability to independently configure band edges through our design algorithm provides the previously elusive design flexibility for filters with different bandwidths. This flexibility also enables other multi-stage filter configurations for implementing more complicated spectral features. Experimentally, we demonstrated band-pass filters composed of two cascaded single-stage filters. Our band-pass filters experimentally achieve bandwidths up to 96.6 nm with flat-top transmissions, a maximum insertion loss of 1.5 dB, and an extinction ratio of over 15 dB in the passband. With the widest bandwidths reported to date, these devices can enable new possibilities in next-generation, high-throughput, and ultra-broadband communications and spectroscopy applications.

Chapter 3

ON-CHIP ARBITRARY DISPERSION ENGINEERING WITH DEEP PHOTONIC NETWORKS

We demonstrate design and optimization of on-chip arbitrary dispersion profiles by using deep photonic networks with custom designed Mach-Zehnder interferometers. The photonic networks employ optimizable waveguide tapers allowing for engineering of wavelength-dependent dispersion profiles. As a proof of principle, we design and demonstrate a photonic network with a triangular dispersion profile optimized over a 40 nm spectrum with a flat transmission of less than 0.7 dB insertion loss.

3.1 Introduction

Efficient management of dispersion is crucial for many applications such as high-speed optical communication and optical signal processing [Eggleton, 2001, Neilson, 2004, Neilson et al., 2004, Goda and Jalali, 2013, Dolgaleva et al., 2011, Mokhtari et al., 2013]. Several methods have been used for on-chip control of dispersion including micro-ring resonators [Liu et al., 2022c], photonic crystals [Vlasov et al., 2005], arrayed waveguide gratings [Wang et al., 2020], and Bragg gratings [Wang et al., 2018, Liu et al., 2023, Sahin et al., 2017]. Most of these studies aimed at achieving a constant dispersion within a band for cancellation of undesired dispersion in communication systems. On the other hand, dispersion management with a large number of optimizable parameters is highly desired for pulse shaping [Weiner, 2011] and dispersion-based quantum applications [Mower et al., 2013]. Early demonstrations of pulse shaping are done with free space diffraction gratings and spatial light modulators, where light is spectrally split into different components, then modulated and combined back [Weiner, 2011]. Later, chip-scale implementation of pulse shaping with cascaded tunable ring resonators is reported for arbitrary radiofrequency waveform generation [Khan et al., 2010]. Dispersion control is also important in quantum information processing applications such as high dimensional quantum key distribution [Mower et al., 2013]. Notaros et al. demonstrated a large scale tunable-coupling ring resonator array providing 30 degrees of freedom in dispersion control and proposed a quantum data locking application [Notaros et al., 2017]. The dispersion control capability of cascaded circuits increases with the number of stages or number of optimizable parameters in the circuit [Madsen et al., 1999]. Madsen et al. proposed dispersion optimization with cascaded resonators and showed that as the number of resonators increases, the achieved dispersion becomes closer to the desired value [Madsen and Lenz, 1998]. Therefore, increased degrees of freedom are needed for more complex dispersion profile realizations. In recent years, Mach-Zehnder interferometers (MZIs) based photonic networks have been proposed with very high degrees of design freedom [Zhuang et al., 2015, Bogaerts et al., 2020, Pérez-López et al., 2020]. Several examples including photonic signal processing, image/signal classification, and arbitrarily specified optical responses have been demonstrated with such networks [Harris et al., 2018, Marpaung et al., 2019, Ashtiani et al., 2022, Amiri et al., 2023, Amiri et al., 2022]. However, the potential of photonic networks for arbitrary dispersion realizations is yet to be explored. In this study, we propose on-chip deep photonic networks providing arbitrarily defined dispersion profiles with custom designed MZIs. Each MZI incorporates custom phase delay sections consisting of pair of optimizable waveguide tapers allowing for wavelength-dependent dispersion profiles to be achieved. We created a custom framework for the simulation and optimization of these tapers by rapid transfer matrix evaluations. The framework allows for optimization of the dispersion and transmission simultaneously. With the high degree of design freedom in these tapers, we demonstrated a proof-of-concept device having triangular dispersion over a 40 nm spectrum in C-band. A flat band transmission is achieved in this band with less than 0.7 dB insertion loss. We also showed increasing design of freedom allows for arbitrary transfer function realizations.

3.2 Network architecture and optimization

A two-port integrated photonic network consisting of cascaded Mach-Zehnder interferometer (MZI) units is shown in Figure 3.1a. Each of these MZIs is capable of performing a 2×2 linear transformation indicated by T_i. Figure 3.1b shows one of these MZI units composed of two directional couplers and two pairs of custom tapers for achieving specific phase delays. The directional couplers are designed to be 50/50 splitters at the wavelength of 1550 nm. The custom tapers act as wavelength-dependent phase delay sections, and are composed of custom-designed waveguides. Light in a straight waveguide propagates with a constant dispersion. However, the optical properties of light in a waveguide of custom width vary along the propagation direction depending on the frequency of the light. Hence, the shape of these waveguides can be optimized to obtain a certain optical response. In order to achieve custom spectral phase profiles, and hence custom dispersion profiles, the width of each one of the waveguides in the two arms of the interferometer can be custom-designed using an evolving width in the propagation direction. Here, we represent this continuously changing width w(z) by a set of optimizable widths denoted as control points W[n] = [w1 ... wn].

The operation of directional coupler can be described by the 2×2 matrix

$$C = e^{-j\phi(\lambda)} \begin{bmatrix} t(\lambda) & -j\kappa(\lambda) \\ -j\kappa(\lambda) & t(\lambda) \end{bmatrix} \tag{3.1}$$

where, t and κ are through-coupling and cross-coupling coefficients, respectively, and ϕ is the phase accumulated in the coupler. The wave transfer matrix for each pair of custom tapers is given by

$$P_i = \begin{bmatrix} e^{-j\theta_{(i)1}(\lambda)} & 0 \\ 0 & e^{-j\theta_{(i)2}(\lambda)} \end{bmatrix} \tag{3.2}$$

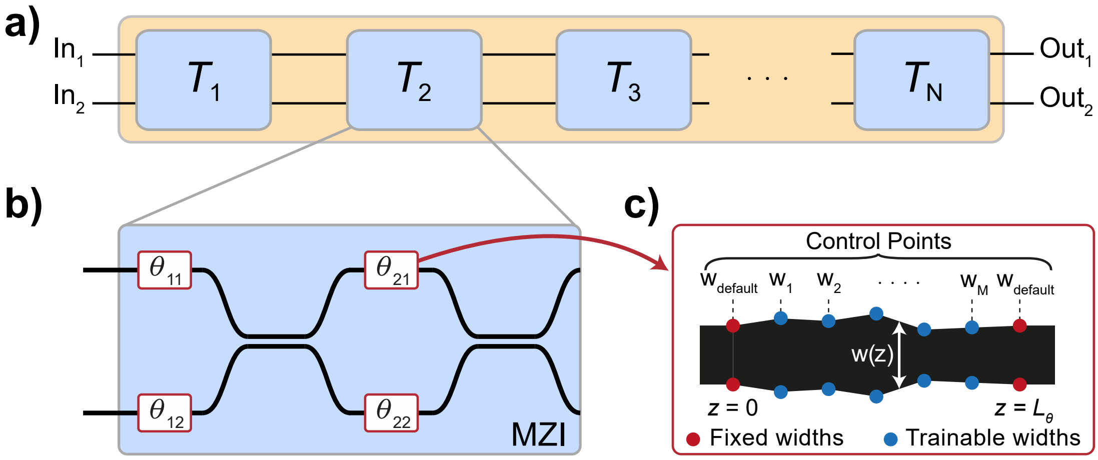

Figure 3.1: a) Photonic network architecture composed of cascaded Mach-Zehnder interferometers (MZIs). b) Single MZI consisting of two splitters, implemented with directional couplers, and two tapers with custom geometries for achieving specific spectral phase profiles. c) Custom waveguide constructed from a set of trainable width parameters.

where $\theta_{(i)1}$ and $\theta_{(i)2}$ are accumulated phases for top and bottom arms, respectively. Accumulated phase in these waveguides is calculated as a function of wavelength as $\theta(\lambda) = \int_0^L \frac{2\pi}{\lambda} n_{eff}(w(z), \lambda), dz$, where n_{eff} is the effective index of the waveguide as a function of wavelength and width, and L is the length of the custom waveguide. Finally, the overall linear transfer matrix of one MZI unit is calculated from the product of the transformation matrices of its two directional couplers and custom phase delay sections as $T = CP_2CP_1$.

$$\begin{aligned} T_i = & e^{-j\phi(\lambda)} \begin{bmatrix} t(\lambda) & -j\kappa(\lambda) \\ -j\kappa(\lambda) & t(\lambda) \end{bmatrix} \begin{bmatrix} e^{-j\theta_{(i)1}(\lambda)} & 0 \\ 0 & e^{-j\theta_{(i)2}(\lambda)} \end{bmatrix} \\ & e^{-j\phi(\lambda)} \begin{bmatrix} t(\lambda) & -j\kappa(\lambda) \\ -j\kappa(\lambda) & t(\lambda) \end{bmatrix} \begin{bmatrix} e^{-j\theta_{(i+1)1}(\lambda)} & 0 \\ 0 & e^{-j\theta_{(i+1)2}(\lambda)} \end{bmatrix} \end{aligned} \tag{3.3}$$

The propagation of the complex optical amplitude through the photonic network is accomplished by employing a computational graph that closely mimics the physical architecture of the network. This computational graph captures the optical transformations carried out by the mesh of interferometers connecting N input channels to

N output channels. Essentially, the graph represents the intricate interconnections and interactions between the optical components. The overall architecture of the computational graph calculates the wavelength-dependent linear scattering matrix, denoted as S(λ), which characterizes the behavior of the deep photonic network [Amiri et al., 2023].

$$S(\lambda) = \prod_{(i)} T_i(\lambda) \tag{3.4}$$

In our designs, while all directional couplers in the MZI network are identical, each phase delay is unique and specifically optimized to provide the desired optical response. The details of this optimization flow for an example photonic network is shown in Figure 3.2. The first step in this optimization procedure is a forward propagation operation which projects the light from input waveguides onto output waveguides. For this operation, t, κ, and ϕ for directional couplers and n_{eff} for custom phase delay sections are fed into the forward propagator. The directional coupler coefficients are extracted from an interpolation of previously run 3D finite difference time-domain simulation result that is readily accessible throughout this process. The effective indices are extracted from a similar set of pre-recorded data from finite difference eigenmode calculations using the Silicon Photonics Toolkit package [Vit et al., 2022]. In order to allow for dispersion calculations with multiple orders of derivatives, all these coefficients are modeled in a way that they are twice continuously differentiable in wavelength. Moreover, the effective indices are also modeled as differentiable functions of width, for gradient based optimization of the waveguide geometry in the custom phase delays. We created a design framework which incorporates these compact models and constructs the network. The key factors contributing to its modularity and high performance are the utilization of open-source deep learning software libraries, namely Jax [Bradbury et al., 2018] and Trax [Tra, 2020]. These libraries offer the capability to perform automatic differentiation-compatible computations on diverse hardware accelerators, such as CPU, GPU, or TPU, in a parallelized manner. This efficiency is achieved through the implementation of just-in-time (JIT) compilation [Aycock, 2003], which optimizes the execution of essential function calls.

Complex amplitude output of the propagator is separated into phase and amplitude components, in order to calculate dispersion $D_c(\lambda)$ and transmission $T_c(\lambda)$ results, respectively. Following this calculation, a loss function L(W) is defined as the difference between calculated network response and target response, summed over spectrum of interest. A weighting parameter, α, is used for balancing loss function in terms of transmission and dispersion. Finally, gradient of L(W) with respect to design parameters (widths) is computed through a back-propagation procedure and used for updating the custom taper widths in each phase delay section. This iterative procedure is repeated until an acceptable loss is achieved.

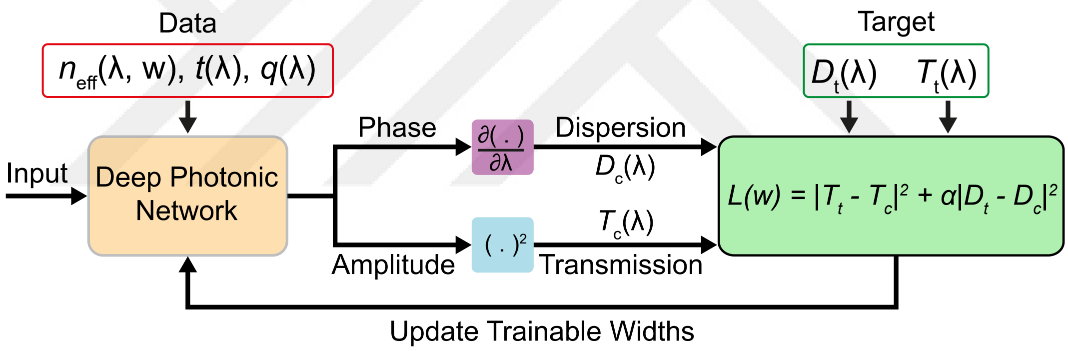

Figure 3.2: Optimization cycle of photonic network.

The proposed network architecture and optimization procedure outlined above allow for design of application-specific photonic networks with arbitrarily-defined, broadband dispersion and transmission profiles. As proof of principle, we demonstrate a photonic network with a target triangular dispersion profile between 1.54 μm and 1.58 μm. With our network structure, the number of MZI layers plays an important role as it is directly related to the degrees of freedom for the specific photonic device being designed, and how easily a target dispersion profile can be achieved. The construction of the photonic network, specifically designed to target a triangular dispersion profile, involves utilizing 12 cascaded MZIs. These MZIs create a total network length of 864 μm. The network's objective is to optimize the response at the top-right port (out_1) for both transmission and dispersion, considering a broadband input applied at the top-left port (in_1).

Each MZI incorporates custom tapers with 5 trainable widths, resulting in a total of 20 trainable widths for each MZI and 240 trainable parameters for the entire network. The initial values of these widths are randomly assigned within the range of 490 nm to 510 nm. Through the optimization process, the widths of all sections are adjusted to find the optimal configuration. The optimized widths, as shown in Figure 3.3, fall between 453 nm and 508 nm, ensuring effective light confinement within the waveguides and maintaining single-mode operation.

For the optimization process, a constant learning rate is utilized. The convergence of the optimization is effectively demonstrated in Figure 3.4, where the loss function, learning rate, and gradient evolution are plotted. The optimization process exhibits stability, with convergence achieved after approximately 4000 iterations, as evident from the loss and gradient plots.

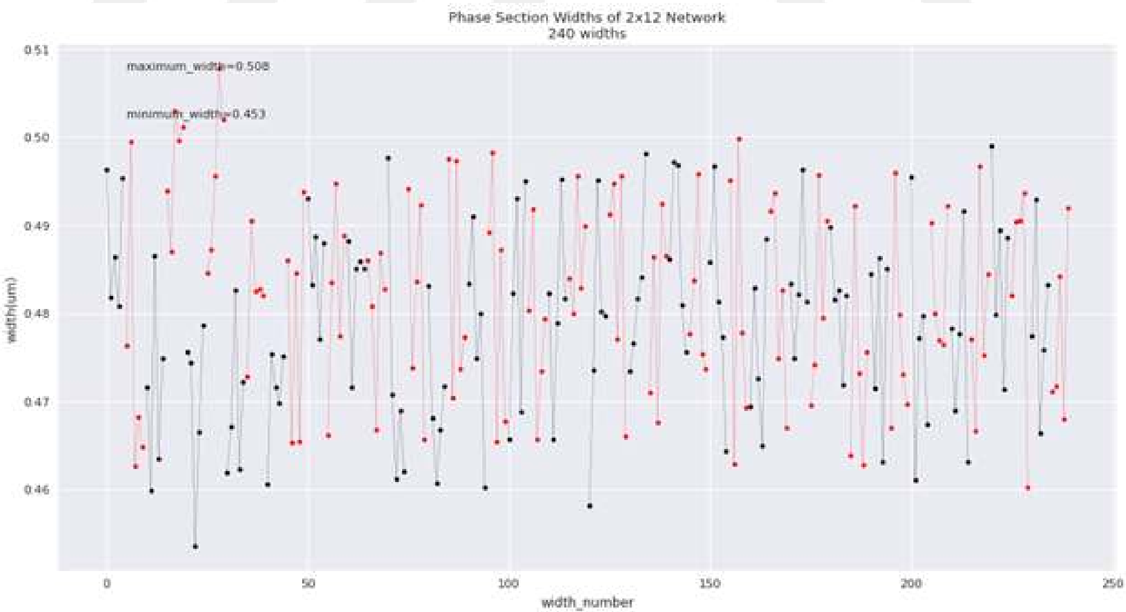

Figure 3.3: Trained widths of dispersion optimized network.

The target and simulated transmission and group delay dispersion results are plotted in Figure 3.5a. The triangular curve shown in green in Fig 2b is the targeted

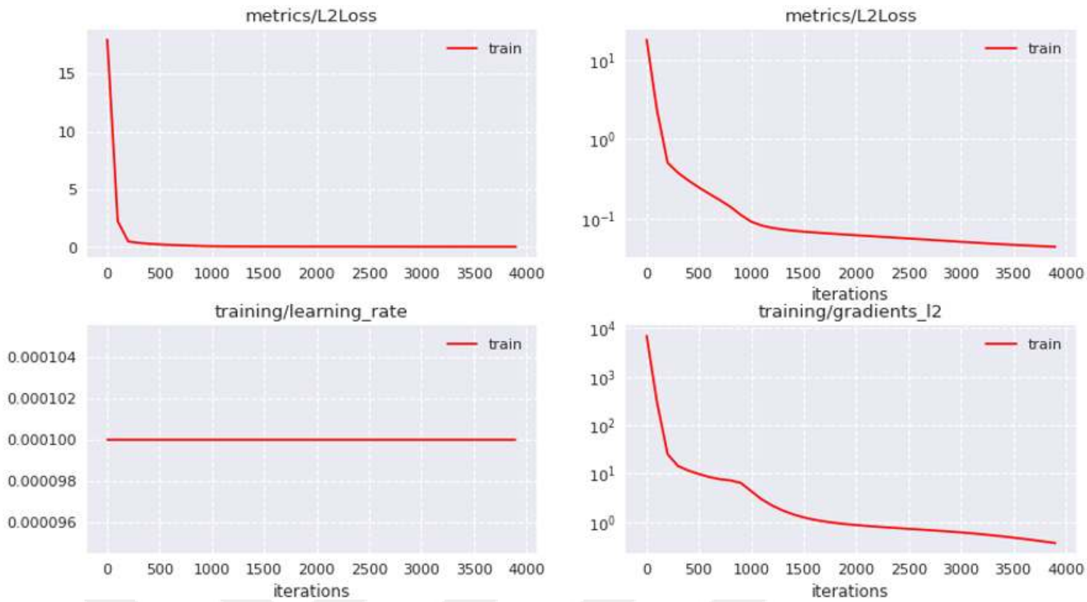

Figure 3.4: Optimization monitor: L2 loss function at the top left (linear scale) and right (log scale) as a function of iteration. Learning rate at the bottom left. Sum of gradients of all parameters at the bottom right.

dispersion profile of the network output. After the optimization of the network is completed, the achieved dispersion profile is plotted in blue. As demonstrated by this result, the network is able to closely achieve the desired dispersion profile, both in spectral features and in amplitude.

In addition to achieving a specific dispersion profile, we also optimize the power output of the device as shown in Figure 3.5b. Here, the target output transmission in port o1 is set to be 1 throughout the entire spectral design range chosen (1.54 μm - 1.58 μm). A full optical transmission objective is included during the optimization process, in order to minimize the output power coupled to the other port (out_2). As shown by the blue curve, the calculated transmission spectrum of the network achieves near lossless transmission response at the desired output port, with simulated amount of loss below 0.16dB.

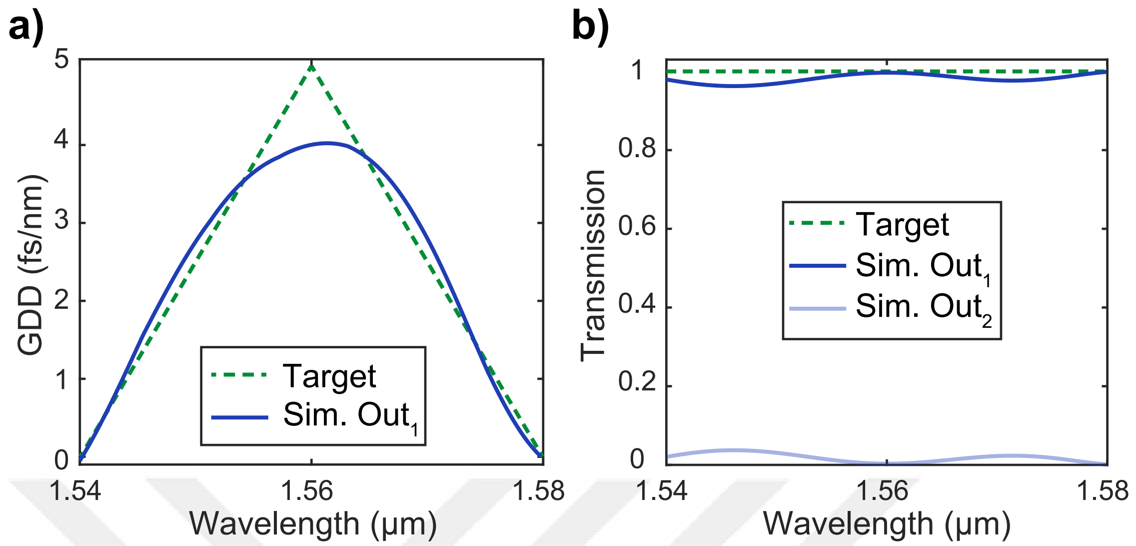

Figure 3.5: a) Target and optimized dispersion profiles for a 2x12 sized network. b) Target and optimized transmittance responses of the same network.

3.3 Experimental results

The photonic network is fabricated using standard 193 nm CMOS photolithography techniques on 220 nm SOI wafers through imec's multi-project-wafer foundry service. Edge couplers provided by the foundry are used for coupling light into and out of the devices. For the characterization of dispersion in this device, an interferometric technique based on observation of interference fringes in transmission spectra was used. Specifically, our device under test was placed in one arm of an integrated interferometer as illustrated in Figure 3.6, in order to measure its group delay dispersion. Transverse electric polarized light was coupled on-chip using a tunable laser and a manual 3-paddle polarization controller. 2x2 power splitters were used at the input and output of the on-chip interferometer in order to characterize the dispersion properties of the fabricated device.

Measured interference fringes and detected peaks are marked in Figure 3.7a. Group delay is calculated from these detected peaks as $\tau = \frac{\lambda^2}{\Delta\lambda c}$, where $\Delta\lambda$ is the period of the consecutive interference fringes, and c is the speed of light. This experimentally calculated group delay is plotted in Figure 3.7b together with a polynomial

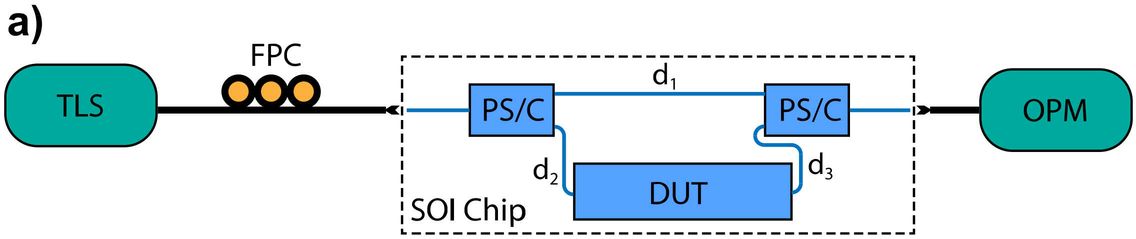

Figure 3.6: Illustration of the interference-based dispersion measurement setup.

fit. Finally, group delay dispersion is then calculated by using the derivative of this polynomial-fit group delay with respect to wavelength as $GDD = \frac{d\tau}{d\lambda}$. This dispersion result is plotted in Figure 3.7c, in agreement with the simulated result from Figure 3.5a (also replotted here in blue). Even though experimental dispersion is slightly narrower and blue-shifted, general profile as well as the maximum amount of dispersion match to the simulated dispersion.

The transmission measurements were performed using an independent replica of the same device placed separately on the same chip. The transmission results at outputs out_1 and out_2 were measured with an optical power meter, and plotted in Figure 3.7d. As predicted by transfer matrix simulations, majority of the output power was recorded at o1 across the measured spectrum. The measured insertion loss was less than 0.7dB within the 1.54 μm - 1.58 μm wavelength range. Slightly higher transmission loss in experiment compared to simulation can be explained by propagation losses and coupling deviation of directional couplers due to fabrication variations.

In general, increasing the number of design parameters makes it easier to achieve desired dispersion profile without compromising from transmission. In order to increase the number of parameters, one can increase the number of layers in the network. Another approach can be adding one more path to the structure and making it a 3-port network as shown in Figure 3.8a. This architecture allows light to take multiple paths depending on the wavelength and combine back at the end of the network which allows multiple control of the multiple spectral features independently. A step-like dispersion profile is optimized with a 3-port, 864 μm long

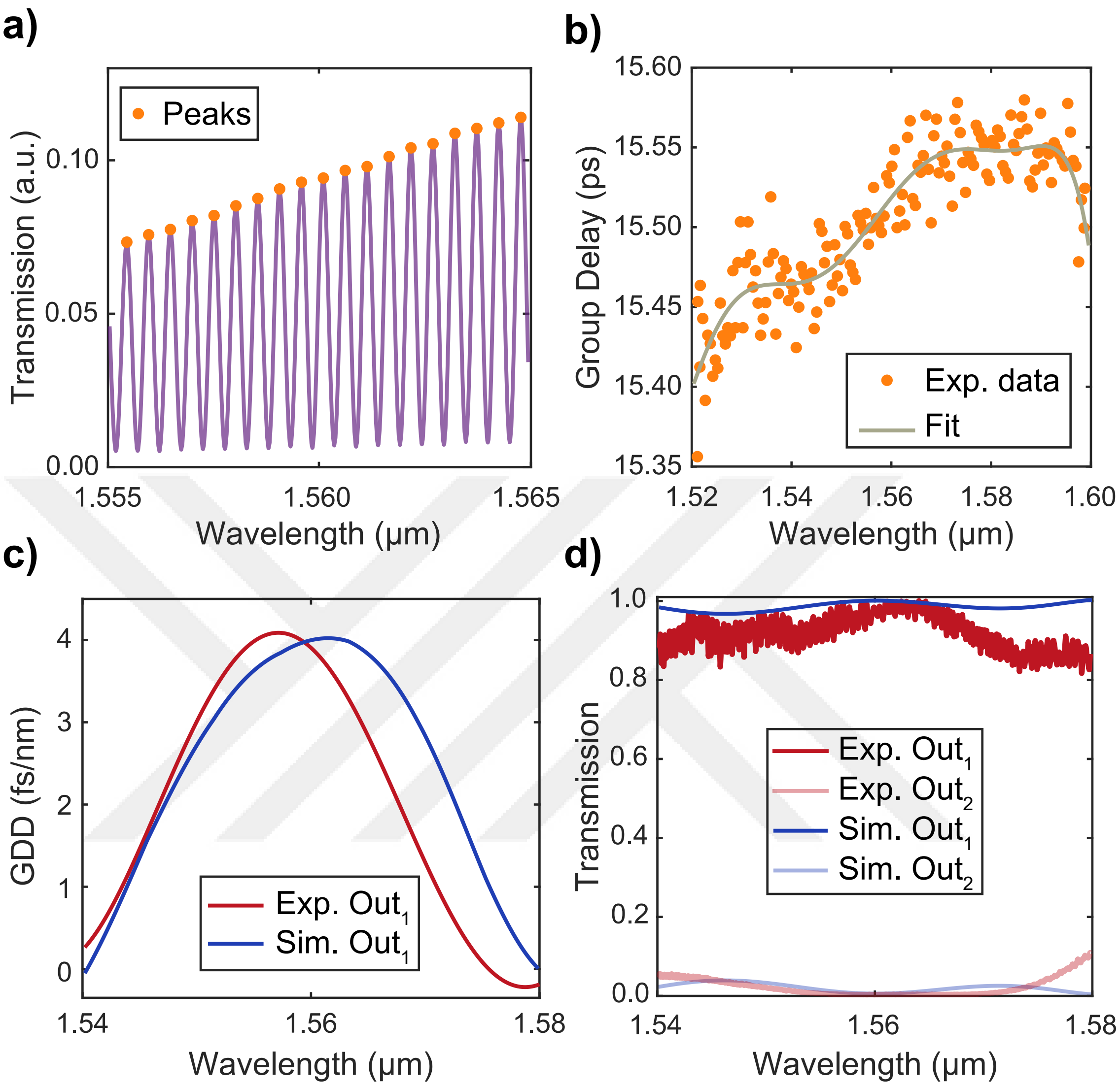

Figure 3.7: a) Measured interference fringes and peak values of the two-port network optimized for a specific dispersion profile. b) Calculated group delay from interference fringes. c) Calculated dispersion from the group-delay. d) Measured transmission responses of the network.

network plotted Figure 3.8a. As shown in the figure, an unorthodox dispersion profile is achieved with this structure that is not possible with a regular waveguide. A 24-layer and 2160 μm long 3-port network is optimized for a large dispersion with 2 nm bandwidth and its dispersion response is plotted in Figure 3.8a. The dispersion profile of a 2160 μm-long bare waveguide is also plotted (in orange). Specifically, this example device achieves up to 70x more dispersion within 2 nm bandwidth than a straight waveguide of equal length. This comparison proves the ability of the optimized deep photonic network to achieve custom dispersion profiles that are significantly different from what is possible with bare waveguides.

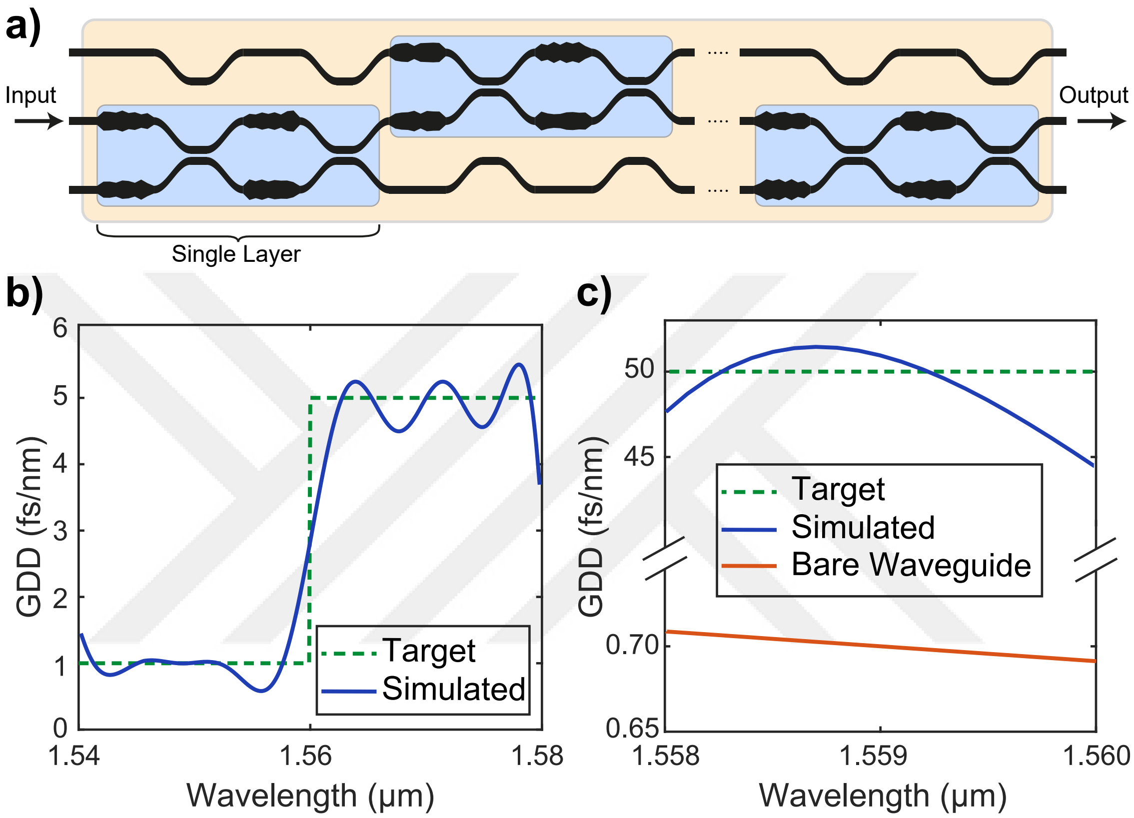

Figure 3.8: a) Schematic of 3-port photonic network architecture. b) Dispersion profile of a 3-port network optimized to have step-like dispersion. c) Dispersion profile of a 3-port network optimized to have a large dispersion.

3.4 Conclusion

In this study, we have proposed and experimentally demonstrated design and optimization of arbitrary dispersion profiles by using deep photonic networks with custom designed MZIs. High degree of freedom in optimizable phase delay sections of MZIs enables arbitrarily defined dispersion profiles with low loss. We demonstrate a proof-of-concept, triangle-like dispersion profile within a 40 nm bandwidth and less than 0.7 dB insertion loss with a two-port deep photonic network. We showed that our approach is scalable to bigger networks (3 or more ports) which provides more spectral features to be controlled independently. Future improvements to the device include adding length optimization of the phase delay sections to increase the dispersion strength and incorporating heaters for dynamic tuning of the dispersion.

Chapter 4

OPTIMIZING PHOTONIC DEVICES UNDER FABRICATION VARIATIONS WITH DEEP PHOTONIC NETWORKS

We propose a deep photonic interferometer network architecture for designing fabrication-tolerant photonic devices. Our framework incorporates layers of variation-aware, custom-designed Mach-Zehnder interferometers and virtual wafer maps to optimize broadband power splitters under fabrication variations. Specifically, we demonstrate 50/50 splitters with below 1% deviation from the desired 50/50 ratio, even with up to 10 nm over-etch and under-etch variations. The significantly improved device performance under fabrication-induced changes demonstrates the effectiveness of the deep photonic network architecture in designing fabrication-tolerant photonic devices, and showcases the potential for improving circuit performance by optimizing for expected variations in waveguide width.

4.1 Introduction

Integrated photonics is a rapidly growing field, to meet ever growing needs of communication applications [Rickman, 2014, Liu et al., 2022d] and also unlocking novel photonic functionalities in areas such as sensing [Iqbal et al., 2010], computation [Pasricha and Nikdast, 2020, Al-Qadasi et al., 2022], spectroscopy [Baets et al., 2013], and various other applications [Rogers et al., 2021, Marpaung et al., 2019]. Currently, there is a diverse range of material platforms available for constructing photonic integrated circuits, including III-V semiconductors (GaAs, InP), Lithium Niobate, glasses, polymers, and silicon. Of these options, silicon photonics stands out as a particularly promising technology due to its compatibility with the manufacturing processes utilized in the CMOS industry [Reed, 2008, Thomson et al., 2016]. This compatibility offers the potential for large-scale production at a significantly reduced cost per device. Another distinguishing characteristic of silicon photonics is its high refractive index contrast, enabling the scaling of waveguides to sub-micrometer dimensions[Bogaerts et al., 2013]. Consequently, this facilitates the compact integration of multiple optical functions on a single chip, immensely increasing the functionality of the chip.

However, the high refractive index contrast in silicon leads to strong confinement of optical mode to the waveguide which, in turn, imposes stringent dimensional requirements on silicon photonic circuits [Bogaerts and Chrostowski, 2018]. Even nanometer-scale variations in waveguide dimensions can lead to significant deviations from the desired performance of the photonic circuits. This becomes particularly critical for circuits such as interferometers that heavily rely on precise phase control and interference effects [Han et al., 2019, Horst et al., 2013]. Consequently, the variability introduced by the fabrication processes holds significant influence over the overall performance of these circuits and it is crucial to accurately quantify these variations in order to develop suitable mitigation strategies [Boning et al., 2021, Zhang et al., 2020, Lu et al., 2017].

Photonic integrated circuits can experience variations stemming from different factors. One factor is process conditions during chip fabrication, such as exposure dose, resist age, and alignment errors. Environmental conditions, including temperature and humidity, also contribute to performance variations in these circuits [Xing et al., 2022].

There are several techniques available to mitigate fabrication variations. One approach involves enhancing the manufacturing technology, such as improving lithography precision, to reduce variability. However, it is important to note that complete elimination of variations through manufacturing improvements alone may not be achievable. Another method involves improving the robustness of individual circuit components through multi-objective device optimizations [Zhang et al., 2019, Ruan et al., 2022]. However, this technique often relies on extensive device-level simulations, which may not always be practical or feasible. Alternatively, active tuning methods can be employed to mitigate the impact of fabrication variations [Lu et al., 2015]. However, this approach involves using electronic circuitry to control individual tuning elements which increases circuit complexity and power consumption.

While the aforementioned methods offer some relaxation of the impact of fabrication variations, it remains inevitable that each building block will exhibit a response that deviates from the ideal to some extent. As signals propagate through the circuit, these non-idealities accumulate, leading to further performance deviations. Hence, it becomes imperative to conduct a variability analysis that extends beyond the device level to the circuit level, particularly for large and complex circuits that are more susceptible to variability [Bogaerts and Chrostowski, 2018]. In a study by Lu et al., a simulation methodology was presented to forecast the influence of layout-dependent correlated fabrication variability on the performance of silicon photonics integrated circuits [Lu et al., 2017]. Numerous other works have also explored layout-aware variability analysis and yield prediction methods, recognizing the significance of understanding and addressing the impact of variabilities on circuit performance [James et al., 2023, El-Henawy et al., 2019, Zhang et al., 2023, Shafiee et al., 2022].

In this study, we propose a deep photonic network architecture aimed at designing complex photonic devices that are resilient to such fabrication variations. To this end, we demonstrate a framework that can optimize broadband photonic devices using a multi-objective approach including simultaneous consideration of device performance under different potential fabrication variations. The devices we demonstrate are constructed as deep photonic networks of cascaded Mach-Zehnder interferometers (MZIs) with compact models for components sensitive to fabrication variations. We optimize these structures using virtual wafer maps for correlated wafer-scale variations of the waveguide width throughout the interferometric layers. Specifically, we show that fabrication-tolerant, broadband 50/50 power splitters can achieve significantly better performance under over-etch and under-etch scenarios across their entire operation bandwidth from 1500nm to 1600nm, and maintain

$\pm 1\%$ transmission around the desired 50% for etch offsets of up to ± 10nm. Our approach demonstrates the effectiveness of the deep photonic network architecture in designing fabrication-tolerant photonic devices, and showcases the potential for improving circuit performance by optimizing for expected fabrication variations.

4.2 Photonic Network Architecture

Photonic networks can be designed in various configurations, such as binary-tree or rectangular architectures, typically comprising 2x2 blocks or meshes. In this context, we are focusing on a rectangular network architecture that utilizes Mach-Zehnder interferometers (MZIs). One of the key advantages of this network is its flexibility in setting the number of ports according to specific requirements.

Figure 4.1a and b showcase two-port and three-port deep photonic network schemes, both incorporating MZI units. Each MZI unit is capable of performing a 2x2 linear transformation, denoted as Ti, which allows for complex signal manipulation and processing.

In detail, Figure 4.1c provides a detailed representation of one of the MZI units employed in the network. This MZI unit consists of two directional couplers and two pairs of custom tapers, precisely engineered to achieve specific phase delays. The directional couplers are designed to function as 50/50 splitters at a wavelength of around 1570 nm, evenly dividing the incoming light into two paths.

The custom tapers serve as wavelength-dependent phase delay sections. Unlike light propagation in a straight waveguide, where dispersion remains constant, the optical properties of light in a waveguide with a custom width vary along the direction of propagation, depending on the frequency of the light. This unique characteristic of our network enables optimization of the waveguide's shape to provide a desired optical response.

The main objective here is to attain custom spectral phase profiles. Achieving this customization involves individually designing the width of each waveguide in the two arms of the interferometer. This special waveguide is expressed through a set of optimizable widths known as control points, as shown in Figure 4.1d.

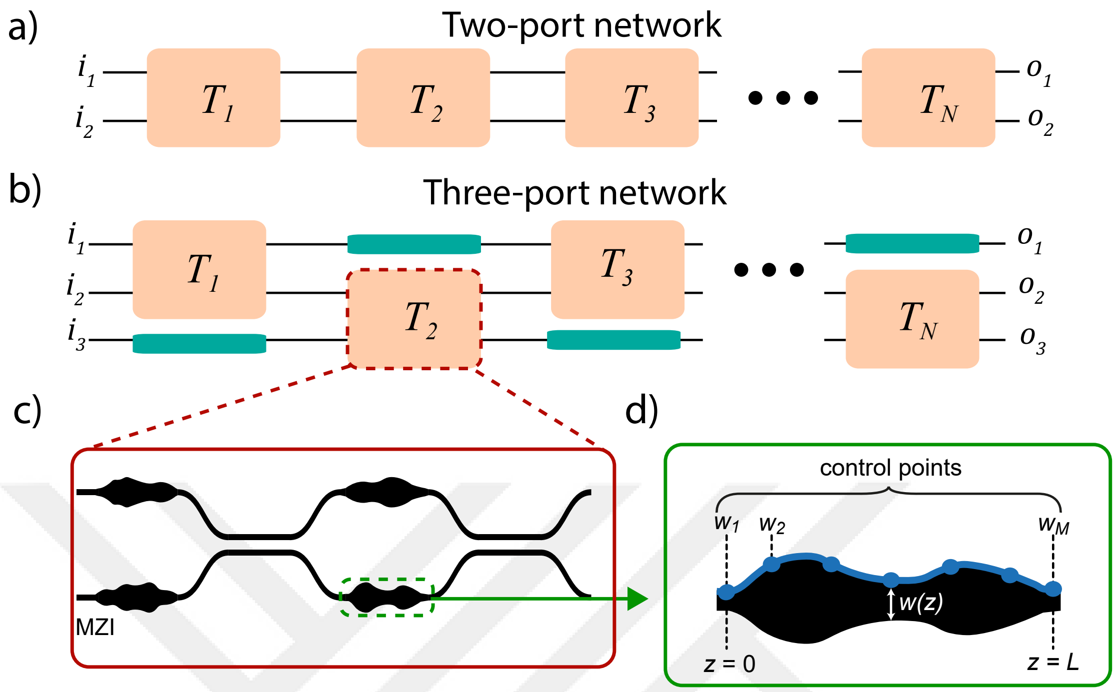

Figure 4.1: Photonic network architecture two-port (a) and three port (b) illustraions. c) Single MZI consisting of two splitters, implemented with directional couplers, and two tapers with custom geometries for achieving specific spectral phase profiles. d) Custom waveguide constructed from a set of trainable width parameters.

4.3 Effect of Fabrication Variations on the Components

Each Mach-Zehnder Interferometer (MZI) comprises two phase sections and two directional couplers. The coupling coefficient is a crucial design parameter of these directional couplers, as it, along with the length of the coupler, determines the power coupling to the cross port. This coefficient depends on the wavelength and geometry of the coupling structure, specifically the widths of individual waveguides and the gap between them. However, due to the inherent imperfections in fabrication processes, deviations from the ideal geometry of the directional coupler are inevitable, leading to variations in the coupling coefficient. Consequently, this alters the power splitting ratio of the directional couplers.

In Figure 4.2, we present transmission spectra of a directional coupler with a 10 um long coupling length under different fabrication variations. As depicted, there is an observed deviation of more than 5% from the nominal transmission. While this deviation may not have a significant impact on a single directional coupler, it becomes critical when considering a regular network that incorporates several, potentially tens of these couplers. The cumulative effect of such variations can substantially influence the overall response of the network, underscoring the importance of addressing fabrication-induced deviations in integrated photonic circuits.

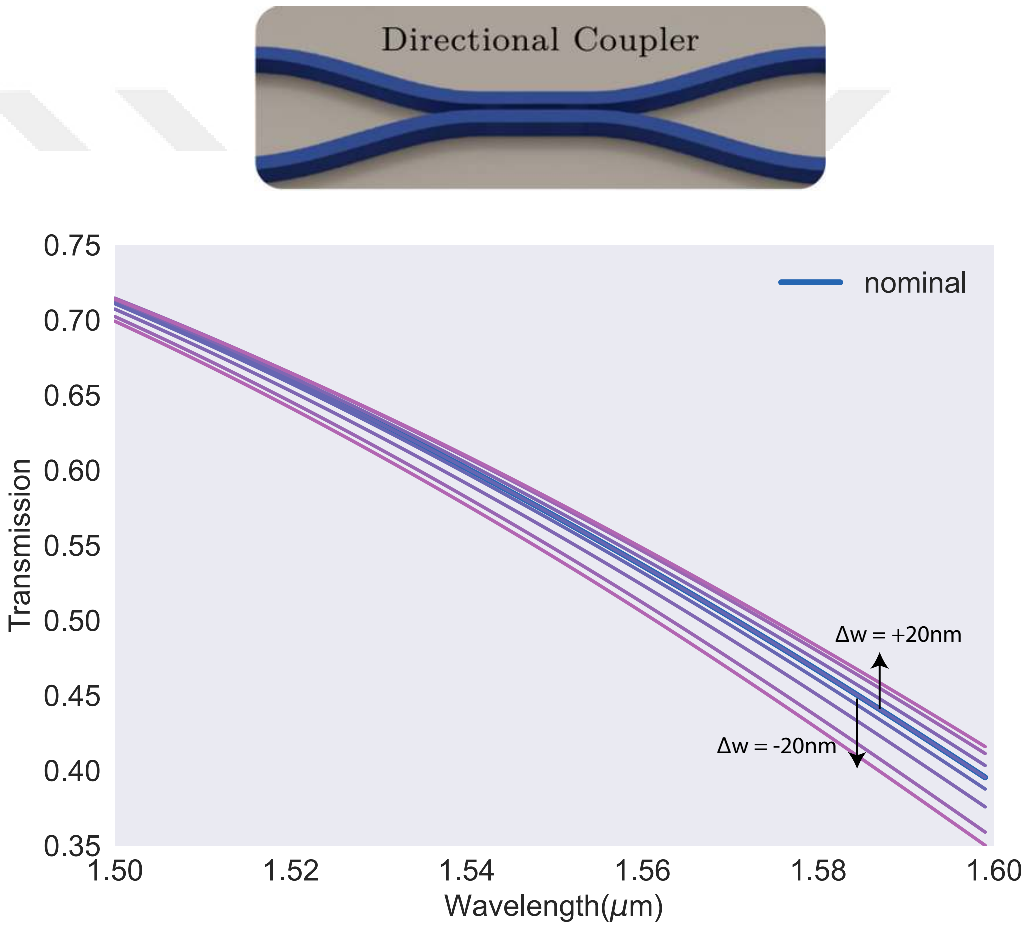

Figure 4.2: 3D illustration of directional coupler and its through port tranmission response under different under-etch and over-etch scenarios. Here Δw represents the width deviations.

Similarly, the custom waveguide tapers within the phase sections of the Mach-Zehnder Interferometer (MZI) are susceptible to potential fabrication variations. These variations can lead to deviations from the nominal design width, subsequently affecting the effective index of the custom waveguides and resulting in phase deviations from their intended values.

Figure 4.3 illustrates the impact of width deviations on the phase of a custom waveguide taper with a length of 10 um. As depicted, the deviations can be quite substantial, exceeding 1 radian. It is important to note that the phase of the custom waveguide is 2π periodic. Consequently, the figure showcases a 2π jump in the phase as deviations approach more negative values. The effect of phase deviations becomes particularly critical in our photonic geometry, as our devices are based on interferometers, which heavily rely on precise phase control and interference effects for their proper functioning. The accumulation of individual phase deviations can potentially introduce significant distortions to the overall network response.

The complex nature of our photonic devices, relying on interferometric interactions, makes them highly sensitive to variations. To address this challenge, it is imperative to create a realistic wafer map that captures the statistical and location-dependent aspects of the variability, particularly regarding systematic geometry variations. In our approach, we model the within-wafer manufacturing variations using a correlated surface roughness function, as reported by Lu et al [Lu et al., 2017]. First, we generate an uncorrelated random distribution map based on a discrete mesh of points. Each discrete point is assigned a random number following a normal distribution with a defined mean and standard deviation. Subsequently, this random function is convolved with a Gaussian filter to introduce correlation. Figure 4.4 illustrates two wafer map examples with different correlation lengths. Depending on the specific origin of the variations, an appropriate correlation length can be chosen to accurately represent and create the wafer maps.

4.4 Fabrication Tolerant Device Optimization

To enable fabrication-tolerant device optimizations, we initially developed compact models for each component in our photonic network. The directional coupler coefficients were obtained through interpolation of 3D finite difference time-domain simulations, considering the coupling coefficient as a function of both wavelength

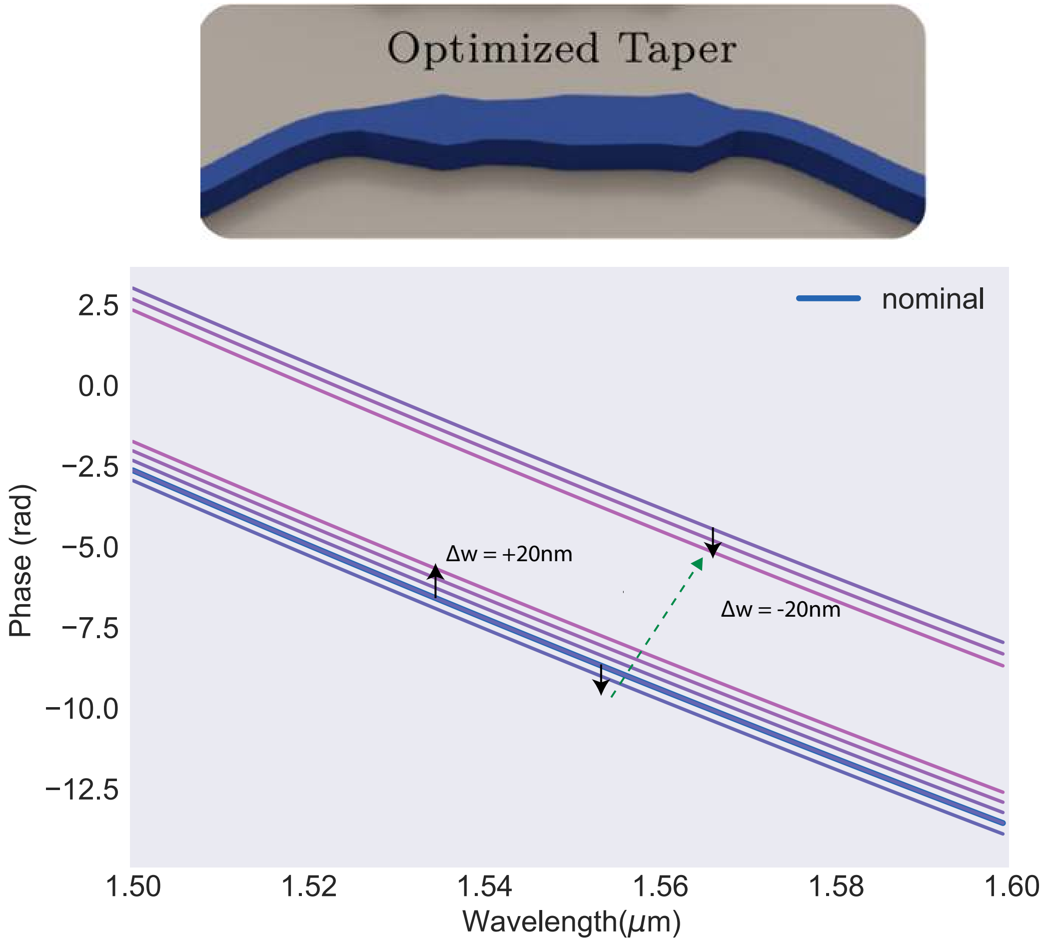

Figure 4.3: 3D illustration of custom waveguide taper and its phase response under different under-etch and over-etch scenarios.

and width variation. Effective indices were derived from pre-recorded data obtained through finite difference eigenmode calculations, utilizing the Silicon Photonics Toolkit package [Vit et al., 2022]. This comprehensive toolkit provides effective index data as a function of both wavelength and width. With these essential components equipped with compact models sensitive to fabrication variations, we constructed deep photonic networks comprising cascaded Mach-Zehnder interferometers (MZIs).

To illustrate the fabrication tolerance optimization feature of our network, we initially designed broadband 50/50 power splitters with 2-port networks, as depicted

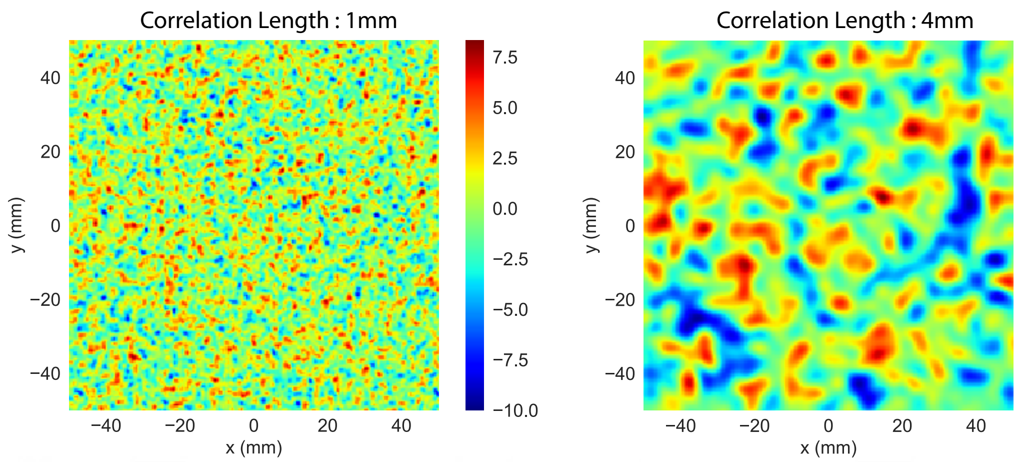

Figure 4.4: Virtual wafer maps with correlation lengths of 1 mm (left and 4 mm (right))

in Figure 4.5. At this stage, these splitters were not initially designed to be fabrication tolerant. The transmission response of both ports was plotted in the same figure, showcasing a desirable broadband splitting behavior.

Next, we subjected our network to a wafer map with a correlation length of 4 mm and width deviations of up to 10 nm. As demonstrated in Figure 4.6, the overall response of the network deviated from the original 50% splitting ratio by more than 7% at various locations across the wafer. The variability introduced by the fabrication processes holds significant influence over the overall performance of the device it is crucial to mitigate it.

In the subsequent step, we proceeded to re-optimize the network, this time instructing the optimizer to account for wafer map variations. During this optimization process, the network transmission was calculated at different locations of the wafer map simultaneously, aiming to optimize a structure that exhibits the best performance possible across all of these locations and width deviations. The results of this fabrication-tolerant optimization are shown in Figure 4.6. Remarkably, the broadband 50/50 power splitters achieved significantly improved performance under both over-etch and under-etch scenarios, covering their entire operating bandwidth from 1500 nm to 1600 nm. These optimized splitters effectively maintained a 1%

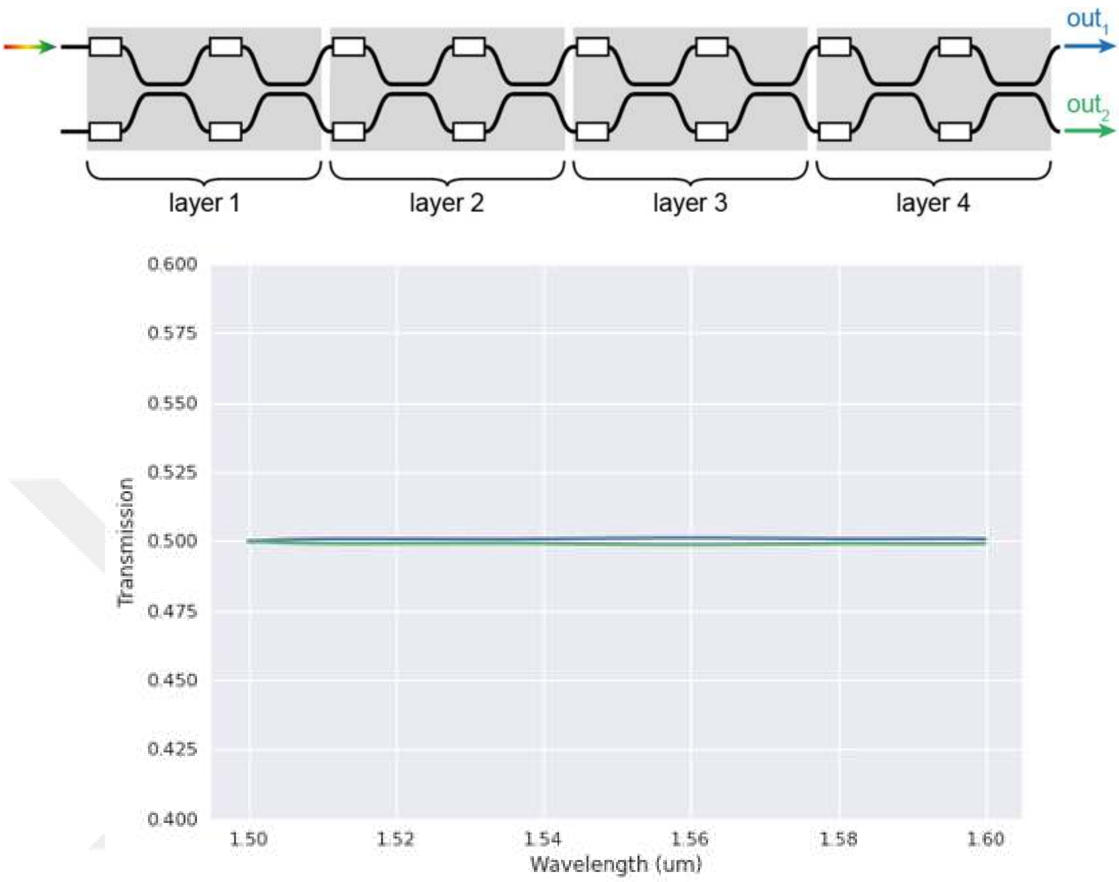

Figure 4.5: (Top) Illustration of a four-layer, two-port deep photonic network architecture. The optimized response of this network achieving a 50/50 splitting ratio, aligned with the designated objective.

transmission around the desired 50% splitting ratio for etch offsets of up to ±10 nm.

In non-tolerant optimization, the primary objective of the photonic network is to achieve a specific power splitting ratio. As a result, we can attain a small loss function in this ideal world optimization since the focus is solely on satisfying this particular criterion. However, in tolerant optimization, the approach is more challenging as the optimizer must consider the response of the photonic network across various locations on the wafer map, each with different width variations. The network is compelled to perform well in all these locations, making the optimization task more complex and difficult to achieve the same low loss as in the non-tolerant case. Figure 4.8 illustrates this difference, where the loss metric in the non-tolerant

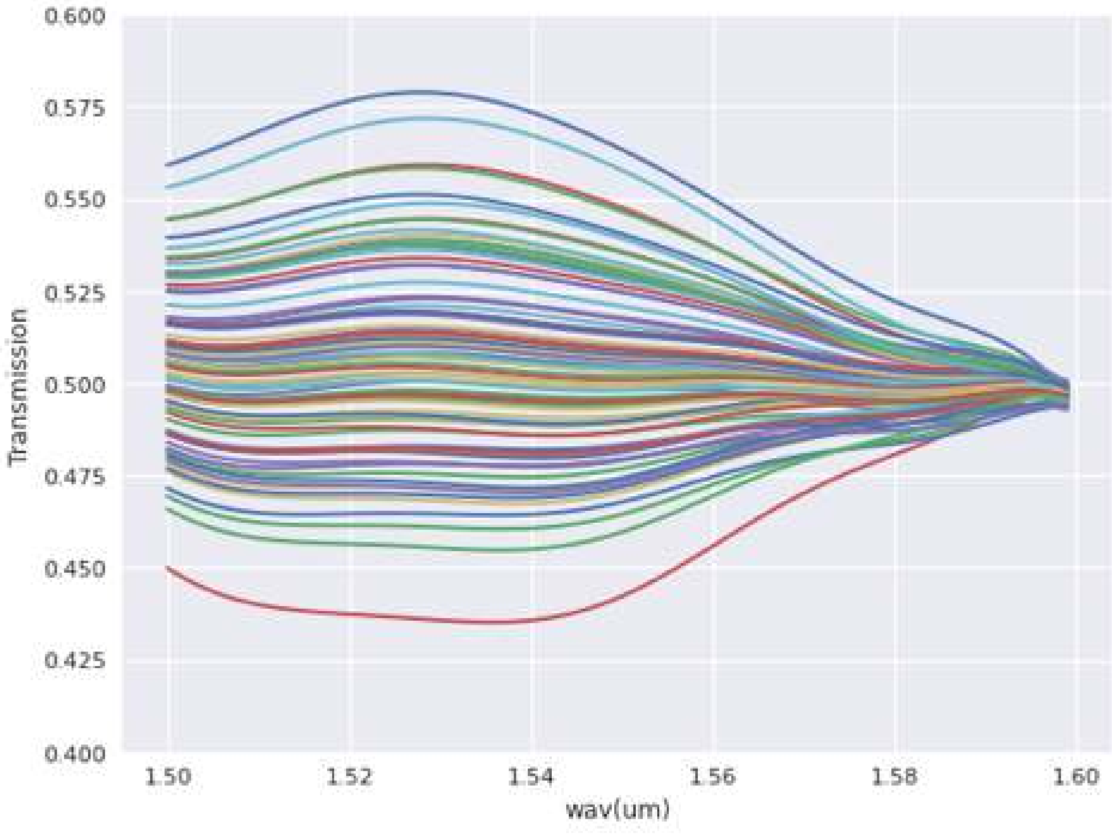

Figure 4.6: Transmission spectra of the non-fabrication tolerant network calculated on different locations of a wafer map of correlation length of 4 mm and width deviation of 10 nm

case is considerably lower than in the tolerant case. Despite the higher loss in the tolerant optimization, the performance of the tolerant version surpasses that of the non-tolerant version, as demonstrated in previous figures.

This optimization technique bears resemblance to noise-included training methods applied in deep neural networks to improve generalization [Noh et al., 2017, Goodfellow et al., 2016, Reed and MarksII, 1999, Bishop, 1995]. In standard noise-included training, noise is introduced during the training process to enhance the robustness of the model and reduce generalization error. Typically, this noise is added to the inputs, but it can also be incorporated into weights, gradients, or activation functions. In our photonic network optimization, we introduce noise in the form of fabrication variations to the input. By doing so, the network becomes less

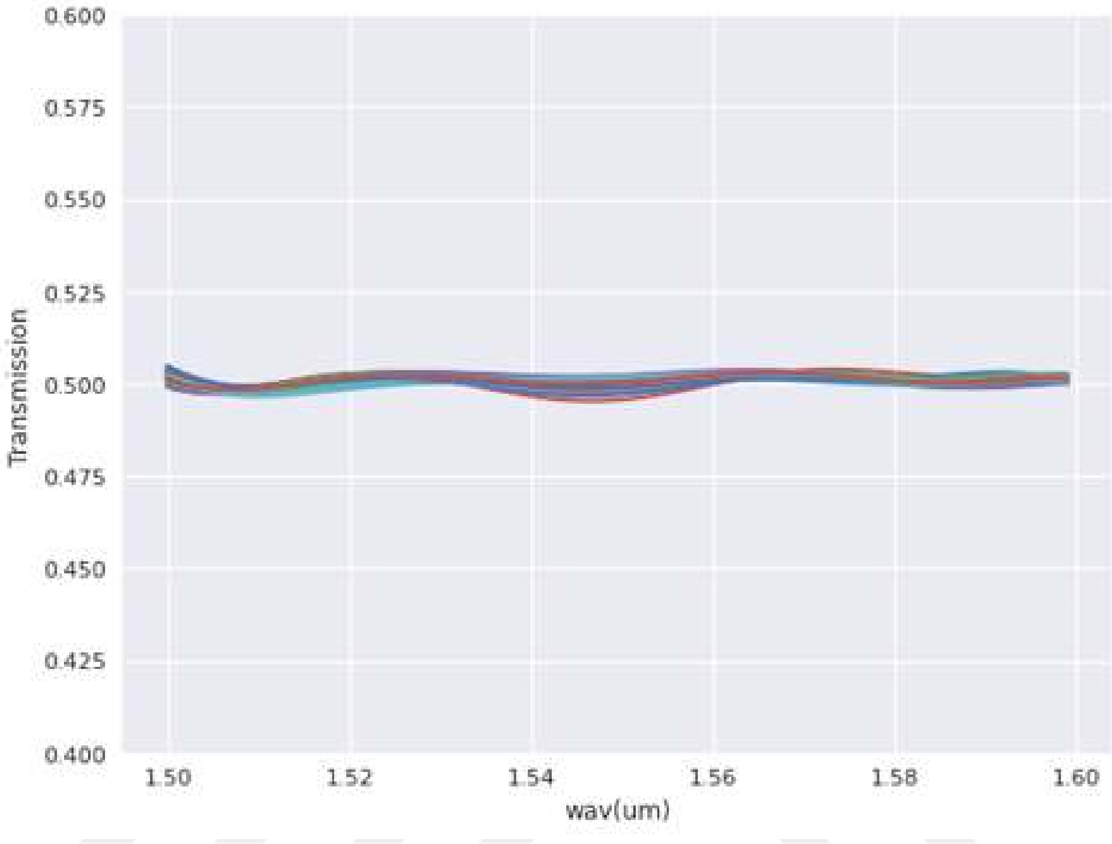

Figure 4.7: Transmission spectra of the fabrication tolerant network calculated on different locations of a wafer map of correlation length of 4 mm and width deviation of 10 nm

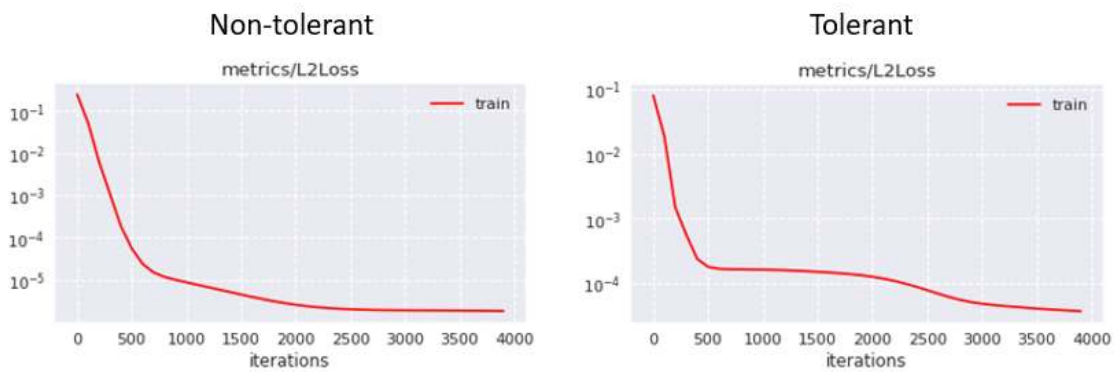

Figure 4.8: Training loss of non-tolerant and tolerant power splitter optimizations.

capable of memorizing specific training samples since they are constantly changing due to the added noise.

To investigate the impact of fabrication variations further, we conducted optimization experiments on 50/50 splitters with networks of varying layer sizes. Both fabrication-tolerant and non-tolerant versions of these splitters were optimized. For each network size, we performed 20 separate optimizations, calculating the maximum deviation from the desired 50% splitting ratio for each optimized network. Subsequently, we computed the average and standard deviations of these maximum difference values.

The results of these experiments are illustrated in Figure 4.9. As expected, the deviation from the ideal 50% splitting ratio is significantly higher in non-fabrication-tolerant devices. This observation is consistent with the notion that fabrication variations can introduce considerable uncertainties in the performance of photonic devices.

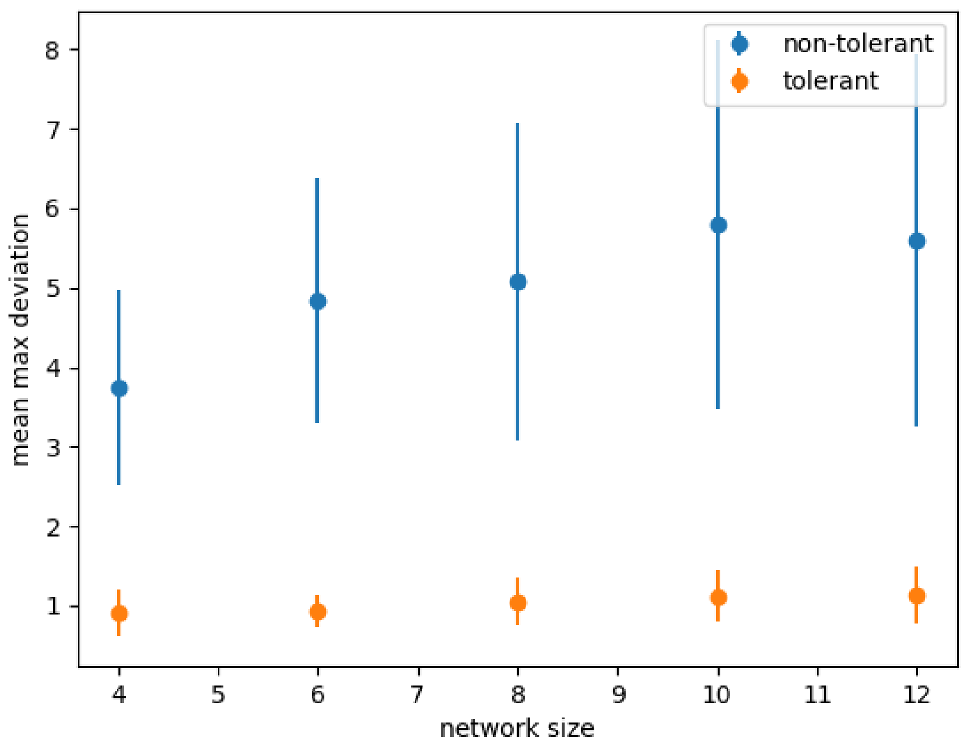

Figure 4.9: Maximum deviation from 50% splitting ratio for tolerant and non-tolerant networks as a function of network size

Furthermore, we observed that in general, the deviation from the desired splitting ratio tends to increase with network size. Larger networks appear to be more susceptible to the effects of fabrication-induced variations. However, it is worth noting that the effect of network size on fabrication-tolerant devices is not as apparent. This phenomenon might be attributed to the increased number of trainable parameters in larger networks. Larger networks offer more degrees of freedom for optimization, allowing them to adapt and optimize effectively even under fabrication variations.

These findings underscore the importance of incorporating fabrication tolerance in the design and optimization of photonic devices, especially as the complexity and size of photonic networks grow. Our fabrication-tolerant optimization approach proves to be a valuable strategy for mitigating the adverse effects of fabrication variations, ensuring consistent and reliable performance in integrated photonic circuits.

One notable advantage of implementing a fabrication-aware design flow is its ability to yield significant cost and time savings. This advantage is clearly demonstrated in Figure 4.10. The upper part of the figure depicts the conventional design flow, where the designer does not take into account any fabrication variations. As shown in this flow, each design cycle typically spans around one year, resulting in a situation where the impact of fabrication-related issues is only revealed after an entire year has elapsed. Such a delay is hardly acceptable in product design.

In contrast, the enhanced design flow, illustrated in the lower part of the figure, employs fabrication-aware models and wafer maps to guide the design of devices in consideration of fabrication variations. This approach facilitates prompt feedback to designers regarding the potential effects of specific fabrication variations, rendering the design stage more dependable. Consequently, it significantly reduces the need for a high number of design-layout-fabrication-test cycles.

Moreover, the improved design flow also enables optimization. With the use of compact models and layout-aware circuit simulations, designers can perform rapid analyses, which allows them to employ sophisticated optimization algorithms for refining their designs under various fabrication variations. This optimization capability enhances the overall design quality and helps in achieving higher performance levels for the end product.

By incorporating fabrication-awareness, the overall product development process becomes more efficient, reliable, and enables the creation of optimized designs that deliver superior performance under different fabrication scenarios.

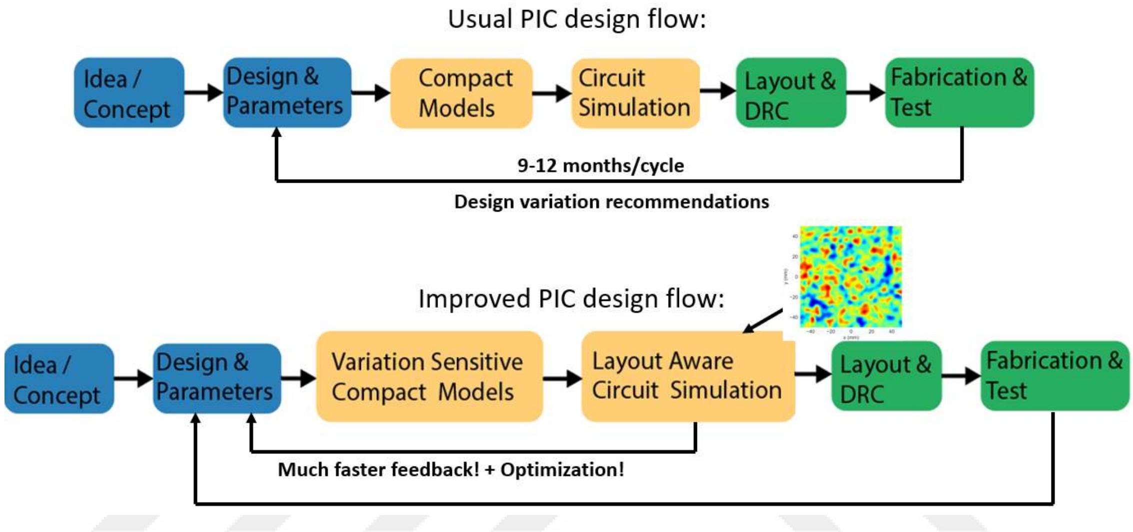

Figure 4.10: Conventional (top) vs fabrication variation aware (bottom) design flows for photonic integrated circuits

4.5 Conclusion

In conclusion, our work on fabrication-tolerant network optimizations in photonic devices has yielded promising results. By employing a deep photonic interferometer network architecture with variation-aware compact models and virtual wafer maps, we successfully designed photonic devices resilient to fabrication-induced variations.

The optimized broadband 50/50 power splitters exhibited deviations below 1% from the desired ratio, even under challenging fabrication scenarios with up to 10 nm over-etch and under-etch variations. This highlights the effectiveness of our approach in creating fabrication-tolerant photonic devices.

Moreover, our experiments on networks of different sizes revealed that non-fabrication-tolerant devices experienced higher deviations as the network size increased, while fabrication-tolerant devices remained stable. The incorporation of variation-aware modeling and fabrication-tolerant optimization ensures robust and reliable performance across various conditions.

Overall, our fabrication-tolerant network optimization approach holds promise in advancing integrated photonics technology, enabling high-performance photonic devices for diverse applications. As the field continues to grow, our work contributes to the development of reliable photonic systems, advancing cutting-edge technologies in this field.

Chapter 5

CONCLUSION

In conclusion, this thesis work has explored and demonstrated the potential of silicon photonics as a highly promising platform for large-scale photonic circuits. Leveraging the advantages of CMOS fabrication technology, silicon photonics offers scalability, reliable manufacturing processes, and cost-effectiveness, making it a viable and industrially attractive option.

The research addressed the growing demand for customized photonic integrated circuits with high-performance capabilities. The design of broadband silicon photonic filters and deep photonic networks with custom dispersion profiles exemplified the efforts in meeting these requirements. The ultra-broadband silicon photonic filters demonstrated exceptional performance, achieving flat-band transmission with flexible bandwidths of over 100 nm. Additionally, deep photonic networks showcased the ability to achieve arbitrarily defined dispersion profiles, offering a wide range of applications in optical signal processing and communication.

One of the significant achievements of this work was the development of fabrication variation-tolerant photonic devices through variation-aware optimization of deep photonic networks. By considering potential fabrication-induced variations, the study demonstrated the creation of highly robust and reliable photonic devices, ensuring consistent performance across varying conditions.

In summary, this thesis contributes to the advancement of integrated photonics technology, revealing the potential of silicon photonics as a powerful platform for large-scale photonic circuits. The optimization of photonic components, deep photonic networks, and the consideration of fabrication tolerance enhance the design and performance of photonic devices, advancing the progress in various applications and accelerating the realization of cutting-edge photonic systems and technologies.

BIBLIOGRAPHY

[Tra, 2020] (2020). Trax: an end-to-end library for deep learning that focuses on clear code and speed, https://github.com/google/trax.

[Akca and Doerr, 2018] Akca, B. I. and Doerr, C. R. (2018). Interleaved silicon nitride awg spectrometers. *IEEE Photonics Technology Letters*, 31(1):90–93.

[Al-Qadasi et al., 2022] Al-Qadasi, M., Chrostowski, L., Shastri, B., and Shekhar, S. (2022). Scaling up silicon photonic-based accelerators: Challenges and opportunities. *APL Photonics*, 7(2).

[Amiri et al., 2022] Amiri, A. N., Vit, A. D., Gorgulu, K., and Magden, E. S. (2022). Optical neural networks with arbitrary and wideband photonic functionality. In *Laser Science*, pages JW4B–40. Optica Publishing Group.

[Amiri et al., 2023] Amiri, A. N., Vit, A. D., Gorgulu, K., and Magden, E. S. (2023). Deep photonic networks with arbitrary and broadband functionality. *arXiv preprint arXiv:2304.04776*.

[Ashtiani et al., 2022] Ashtiani, F., Geers, A. J., and Aflatouni, F. (2022). An on-chip photonic deep neural network for image classification. *Nature*, 606(7914):501–506.

[Baets et al., 2013] Baets, R., Subramanian, A. Z., Dhakal, A., Selvaraja, S. K., Komorowska, K., Peyskens, F., Ryckeboer, E., Yebo, N., Roelkens, G., and Le Thomas, N. (2013). Spectroscopy-on-chip applications of silicon photonics. In *Integrated optics: Devices, materials, and technologies XVII*, volume 8627, pages 87–96. Spie.

[Biberman et al., 2012] Biberman, A., Shaw, M. J., Timurdogan, E., Wright, J. B., and Watts, M. R. (2012). Ultralow-loss silicon ring resonators. *Optics letters*, 37(20):4236–4238.

[Bishop, 1995] Bishop, C. M. (1995). Training with noise is equivalent to tikhonov regularization. *Neural computation*, 7(1):108–116.

[Bogaerts and Chrostowski, 2018] Bogaerts, W. and Chrostowski, L. (2018). Silicon photonics circuit design: methods, tools and challenges. *Laser & Photonics Reviews*, 12(4):1700237.

[Bogaerts et al., 2012] Bogaerts, W., De Heyn, P., Van Vaerenbergh, T., De Vos, K., Kumar Selvaraja, S., Claes, T., Dumon, P., Bienstman, P., Van Thourhout, D., and Baets, R. (2012). Silicon microring resonators. *Laser & Photonics Reviews*, 6(1):47–73.

[Bogaerts et al., 2013] Bogaerts, W., Fiers, M., and Dumon, P. (2013). Design challenges in silicon photonics. *IEEE Journal of Selected Topics in Quantum Electronics*, 20(4):1–8.

[Bogaerts et al., 2016] Bogaerts, W., Fiers, M., Sivilotti, M., and Dumon, P. (2016). The ipkiss photonic design framework. In *Optical Fiber Communication Conference*, pages W1E–1. Optica Publishing Group.

[Bogaerts et al., 2020] Bogaerts, W., Pérez, D., Capmany, J., Miller, D. A., Poon, J., Englund, D., Morichetti, F., and Melloni, A. (2020). Programmable photonic circuits. *Nature*, 586(7828):207–216.

[Boning et al., 2021] Boning, D. S., El-Henawy, S. I., and Zhang, Z. (2021). Variation-aware methods and models for silicon photonic design-for-manufacturability. *Journal of Lightwave Technology*, 40(6):1776–1783.

[Bradbury et al., 2018] Bradbury, J., Frostig, R., Hawkins, P., Johnson, M. J., Leary, C., Maclaurin, D., Necula, G., Paszke, A., VanderPlas, J., Wanderman-Milne, S., and Zhang, Q. (2018). JAX: composable transformations of Python+NumPy programs, http://github.com/google/jax.

[Brouckaert et al., 2007] Brouckaert, J., Bogaerts, W., Dumon, P., Van Thourhout, D., and Baets, R. (2007). Planar concave grating demultiplexer fabricated on a nanophotonic silicon-on-insulator platform. *Journal of Lightwave Technology*, 25(5):1269–1275.

[Chen et al., 2013] Chen, G., Wang, T., Donnelly, C., and Tan, D. (2013). Second and third order dispersion generation using nonlinearly chirped silicon waveguide gratings. *Optics Express*, 21(24):29223–29230.

[Chen et al., 2014] Chen, P., Chen, S., Guan, X., Shi, Y., and Dai, D. (2014). High-order microring resonators with bent couplers for a box-like filter response. *optics letters*, 39(21):6304–6307.

[Chen et al., 2015] Chen, S., Fu, X., Wang, J., Shi, Y., He, S., and Dai, D. (2015). Compact dense wavelength-division (de) multiplexer utilizing a bidirectional arrayed-waveguide grating integrated with a mach–zehnder interferometer. *Journal of Lightwave Technology*, 33(11):2279–2285.

[Cheng et al., 2020] Cheng, L., Mao, S., Li, Z., Han, Y., and Fu, H. (2020). Grating couplers on silicon photonics: Design principles, emerging trends and practical issues. *Micromachines*, 11(7):666.

[Cheng and Chrostowski, 2020] Cheng, R. and Chrostowski, L. (2020). Spectral design of silicon integrated bragg gratings: A tutorial. *Journal of Lightwave Technology*, 39(3):712–729.

[Chrostowski and Hochberg, 2015] Chrostowski, L. and Hochberg, M. (2015). *Silicon photonics design: from devices to systems*. Cambridge University Press.

[Chung and Tseng, 2018] Chung, H.-C. and Tseng, S.-Y. (2018). Ultrashort and broadband silicon polarization splitter-rotator using fast quasiadiabatic dynamics. *Optics Express*, 26(8):9655–9665.

[Dai, 2017] Dai, D. (2017). Silicon nanophotonic integrated devices for on-chip multiplexing and switching. *Journal of Lightwave Technology*, 35(4):572–587.

[Dai and Bowers, 2011] Dai, D. and Bowers, J. E. (2011). Novel concept for ultra-compact polarization splitter-rotator based on silicon nanowires. *Optics express*, 19(11):10940–10949.

[Dai and Bowers, 2014] Dai, D. and Bowers, J. E. (2014). Silicon-based on-chip multiplexing technologies and devices for peta-bit optical interconnects. *Nanophotonics*, 3(4-5):283–311.

[De Vos et al., 2007] De Vos, K., Bartolozzi, I., Schacht, E., Bienstman, P., and Baets, R. (2007). Silicon-on-insulator microring resonator for sensitive and label-free biosensing. *Optics express*, 15(12):7610–7615.

[DeCorby et al., 2005] DeCorby, R. G., Ponnampalam, N., Pai, M. M., Nguyen, H. T., Dwivedi, P. K., Clement, T. J., Haugen, C. J., McMullin, J. N., and Kasap, S. O. (2005). High index contrast waveguides in chalcogenide glass and polymer. *IEEE Journal of selected topics in quantum electronics*, 11(2):539–546.

[Doerr et al., 2016] Doerr, C., Chen, L., Nielsen, T., Aroca, R., Chen, L., Banaee, M., Azemati, S., McBrien, G., Park, S., Geyer, J., et al. (2016). O, e, s, c, and l band silicon photonics coherent modulator/receiver. In *2016 Optical Fiber Communications Conference and Exhibition (OFC)*, pages 1–3. IEEE.

[Doerr, 2015] Doerr, C. R. (2015). Silicon photonic integration in telecommunications. *Frontiers in Physics*, 3:37.

[Dolgaleva et al., 2011] Dolgaleva, K., Malacarne, A., Tannouri, P., Fernandes, L. A., Grenier, J. R., Aitchison, J. S., Azaña, J., Morandotti, R., Herman, P. R., and Marques, P. V. (2011). Integrated optical temporal fourier transformer based on a chirped bragg grating waveguide. *Optics letters*, 36(22):4416–4418.

[Dong et al., 2014] Dong, P., Chen, Y.-K., Duan, G.-H., and Neilson, D. T. (2014). Silicon photonic devices and integrated circuits. *Nanophotonics*, 3(4-5):215–228.

[Dumon et al., 2004] Dumon, P., Bogaerts, W., Wiaux, V., Wouters, J., Beckx, S., Van Campenhout, J., Taillaert, D., Luyssaert, B., Bienstman, P., Van Thourhout, D., et al. (2004). Low-loss soi photonic wires and ring resonators fabricated with deep uv lithography. *IEEE Photonics Technology Letters*, 16(5):1328–1330.

[Dutt et al., 2018] Dutt, A., Joshi, C., Ji, X., Cardenas, J., Okawachi, Y., Luke, K., Gaeta, A. L., and Lipson, M. (2018). On-chip dual-comb source for spectroscopy. *Science advances*, 4(3):e1701858.

[Eggleton, 2001] Eggleton, B. J. (2001). Dynamic dispersion compensation devices for high speed transmission systems. In *Optical Fiber Communication Conference*, page WH1. Optica Publishing Group.

[El-Henawy et al., 2019] El-Henawy, S. I., Zhang, Z., Miller, R., and Boning, D. S. (2019). Photonic device sensitivity analysis methods: towards process variation-aware silicon photonics design. In *Optical Modeling and System Alignment*, volume 11103, pages 185–195. SPIE.

[Eldada and Shacklette, 2000] Eldada, L. and Shacklette, L. W. (2000). Advances in polymer integrated optics. *IEEE Journal of selected topics in quantum electronics*, 6(1):54–68.

[Fernández Gavela et al., 2016] Fernández Gavela, A., Grajales García, D., Ramirez, J. C., and Lechuga, L. M. (2016). Last advances in silicon-based optical biosensors. *sensors*, 16(3):285.

[Goda and Jalali, 2013] Goda, K. and Jalali, B. (2013). Dispersive fourier transformation for fast continuous single-shot measurements. *Nature Photonics*, 7(2):102–112.

[Goodfellow et al., 2016] Goodfellow, I., Bengio, Y., and Courville, A. (2016). *Deep learning*. MIT press.

[Gorgulu and Magden, 2021] Gorgulu, K. and Magden, E. S. (2021). Compact and broadband silicon photonic multiplexers based on fast adiabatic structures. In *CLEO: QELS_Fundamental Science*, pages JW1A–23. Optica Publishing Group.

[Gorgulu and Magden, 2022] Gorgulu, K. and Magden, E. S. (2022). Compact adiabatic silicon photonic filters with arbitrary and ultra-broadband response. In *Optical Fiber Communication Conference*, pages Th4C–3. Optica Publishing Group.

[Gorgulu and Magden, 2023] Gorgulu, K. and Magden, E. S. (2023). Ultra-broadband integrated optical filters based on adiabatic optimization of coupled waveguides. *Journal of Lightwave Technology*.

[Gross et al., 2014] Gross, S., Riesen, N., Love, J. D., and Withford, M. J. (2014). Three-dimensional ultra-broadband integrated tapered mode multiplexers. *Laser & Photonics Reviews*, 8(5):L81–L85.

[Guo and Chu, 2017] Guo, D. and Chu, T. (2017). Silicon mode (de) multiplexers with parameters optimized using shortcuts to adiabaticity. *Optics express*, 25(8):9160–9170.

[Hammood et al., 2019] Hammood, M., Mistry, A., Ma, M., Yun, H., Chrostowski, L., and Jaeger, N. A. (2019). Compact, silicon-on-insulator, series-cascaded, contradirectional-coupling-based filters with¿ 50 db adjacent channel isolation. *Optics letters*, 44(2):439–442.

[Hammood et al., 2021] Hammood, M., Mistry, A., Yun, H., Ma, M., Lin, S., Chrostowski, L., and Jaeger, N. A. (2021). Broadband, silicon photonic, optical add–drop filters with 3 db bandwidths up to 11 thz. *Optics Letters*, 46(11):2738–2741.

[Han et al., 2018] Han, L., Kuo, B. P.-P., Alic, N., and Radic, S. (2018). Ultra-broadband multimode 3db optical power splitter using an adiabatic coupler and a y-branch. *Optics Express*, 26(11):14800–14809.

[Han et al., 2019] Han, L., Kuo, B. P.-P., Pejkic, A., Alic, N., and Radic, S. (2019). 50ghz silicon cascaded mach-zehnder wavelength filter and automatic phase error correction. In *2019 Optical Fiber Communications Conference and Exhibition (OFC)*, pages 1–3. IEEE.

[Harris et al., 2018] Harris, N. C., Carolan, J., Bunandar, D., Prabhu, M., Hochberg, M., Baehr-Jones, T., Fanto, M. L., Smith, A. M., Tison, C. C., Alsing, P. M., et al. (2018). Linear programmable nanophotonic processors. *Optica*, 5(12):1623–1631.

[Haus, 1984] Haus, H. A. (1984). Waves and fields in optoelectronics. *(No Title)*.

[Horst et al., 2013] Horst, F., Green, W. M., Assefa, S., Shank, S. M., Vlasov, Y. A., and Offrein, B. J. (2013). Cascaded mach-zehnder wavelength filters in silicon photonics for low loss and flat pass-band wdm (de-) multiplexing. *Optics express*, 21(10):11652–11658.

[Hung et al., 2019] Hung, Y.-J., Li, Z.-Y., Chung, H.-C., Liang, F.-C., Jung, M.-Y., Yen, T.-H., and Tseng, S.-Y. (2019). Mode-evolution-based silicon-on-insulator 3 db coupler using fast quasiadiabatic dynamics. *Optics Letters*, 44(4):815–818.

[Imec,] Imec, R. im. `https://www.imec-int.com/en/silicon-photonic-ICs-prototyping` [Accessed: 2023-07-10].

[Iqbal et al., 2010] Iqbal, M., Gleeson, M. A., Spaugh, B., Tybor, F., Gunn, W. G., Hochberg, M., Baehr-Jones, T., Bailey, R. C., and Gunn, L. C. (2010). Label-free biosensor arrays based on silicon ring resonators and high-speed optical scanning instrumentation. *IEEE Journal of selected topics in quantum electronics*, 16(3):654–661.

[Jalali and Fathpour, 2006] Jalali, B. and Fathpour, S. (2006). Silicon photonics. *Journal of lightwave technology*, 24(12):4600–4615.

[James et al., 2023] James, A., Rizzo, A., Wang, Y., Novick, A., Wang, S., Parsons, R., Jang, K., Hattink, M., and Bergman, K. (2023). Process variation-aware compact model of strip waveguides for photonic circuit simulation. *Journal of Lightwave Technology*, 41(9):2801–2814.

[Khan et al., 2010] Khan, M. H., Shen, H., Xuan, Y., Zhao, L., Xiao, S., Leaird, D. E., Weiner, A. M., and Qi, M. (2010). Ultrabroad-bandwidth arbitrary radiofrequency waveform generation with a silicon photonic chip-based spectral shaper. *Nature Photonics*, 4(2):117–122.

[Lam et al., 2010] Lam, C. F., Liu, H., Koley, B., Zhao, X., Kamalov, V., and Gill, V. (2010). Fiber optic communication technologies: What's needed for datacenter network operations. *IEEE Communications Magazine*, 48(7):32–39.

[Liao et al., 2005] Liao, L., Samara-Rubio, D., Morse, M., Liu, A., Hodge, D., Rubin, D., Keil, U. D., and Franck, T. (2005). High speed silicon mach-zehnder modulator. *Optics express*, 13(8):3129–3135.

[Lifante, 2003] Lifante, G. (2003). *Integrated photonics: fundamentals*. John Wiley & Sons.

[Lim et al., 2013] Lim, A. E.-J., Song, J., Fang, Q., Li, C., Tu, X., Duan, N., Chen, K. K., Tern, R. P.-C., and Liow, T.-Y. (2013). Review of silicon photonics foundry efforts. *IEEE Journal of Selected Topics in Quantum Electronics*, 20(4):405–416.

[Lin et al., 2021] Lin, Y.-X., Younesi, M., Chung, H.-P., Chiu, H.-K., Geiss, R., Tseng, Q.-H., Setzpfandt, F., Pertsch, T., and Chen, Y.-H. (2021). Ultra-compact, broadband adiabatic passage optical couplers in thin-film lithium niobate on insulator waveguides. *Optics Express*, 29(17):27362–27372.

[Liu et al., 2004] Liu, A., Jones, R., Liao, L., Samara-Rubio, D., Rubin, D., Cohen, O., Nicolaescu, R., and Paniccia, M. (2004). A high-speed silicon optical modulator based on a metal–oxide–semiconductor capacitor. *Nature*, 427(6975):615–618.

[Liu et al., 2021] Liu, D., Xu, H., Tan, Y., Shi, Y., and Dai, D. (2021). Silicon photonic filters. *Microwave and Optical Technology Letters*, 63(9):2252–2268.

[Liu et al., 2022a] Liu, J., Bo, F., Chang, L., Dong, C.-H., Ou, X., Regan, B., Shen, X., Song, Q., Yao, B., Zhang, W., et al. (2022a). Emerging material platforms for integrated microcavity photonics. *Science China Physics, Mechanics & Astronomy*, 65(10):104201.

[Liu et al., 2022b] Liu, S., Feng, J., Tian, Y., Zhao, H., Jin, L., Ouyang, B., Zhu, J., and Guo, J. (2022b). Thermo-optic phase shifters based on silicon-on-insulator platform: State-of-the-art and a review. *Frontiers of Optoelectronics*, 15(1):9.

[Liu et al., 2023] Liu, S., Zhang, C., Cao, H., Hong, S., Yu, Z., and Dai, D. (2023). On-chip circulator-free chirped spiral multimode waveguide grating for dispersion management. *ACS Photonics*, 10(5):1654–1661.

[Liu et al., 2022c] Liu, Y., Lu, L., Ni, Z., Chen, J., Chen, J., and Zhou, L. (2022c). Silicon integrated continuously tunable dispersion compensator based on cascaded micro-ring resonators. In *2022 Asia Communications and Photonics Conference (ACP)*, pages 1352–1355. IEEE.

[Liu et al., 2022d] Liu, Y., Wang, S., Wang, J., Li, X., Yu, M., and Cai, Y. (2022d). Silicon photonic transceivers in the field of optical communication. *Nano Communication Networks*, 31:100379.

[Lu et al., 2015] Lu, L., Zhou, L., Li, Z., Li, X., and Chen, J. (2015). Broadband $4x4$ nonblocking silicon electrooptic switches based on mach-zehnder interferometers. *IEEE Photonics Journal*, 7(1):1–8.

[Lu et al., 2017] Lu, Z., Jhoja, J., Klein, J., Wang, X., Liu, A., Flueckiger, J., Pond, J., and Chrostowski, L. (2017). Performance prediction for silicon photonics integrated circuits with layout-dependent correlated manufacturing variability. *Optics express*, 25(9):9712–9733.

[Luan et al., 2018] Luan, E., Shoman, H., Ratner, D. M., Cheung, K. C., and Chrostowski, L. (2018). Silicon photonic biosensors using label-free detection. *Sensors*, 18(10):3519.

[Luque-González et al., 2021] Luque-González, J. M., Sánchez-Postigo, A., Hadij-ElHouati, A., Ortega-Moñux, A., Wangüemert-Pérez, J. G., Schmid, J. H., Cheben, P., Molina-Fernández, Í., and Halir, R. (2021). A review of silicon subwavelength gratings: building break-through devices with anisotropic metamaterials. *Nanophotonics*, 10(11):2765–2797.

[Madsen and Lenz, 1998] Madsen, C. and Lenz, G. (1998). Optical all-pass filters for phase response design with applications for dispersion compensation. *IEEE Photonics Technology Letters*, 10(7):994–996.

[Madsen et al., 1999] Madsen, C. K., Lenz, G., Bruce, A. J., Cappuzzo, M., Gomez, L., and Scotti, R. (1999). Integrated all-pass filters for tunable dispersion and dispersion slope compensation. *IEEE Photonics Technology Letters*, 11(12):1623–1625.

[Magden et al., 2018] Magden, E. S., Li, N., Raval, M., Poulton, C. V., Ruocco, A., Singh, N., Vermeulen, D., Ippen, E. P., Kolodziejski, L. A., and Watts, M. R. (2018). Transmissive silicon photonic dichroic filters with spectrally selective waveguides. *Nature communications*, 9(1):3009.

[Margalit et al., 2021] Margalit, N., Xiang, C., Bowers, S. M., Bjorlin, A., Blum, R., and Bowers, J. E. (2021). Perspective on the future of silicon photonics and electronics. *Applied Physics Letters*, 118(22).

[Marpaung et al., 2019] Marpaung, D., Yao, J., and Capmany, J. (2019). Integrated microwave photonics. *Nature photonics*, 13(2):80–90.

[Menchon-Enrich et al., 2013] Menchon-Enrich, R., Llobera, A., Vila-Planas, J., Cadarso, V. J., Mompart, J., and Ahufinger, V. (2013). Light spectral filtering based on spatial adiabatic passage. *Light: Science & Applications*, 2(8):e90–e90.

[Mikkelsen et al., 2018] Mikkelsen, J., Bois, A., Lordello, T., Mahgerefteh, D., Menezo, S., and Poon, J. (2018). Polarization-insensitive silicon nitride mach-zehnder lattice wavelength demultiplexers for cwdm in the o-band. *Optics express*, 26(23):30076–30084.

[Miller, 2009] Miller, D. A. (2009). Device requirements for optical interconnects to silicon chips. *Proceedings of the IEEE*, 97(7):1166–1185.

[Misra et al., 2020] Misra, A., Preußler, S., Munk, D., Katzman, M., Zhou, L., Zadok, A., and Schneider, T. (2020). Integrated high-resolution optical spectrum analyzer with broad operational bandwidth. *IEEE Photonics Technology Letters*, 32(17):1061–1064.

[Mokhtari et al., 2013] Mokhtari, A., Jamshidi, K., Preußler, S., Zadok, A., and Schneider, T. (2013). Tunable microwave-photonic filter using frequency-to-time mapping-based delay lines. *Optics Express*, 21(18):21702–21707.

[Mower et al., 2013] Mower, J., Zhang, Z., Desjardins, P., Lee, C., Shapiro, J. H., and Englund, D. (2013). High-dimensional quantum key distribution using dispersive optics. *Physical Review A*, 87(6):062322.

[Mu et al., 2020] Mu, X., Wu, S., Cheng, L., and Fu, H. (2020). Edge couplers in silicon photonic integrated circuits: A review. *Applied Sciences*, 10(4):1538.

[Nagarajan et al., 2010] Nagarajan, R., Kato, M., Pleumeekers, J., Evans, P., Corzine, S., Hurtt, S., Dentai, A., Murthy, S., Missey, M., Muthiah, R., et al. (2010). Inp photonic integrated circuits. *IEEE Journal of Selected Topics in Quantum Electronics*, 16(5):1113–1125.

[Naghdi and Chen, 2016] Naghdi, B. and Chen, L. R. (2016). Silicon photonic contradirectional couplers using subwavelength grating waveguides. *Optics express*, 24(20):23429–23438.

[Neilson, 2004] Neilson, D. T. (2004). Advanced mems devices for channelized dispersion compensation. In *Optical Fiber Communication Conference*, page WK4. Optica Publishing Group.

[Neilson et al., 2004] Neilson, D. T., Ryf, R., Pardo, F., Aksyuk, V. A., Simon, M.-E., Lopez, D. O., Marom, D. M., and Chandrasekhar, S. (2004). Mems-based channelized dispersion compensator with flat passbands. *Journal of lightwave technology*, 22(1):101.

[Newbury et al., 2010] Newbury, N. R., Coddington, I., and Swann, W. (2010). Sensitivity of coherent dual-comb spectroscopy. *Optics express*, 18(8):7929–7945.

[Nitkowski et al., 2008] Nitkowski, A., Chen, L., and Lipson, M. (2008). Cavity-enhanced on-chip absorption spectroscopy using microring resonators. *Optics express*, 16(16):11930–11936.

[Noh et al., 2017] Noh, H., You, T., Mun, J., and Han, B. (2017). Regularizing deep neural networks by noise: Its interpretation and optimization. *Advances in neural information processing systems*, 30.

[Notaros et al., 2017] Notaros, J., Mower, J., Heuck, M., Lupo, C., Harris, N. C., Steinbrecher, G. R., Bunandar, D., Baehr-Jones, T., Hochberg, M., Lloyd, S., et al. (2017). Programmable dispersion on a photonic integrated circuit for classical and quantum applications. *Optics express*, 25(18):21275–21285.

[Okamoto et al., 2019] Okamoto, S., Minoguchi, K., Hamaoka, F., Horikoshi, K., Matsushita, A., Nakamura, M., Yamazaki, E., and Kisaka, Y. (2019). A study on the effect of ultra-wide band wdm on optical transmission systems. *Journal of Lightwave Technology*, 38(5):1061–1070.

[Pasricha and Nikdast, 2020] Pasricha, S. and Nikdast, M. (2020). A survey of silicon photonics for energy-efficient manycore computing. *IEEE Design & Test*, 37(4):60–81.

[Pathak et al., 2014] Pathak, S., Dumon, P., Van Thourhout, D., and Bogaerts, W. (2014). Comparison of awgs and echelle gratings for wavelength division multiplexing on silicon-on-insulator. *IEEE Photonics Journal*, 6(5):1–9.

[Pathak et al., 2013] Pathak, S., Vanslembrouck, M., Dumon, P., Van Thourhout, D., and Bogaerts, W. (2013). Optimized silicon awg with flattened spectral response using an mmi aperture. *Journal of Lightwave Technology*, 31(1):87–93.

[Pérez-López et al., 2020] Pérez-López, D., López, A., DasMahapatra, P., and Capmany, J. (2020). Multipurpose self-configuration of programmable photonic circuits. *Nature communications*, 11(1):6359.

[Piels and Bowers, 2023] Piels, M. and Bowers, J. E. (2023). Photodetectors for silicon photonic integrated circuits. *Photodetectors*, pages 419–436.

[Pinguet et al., 2008] Pinguet, T., Analui, B., Balmater, E., Guckenberger, D., Harrison, M., Koumans, R., Kucharski, D., Liang, Y., Masini, G., Mekis, A., et al. (2008). Monolithically integrated high-speed cmos photonic transceivers. In *2008 5th IEEE international conference on group IV photonics*, pages 362–364. IEEE.

[Reed et al., 2022] Reed, B. D., Meyer, M. J., Abramzon, V., Ad, O., Ad, O., Adcock, P., Ahmad, F. R., Alppay, G., Ball, J. A., Beach, J., et al. (2022). Real-time dynamic single-molecule protein sequencing on an integrated semiconductor device. *Science*, 378(6616):186–192.

[Reed, 2008] Reed, G. T. (2008). Silicon photonics: the state of the art.

[Reed and MarksII, 1999] Reed, R. and MarksII, R. J. (1999). *Neural smithing: supervised learning in feedforward artificial neural networks*. Mit Press.

[Rickman, 2014] Rickman, A. (2014). The commercialization of silicon photonics. *Nature Photonics*, 8(8):579–582.

[Rickman et al., 1994] Rickman, A., Reed, G., and Namavar, F. (1994). Silicon-on-insulator optical rib waveguide loss and mode characteristics. *Journal of Lightwave Technology*, 12(10):1771–1776.

[Rogers et al., 2021] Rogers, C., Piggott, A. Y., Thomson, D. J., Wiser, R. F., Opris, I. E., Fortune, S. A., Compston, A. J., Gondarenko, A., Meng, F., Chen, X., et al. (2021). A universal 3d imaging sensor on a silicon photonics platform. *Nature*, 590(7845):256–261.

[Ruan et al., 2022] Ruan, X., Li, H., and Chu, T. (2022). Inverse-designed ultra-compact polarization splitter–rotator in standard silicon photonic platforms with large fabrication tolerance. *Journal of Lightwave Technology*, 40(21):7142–7149.

[Sahin et al., 2017] Sahin, E., Ooi, K., Png, C., and Tan, D. (2017). Large, scalable dispersion engineering using cladding-modulated bragg gratings on a silicon chip. *Applied Physics Letters*, 110(16).

[Seok et al., 2019] Seok, T. J., Kwon, K., Henriksson, J., Luo, J., and Wu, M. C. (2019). Wafer-scale silicon photonic switches beyond die size limit. *Optica*, 6(4):490–494.

[Shafiee et al., 2022] Shafiee, A., Banerjee, S., Chakrabarty, K., Pasricha, S., and Nikdast, M. (2022). Loci: An analysis of the impact of optical loss and crosstalk noise in integrated silicon-photonic neural networks. In *Proceedings of the Great Lakes Symposium on VLSI 2022*, pages 351–355.

[Shastri et al., 2021] Shastri, B. J., Tait, A. N., Ferreira de Lima, T., Pernice, W. H., Bhaskaran, H., Wright, C. D., and Prucnal, P. R. (2021). Photonics for artificial intelligence and neuromorphic computing. *Nature Photonics*, 15(2):102–114.

[Shekhar et al., 2023] Shekhar, S., Bogaerts, W., Chrostowski, L., Bowers, J. E., Hochberg, M., Soref, R., and Shastri, B. J. (2023). Silicon photonics–roadmapping the next generation. *arXiv preprint arXiv:2305.15820*.

[Shi et al., 2020] Shi, W., Tian, Y., and Gervais, A. (2020). Scaling capacity of fiber-optic transmission systems via silicon photonics. *Nanophotonics*, 9(16):4629–4663.

[Siew et al., 2021] Siew, S. Y., Li, B., Gao, F., Zheng, H. Y., Zhang, W., Guo, P., Xie, S. W., Song, A., Dong, B., Luo, L. W., et al. (2021). Review of silicon photonics technology and platform development. *Journal of Lightwave Technology*, 39(13):4374–4389.

[Siriani and Tambasco, 2021] Siriani, D. F. and Tambasco, J.-L. (2021). Adiabatic guided wave optics–a toolbox of generalized design and optimization methods. *Optics Express*, 29(3):3243–3257.

[Sohler et al., 2008] Sohler, W., Hu, H., Ricken, R., Quiring, V., Vannahme, C., Herrmann, H., Büchter, D., Reza, S., Grundkötter, W., Orlov, S., et al. (2008). Integrated optical devices in lithium niobate. *Optics and Photonics News*, 19(1):24–31.

[Soref, 2006] Soref, R. (2006). The past, present, and future of silicon photonics. *IEEE Journal of selected topics in quantum electronics*, 12(6):1678–1687.

[Soref and Bennett, 1987] Soref, R. and Bennett, B. (1987). Electrooptical effects in silicon. *IEEE journal of quantum electronics*, 23(1):123–129.

[Subramanian et al., 2015] Subramanian, A. Z., Ryckeboer, E., Dhakal, A., Peyskens, F., Malik, A., Kuyken, B., Zhao, H., Pathak, S., Ruocco, A., De Groote, A., et al. (2015). Silicon and silicon nitride photonic circuits for spectroscopic sensing on-a-chip. *Photonics Research*, 3(5):B47–B59.

[Sumi et al., 2018] Sumi, R., Gupta, R. K., DasGupta, N., and Das, B. K. (2018). Ultra-broadband add-drop filter/switch circuit using subwavelength grating waveguides. *IEEE Journal of Selected Topics in Quantum Electronics*, 25(3):1–11.

[Sun et al., 2009] Sun, X., Liu, H.-C., and Yariv, A. (2009). Adiabaticity criterion and the shortest adiabatic mode transformer in a coupled-waveguide system. *Optics letters*, 34(3):280–282.

[Tang and Reed, 1995] Tang, C. and Reed, G. (1995). Highly efficient optical phase modulator in soi waveguides. *Electronics letters*, 31(6):451–452.

[Tao et al., 2008] Tao, S., Fang, Q., Song, J., Yu, M., Lo, G., and Kwong, D. (2008). Cascade wide-angle y-junction 1× 16 optical power splitter based on silicon wire waveguides on silicon-on-insulator. *Optics express*, 16(26):21456–21461.

[Thomson et al., 2016] Thomson, D., Zilkie, A., Bowers, J. E., Komljenovic, T., Reed, G. T., Vivien, L., Marris-Morini, D., Cassan, E., Virot, L., Fédéli, J.-M., et al. (2016). Roadmap on silicon photonics. *Journal of Optics*, 18(7):073003.

[Vermeulen et al., 2010] Vermeulen, D., Selvaraja, S., Verheyen, P., Lepage, G., Bogaerts, W., Absil, P., Van Thourhout, D., and Roelkens, G. (2010). High-efficiency fiber-to-chip grating couplers realized using an advanced cmos-compatible silicon-on-insulator platform. *Optics express*, 18(17):18278–18283.

[Vit et al., 2022] Vit, A. D., Gorgulu, K., Amiri, A. N., and Magden, E. S. (2022). Silicon photonics toolkit.

[Vlasov et al., 2005] Vlasov, Y. A., O'boyle, M., Hamann, H. F., and McNab, S. J. (2005). Active control of slow light on a chip with photonic crystal waveguides. *nature*, 438(7064):65–69.

[Wang et al., 2014] Wang, J., Sheng, Z., Li, L., Pang, A., Wu, A., Li, W., Wang, X., Zou, S., Qi, M., and Gan, F. (2014). Low-loss and low-crosstalk 8× 8 silicon nanowire awg routers fabricated with cmos technology. *Optics express*, 22(8):9395–9403.

[Wang et al., 2018] Wang, X., Zhao, Y., Ding, Y., Xiao, S., and Dong, J. (2018). Tunable optical delay line based on integrated grating-assisted contradirectional couplers. *Photonics Research*, 6(9):880–886.

[Wang et al., 2020] Wang, X., Zhou, L., Lu, L., Wang, X., and Chen, J. (2020). Integrated optical delay line based on a loopback arrayed waveguide grating for radio-frequency filtering. *IEEE Photonics Journal*, 12(3):1–11.

[Wang et al., 2016] Wang, Y., Gao, S., Wang, K., and Skafidas, E. (2016). Ultra-broadband and low-loss 3 db optical power splitter based on adiabatic tapered silicon waveguides. *Optics letters*, 41(9):2053–2056.

[Weiner, 2011] Weiner, A. M. (2011). Ultrafast optical pulse shaping: A tutorial review. *Optics Communications*, 284(15):3669–3692.

[Witzens, 2018] Witzens, J. (2018). High-speed silicon photonics modulators. *Proceedings of the IEEE*, 106(12):2158–2182.

[Wu et al., 2020a] Wu, S., Mu, X., Cheng, L., Mao, S., and Fu, H. (2020a). State-of-the-art and perspectives on silicon waveguide crossings: A review. *Micromachines*, 11(3):326.

[Wu et al., 2020b] Wu, Y.-L., Liang, F.-C., Chung, H.-C., and Tseng, S.-Y. (2020b). Adiabaticity engineering in optical waveguides. *Optics Express*, 28(20):30117–30129.

[Xia et al., 2011] Xia, Z., Eftekhar, A. A., Soltani, M., Momeni, B., Li, Q., Chamanzar, M., Yegnanarayanan, S., and Adibi, A. (2011). High resolution on-chip spectroscopy based on miniaturized microdonut resonators. *Optics express*, 19(13):12356–12364.

[Xing et al., 2022] Xing, Y., Dong, J., Khan, U., and Bogaerts, W. (2022). Capturing the effects of spatial process variations in silicon photonic circuits. *ACS Photonics*, 10(4):928–944.

[Xu and Shi, 2017] Xu, H. and Shi, Y. (2017). Flat-top cwdm (de) multiplexer based on mzi with bent directional couplers. *IEEE Photonics Technology Letters*, 30(2):169–172.

[Yaacobi et al., 2014] Yaacobi, A., Sun, J., Moresco, M., Leake, G., Coolbaugh, D., and Watts, M. R. (2014). Integrated phased array for wide-angle beam steering. *Optics letters*, 39(15):4575–4578.

[Yang et al., 2021] Yang, Z., Albrow-Owen, T., Cai, W., and Hasan, T. (2021). Miniaturization of optical spectrometers. *Science*, 371(6528):eabe0722.

[Ye et al., 2021] Ye, M., Sun, C., Yu, Y., Ding, Y., and Zhang, X. (2021). Silicon integrated multi-mode ring resonator. *Nanophotonics*, 10(4):1265–1272.

[Yu et al., 2018] Yu, M., Okawachi, Y., Griffith, A. G., Picqué, N., Lipson, M., and Gaeta, A. L. (2018). Silicon-chip-based mid-infrared dual-comb spectroscopy. *Nature communications*, 9(1):1869.

[Yun et al., 2019] Yun, H., Hammood, M., Lin, S., Chrostowski, L., and Jaeger, N. A. (2019). Broadband flat-top soi add–drop filters using apodized subwavelength grating contradirectional couplers. *Optics Letters*, 44(20):4929–4932.

[Zhang et al., 2020] Zhang, Z., El-Henawy, S. I., Miller, R., and Boning, D. S. (2020). Decomposed representation of s-parameters for silicon photonic variation analysis. In *Optical Modeling and Performance Predictions XI*, volume 11484, pages 29–41. SPIE.

[Zhang et al., 2023] Zhang, Z., El-Henawy, S. I., Ocampo, C. A. R., and Boning, D. S. (2023). Inference of process variations in silicon photonics from characterization measurements. *Optics Express*, 31(14):23651–23661.

[Zhang et al., 2019] Zhang, Z., El-Henawy, S. I., Sadun, A., Miller, R., Daniel, L., White, J. K., and Boning, D. S. (2019). Adjoint-based sensitivity analysis for silicon photonic variations. In *2019 IEEE MTT-S International Conference on Numerical Electromagnetic and Multiphysics Modeling and Optimization (NEMO)*, pages 1–4. IEEE.

[Zhao et al., 1995] Zhao, C., Li, G., Liu, E., Gao, Y., and Liu, X. (1995). Silicon on insulator mach–zehnder waveguide interferometers operating at 1.3 μm. *Applied physics letters*, 67(17):2448–2449.

[Zheng et al., 2019] Zheng, S., Cai, H., Song, J., Zou, J., Liu, P. Y., Lin, Z., Kwong, D.-L., and Liu, A.-Q. (2019). A single-chip integrated spectrometer via tunable microring resonator array. *IEEE Photonics Journal*, 11(5):1–9.

[Zhu et al., 2021] Zhu, D., Shao, L., Yu, M., Cheng, R., Desiatov, B., Xin, C., Hu, Y., Holzgrafe, J., Ghosh, S., Shams-Ansari, A., et al. (2021). Integrated photonics on thin-film lithium niobate. *Advances in Optics and Photonics*, 13(2):242–352.

[Zhuang et al., 2015] Zhuang, L., Roeloffzen, C. G., Hoekman, M., Boller, K.-J., and Lowery, A. J. (2015). Programmable photonic signal processor chip for radiofrequency applications. *Optica*, 2(10):854–859.